Carbon nanotube field-effect sensors for single-molecule detection

Sebastian Sorgenfrei

Submitted in partial fulfillment of the

requirements for the degree

of Doctor of Philosophy

in the Graduate School of Arts and Sciences

COLUMBIA UNIVERSITY

2011

Abstract

Carbon nanotube field-effect sensors for single-molecule detection

Sebastian Sorgenfrei

This thesis describes a detection system for single molecules based on individual single-walled carbon nanotube field-effect sensors. The sensitivity, spatial confinement and transducer gain of the sensor is derived from a conductance controlled electrochemically created defect, which is also chemically reactive. An automated microfluidic system is designed to enable long and stable measurements of the carbon nanotube device in aqueous environment with temperature control of $\pm 0.1°C$. A probe DNA can be covalently attached to the defect through an amide bond and the conductance is modulated when a target DNA binds to the probe. As a result, the conductance shows a traditional random telegraph signal and fluctuates between a hybridized and melted state. By monitoring the conductance as a function of temperature, the kinetics and thermodynamics can be extracted, which are comparable to previous fluorescent correlation spectroscopy studies using optical fluorescent resonant energy transfer. By studying the fluctuation amplitude as a function of charge proximity, buffer concentration and solution potential, it is shown that the sensor is based on a field-effect. The sensor has a temporal resolution of 200 μs and a signal to noise ratio of 3-8 when continuously measuring for 30 seconds. By further reducing the parasitics, the sensor has the capabilities to detect biomolecule kinetics down to microsecond resolution, which could make it an attractive tool for single-molecule experiments with fast kinetics.

Contents

List of Figures

List of Tables

Acknowledgments

This dissertation would not have been possible without the help and support of many people. First of all, I would like to thank my supervisor, Professor Kenneth Shepard, for his support and encouragement over the six years that I have worked in his group. With his keen perception, Ken immediately understands complex problems and tries to find solutions to them. I have learnt a lot about device physics, digital circuits and systematic technical writing from him. In particular, I am grateful for his positive attitude and optimism towards research, which is very important when things are not working out. It was both challenging and rewarding to work in a group with very interdisciplinary research and I am grateful that Ken is actively exploring projects in many unusual fields for an electrical engineer such as single-molecule biophysics.

I really want to thank Chien-yang Chiu (Frank) for an amazing collaboration. Frank is a great chemist and one of the most diligent and thoughtful people that I know and it was a pleasure to be able to work with him for many long days in the lab. I will never forget when our first device started to work at around 3 am on October 9th, 2009. Besides his tremendous help on the technological side, we had many lunches and dinners together during which I could take my mind off of work.

I would like to thank Professor Ruben Gonzalez for several short but very intense conversations in his office. In particular the 12 minute conversation that we had when I was showing a prospective student around. Instead of discussing the program, we started to talk about this project and the possible future experiments. I am thankful to Ruben for giving me biological insights and directing me to relevant literature and also discussing the

data. I think in my next life, I will try to become a biophysicist. Besides Ruben and Ken, I would also like to thank my other thesis committee members, which are Professor John Kymissis, Professor Colin Nuckolls and Professor Wen Wang for their attention and time reading the thesis.

Throught the years, the members of the Shepard group have had a large impact on my work and I have become friends with many of them. First and foremost, I want to thank Inanc Meric for working together on many projects and developing a lot of the infrastructure and protocols for making devices. I am very grateful to have him as a friend and coworker, lunch and coffee buddy and fellow German speaker. I would also like to thank my fellow classmates Matthew Johnston and Omar Ahmad. I learned a lot about microfluidics from Matt and both of you were very fun to be around. I would like to thank the group members that finished before me especially George Patounakis who was my first contact with the Shepard group, Peter Levine, David Huang, David Schwartz, Na Lei and Vicky Wang with whom I had many good conversations on both a technical and personal level. Steven Warren was very nice to proofread the thesis and Ryan Field took care of my computer issues and provided voluntary tech support. I also wanted to thank members of the Shepard group who came after me including Simeon Realov, Jared Roseman, Jacob Rosenstein, Siddharth Ramakrishnan, Brian Tull, Eyal Aklimi, Daniel Bellin, Haig Norian, Noah Sturcken, Kevin Li, Michael Lekas and Anthony Erlinger for providing a good working atmosphere. Ken is very fortunate to have so many bright and hard-working students.

Many lunch breaks were spend with the faculty house crew, Sami Rosenblatt, Robert Caldwell, Inanc and Caroline Lee. At times, it seemed that all the experimentalists in physical science at Columbia University were working on graphene so it was easy to colaborate and start on several projects based on graphene, particular with Professor Philip Kim's group from physics. I really appreciated working with Andrea Young, Cory Dean, Vikram Desphande, Kirill Bolotin and Young-Jun Yu. After work, the epic squash battles with Andrea and Cory provided a good way to relax. I also enjoyed interacting with the analog circuits lab people including Ajay Balankutty, Frank Zhang, Mariya Kurchuk and Colin

Weltin-Wu. I want to thank Professor Peter Kinget for giving me the chance to work as an undergraduate and for introducing me to research.

I also want to thank my industry supervisors during my time at Columbia for giving me the opportunity to see beyond the Ivory Tower and work on several intersting projects. These includes Marc Schneider from Dr. Ing. h.c. F. Porsche AG, Dr. Christian Pacha and Dr. Jörg Berthold from Infineon Technologies AG and Dr. Sam Kavusi, Dr. Clementz Portmann and Dr. Christoph Lang from Robert Bosch LLC.

New York is an amazing place to pursue a PhD and I want to thank some friends over the years, Sonja Bebber, Franziska Kluge, Daniel Douglas, Clifford Huang, Steven Tam, Meghan FitzPatrick, Taylor Sullivan and Ryan Lynn for reminding me that there are other things out there. I wanted to thank the "turkish mafia", Inanc, Tufan Eratici, Deniz Tunaoglu, Ipek Attik and Sera Beoglu for the good times and "wednesday night frenzies". I especially wanted to thank Deniz for her kindness and support and for always being there for me.

Ganz besonders möchte ich mich bei meinen Eltern für Ihre grenzenlose Unterstützung bedanken. Mit meiner Entscheidung in die USA zu kommen habe ich es Ihnen über die Jahre nicht leicht gemacht und sie haben mich jederzeit unterstützt und waren immer für mich da.

Für meine Eltern.

So eine Arbeit wird eigentlich nie fertig,

man muss sie für fertig erklären,

wenn man nach Zeit und Umständen

das Mögliche getan hat.

-Johann Wolfgang von Goethe

Chapter 1

Introduction

When Richard Feynman gave his famous talk "There is plenty of room at the bottom" at the annual meeting of the American Physical Society on December 29th 1959, he was envisioning a world where things could be manipulated and controlled on an atomic scale. His idea of a physicist arranging individual atoms to synthesize any chemical compound certainly sounded like science fiction at the time, when computers were still the size of a room. The tools and methods to manipulate and image individual atoms and molecules did not exist. Around the same time, on September 12th 1958, Jack Kilby demonstrated the first monolithic integrated circuits with a single transistor and a few other components on a single piece of germanium [1].

More than half a century later, generations of scientists and engineers have greatly improved existing techniques and made groundbreaking new discoveries. A single integrated circuit chip can now have billions of transistors and other components and the channel length of commercial state of the art transistors is only 22 nm (announced by Intel Corporation on May 4^{th}, 2011), which approaches the atomic scale that Feynman was dreaming about. Many biophysical methods for the study of single molecules have been developed and are still being developed that provide a toolbox for novel fundamental experiments in biology, chemistry and physics and also allow a significant cost reduction in DNA sequencing. In particular, inventions such as the scanning tunneling microscope and the atomic force mi-

croscope have enabled researchers to probe and manipulate single atoms and molecules. Using advanced optical and spectroscopy techniques such as single molecule fluorescent resonance energy transfer and optical tweezers, researchers are able to study the dynamics and fluctuations of single molecules such as DNA and proteins.

When probing biomolecules at the single molecule level, dynamics can be observed that are usually hidden in ensemble measurements where dynamics of many molecules are averaged. Because these methods require sensitivities at the single molecule level, which is the fundamental limit, there is a complex tradeoff between sensitivity, signal-to-noise ratio and bandwidth. The motivation for this thesis is to develop a single molecule biosensor based on a nanoscale field-effect transistor with potential for very high bandwidth applications.

The biosensor is made from a single walled carbon nanotube field effect transistor, which is around 1.5 nm in diameter and designed to operate in a liquid environment. A point defect is introduced in the pristine nanotube by a conductance controlled electrochemical oxidation step. The point defect localizes the sensitivity of the conductance and also provides a chemical reactive site to which a biomolecule can be covalently attached. DNA has been used as a proof of principle of the sensor and probe DNA is covalently attached to the defect. The conductance shows a two level fluctuation when the channel is exposed to complementary target DNA. Experiments at different temperatures, buffer concentrations and DNA proximities to the defect demonstrate a field effect based sensing mechanism. The biosensor is label free and has the potential for very high bandwidth applications because of the underlying flicker noise limitation.

1.1 Thesis outline

Chapter 2 provides a brief overview of existing single molecule techniques and compares them in terms of sensitivity, spatial resolution and bandwidth. Since the main experiments involve the detection of DNA, the focus will be on techniques that are able to image and probe single DNA molecules. Chapter 3 introduces carbon nanotubes and shows their applications as field effect transistors with focus on one dimensional transport and defects.

In order to further multiplex the nanotube sensors and reduce parasitics, the long term goal is to integrate the devices on an active complementary metal oxide semiconductor (CMOS) substrate. Chapter 4 describes some promising integration techniques such as mechanical transfer, spin-on nanotubes and dielectrophoresis using an electronic detection system.

Chapter 5 discusses how carbon nanotube field effect transistors can operate in liquid environment, discusses noise and demonstrates that pristine nanotubes can be used as biosensors. However, the sensitivity is not sufficient for single molecule detection. Chapter 6 discusses how the sensitivity can be improved by point defects. This is done through an electrochemical method while monitoring the device conductance. Both scanning gate microscopy and low temperature measurements show that the sensitivity is localized and the defect acts as a barrier for electron transport. This chapter also describes the design of using a carbon nanotube field effect transistor for single molecule DNA hybridization, shows the experimental results and goes over the analysis of the thermodynamics and kinetics data. Chapter 7 discusses an improved design and shows how the amplitude is affected by charge proximity and buffer concentration. Chapter 8 concludes the thesis.

Chapter 2

Measuring single molecules

Fundamental biological and biophysical research has created a variety of different tools and techniques for single-molecule studies. This chapter provides a brief overview of several of the most common techniques for probing single molecules and compares them from the perspective of a sensor system. Since the main part of the thesis studies DNA hybridization dynamics, the chapter will very briefly discuss DNA and its thermodynamic properties. Important performance metrics for single molecule sensors will be discussed such as noise, signal-to-noise ratio, spatial resolution and bandwidth.

2.1 DNA overview

2.1.1 DNA structure

All living organisms on earth store their hereditary information in double stranded molecules of deoxyribonucleic acid (DNA). This genetic blueprint is essential to life because it serves as the long-term storage for the instructions for all cellular functions. DNA can be copied in a process called DNA replication in which the original double stranded DNA is separated and then used as a template to make identical strands. The information to make single proteins and ribonucleic acid molecules (RNA) are stored in genes, which are small segments of DNA. These genes are first transcribed into RNA and then translated into amino acids, which are the building blocks of proteins.

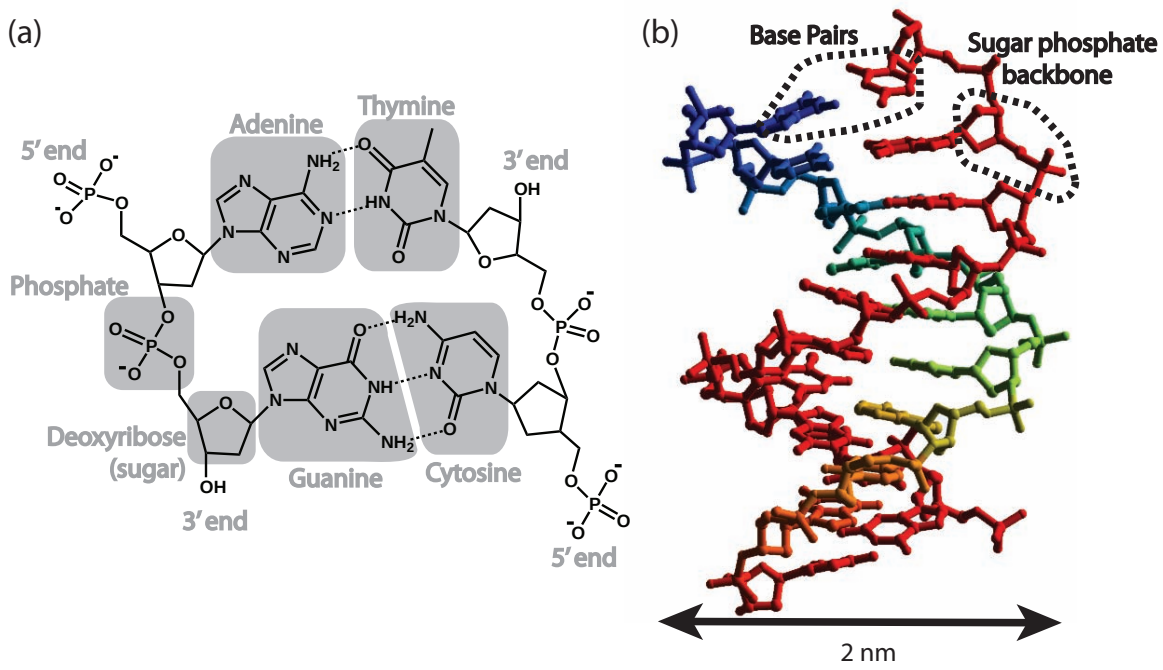

Figure 2.1: The structure of DNA. (a) Chemical Structure of DNA showing all four nucleotides. (b) The 3D structure of the DNA double helix.

The basic structure of DNA is shown in Fig. 2.1 and was first suggested by Watson and Crick [2]. The DNA molecule consists of two polynucleotide chains with four types of nucleotide subunits. The nucleotides consist of three parts, the phosphate group, the deoxyribose sugar and the nitrogenous bases shown in Fig. 2.1a. There are four types of bases, adenine (A), cytosine (C), guanine (G) and thymine (T). The sequence of these bases contains all the organisms hereditary information. At neutral buffer concentration, the phosphate group is negatively charged, which is responsible for the acidic nature of the molecule.

The nucleotides are covalently linked to each other through the sugars and phosphates, which forms the backbone of the DNA strand. Two polynucleotide chains are held together by hydrogen bonds between the bases: an A base can only pair with a T base and a G base can only pair with a C base. The resulting structure is displayed as a double helix in Fig. 2.1b. The double helix structure is an energetically favorable configuration and leads to a very tightly packed and rigid structure with a base-to-base separation of 0.33 nm and with a width of 2 nm [3]. This is also the reason for the long persistence length in

double stranded DNA of 50 nm, whereas single stranded DNA (only one polypeptide chain) has a persistence length of only 2 nm [4].

2.1.2 DNA Thermodynamics

A lot of cellular functions such as DNA replication and translation require the ordered double helix DNA structure to transition into an unpaired single strand in which the bases are not stacked. At low temperatures, the double helix structure has a lower energy than two single strands of DNA in the random coil state. Because the double stranded state is stable and there is a large energy barrier to go from the double stranded state back into the single stranded state, single stranded DNA hybridizes and then stays in the double helix state. As the temperature is increased, the energy barrier decreases and the double stranded DNA will eventually melt into two single strands of DNA.

In order to better understand the formation of duplex DNA, it is essential to consider chemical kinetics and thermodynamics [5]. The hybridization between probe A and target B to result in a DNA duplex AB can be expressed as the reversible reaction

$$A + B \leftrightarrow AB. \tag{2.1}$$

The equilibrium constant K is given by the concentration of the product divided by the concentrations of the reactants,

$$K = \frac{[AB]}{[A][B]}. \tag{2.2}$$

Assuming an equal probe and target DNA concentrations that are free to react in solution, the above concentrations can be rewritten in terms of the fraction of total strands in duplex form α. For initial DNA concentrations $[A]_0 = [B]_0 = C$, the equilibrium concentrations will be $[A] = C - \alpha C$, $[B] = C - \alpha C$ and $[AB] = 2\alpha C$. K can be rewritten as

$$K = \frac{2\alpha C}{(C - \alpha C)^2} \approx \frac{2\alpha}{(1 - \alpha)^2 C} \tag{2.3}$$

The equilibrium constant K is given by the change in Gibbs free energy, ΔG as

$$K = e^{-\frac{\Delta G}{kT}} \tag{2.4}$$

where the Gibbs free energy is the work that needs to be done to create the duplex DNA or the work that is recovered when going back to the single strands at a constant pressure and temperature. The change in Gibbs free energy can be expressed in terms of the change in enthalpy, ΔH and change in entropy, ΔS, as

$$\Delta G = \Delta H - T\Delta S. \tag{2.5}$$

Combining equations 2.3-2.5, the change in enthalpy and entropy can be related to the fraction of strands in duplex form at a given temperature so that

$$kT \ln\left(\frac{2\alpha}{(1-\alpha)^2 C}\right) = \Delta S - T\Delta H. \tag{2.6}$$

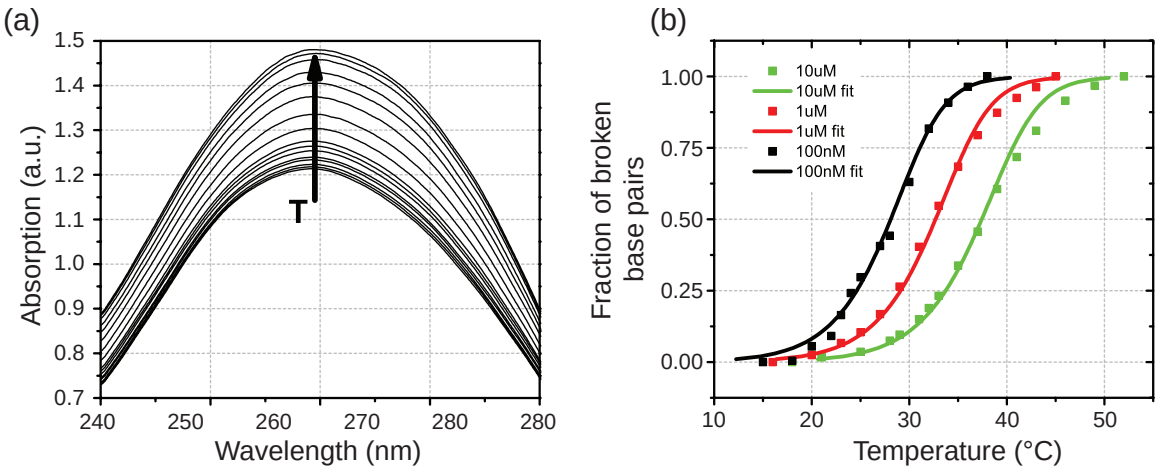

Figure 2.2: DNA Thermodynamics. (a) DNA absorption spectrum taken with UV-Vis (b) Extracted melting curve for different concentrations.

There are two main methods for monitoring the thermodynamic properties of DNA. The first one is using scanning differential calorimetry, which monitors the change in heat capacity. If some of the heat is used for the chemical reaction, a change in heat capacity will be detected. This analysis can be done for several temperatures to develop a melting

curve and extract enthalpy and entropy values. Another method is to use the temperature dependence of the spectroscopy properties as shown in Fig. 2.2a. The absorption of the solution with the majority of the DNA in single stranded form is higher at 260 nm than the adsorption with the majority of the DNA in the duplex form, resulting in an increase of the 260 nm peak at higher temperatures. By plotting the normalized change in the 260 nm peak, it is possible to extract the melting curve as shown in Fig. 2.2b. This melting curve is extracted from equal concentrations of probe DNA with sequence 5'-GGAAAAAAGG-3' and complementary target DNA using ultraviolet-visible absorption spectroscopy (UV-Vis). As shown in Eqn. 2.6, the melting curve is dependent on the concentration. The melting temperature shifts to lower temperatures at lower concentrations.

2.2 DNA sequencing

2.2.1 Ensemble Sequencing

Since the start of the Human Genome Project [6] in 1990, tremendous work has been made both in DNA sequencing and improving sequencing technologies. Even though the sequence of the human genome was already completed in 2003, sequencing continues to be a growing market with applications in comparative genomics [7], genomic studies especially targeted towards the role of single nucleotide polymorphisms (SNPs) in both common and rare human diseases [8], cancer research [9], gene regulation [10], personal medicine [11] and drug discovery [12].

The total cost for the bulk sequencing of the human genome was approximately US $300 million. In order to make the above applications commercially viable, the cost of sequencing the genome has to be significantly decreased. In fact, the ambitious goal after the completion of the human genome was to reduce the cost for an entire human genome to US $1000. This can only be achieved if significant technological improvements in sequencing technologies are made by increasing the throughput and reducing the costs per base. In fact, the sequencing method used to complete most of the human genome has not changed

significantly since its invention in 1977 though it was made more efficient. It is based on the Sanger Sequencing method [13,14], which uses electrophoresis to separation DNA fragments with single base pair resolution.

Emerging ensemble technologies for sequencing are based on hybridization sequencing [6,15] in which single stranded DNA probes are immobilized on a surface, usually glass, and then analyte with single stranded DNA target is introduced. If the probe and target sequences are complementary, hybridization will occur and trigger a signal from a label. Sequence-by-synthesis [16, 17] and pyrosequencing [18] has also been used for sequencing (these are also refered to as cyclic-array sequencing). These methods use the enzyme DNA polymerase to incorporate a single nucleotide to an unknown single DNA stand by cycling through the four bases. If a new base is complementary to the next unknown base, it will get incorporated and triggers a signal by either chemiluminescence or fluorescence.

The ensemble techniques described above have been demonstrated for genomic sequencing with high yield and accuracy. However, the initial concentration of DNA when extracted is below the detection limit of most sensors and needs to be amplified and purified. When extracting DNA from the white blood cells in human blood, the concentration is usually in the 10s of attomoles, which is too low for accurate detection [19]. Amplification is usually done by a method called polymerase chain reaction (PCR) [20] which cycles through a three step process until the desired concentration is reached. The solution used in PCR consists of the double stranded DNA to be amplified, DNA polymerase, the four nucleotide triphosphates, magnesium ion and two synthetic oligonucleotide primers. In the first step, the solution is heated to 95 C to anneal the target DNA. In the second step, the solution is cooled to 37-55 °C so that the primers anneal to their target sequence. Then in the last step, the solution is heated to 75 °C so that the polymerase can extend the primers. These steps are repeated and after each cycle, the amount of DNA strands is approximately doubled. The final products after PCR can be separated by agarose gel electrophoresis.

2.2.2 Single-Molecule Sequencing

The drawback of the ensemble based techniques is that they require DNA cloning and PCR amplification which limits the reduction in costs that can be achieved. As an alternative, methods to directly sequence single DNA molecules have been suggested [6, 21]. Besides avoiding amplification, single molecule based sequencing also requires less starting material and has the potential for a very multiplexed detection. The basic technique is also based on a cyclic-array method in which a polymerase incorporates a fluorescent-labeled single nucleotide to a primed DNA template. A review of these advanced sequencing technologies can be found in [21]. Compared to the automated Sanger sequencing method previously used, these single molecule techniques can reduce the cost by 3-4 orders of magnitude and provide a viable platform for sequencing.

2.3 Single-Molecule Techniques for Fundamental Research

In the last two decades, the field of single molecule biophysics has continuously grown and due to tremendous technological advancements, groundbreaking experimental studies on single molecules have been accomplished [22–24]. These studies have focused on studying and understanding biological systems by visualization and manipulation of biomolecules. The following sections serve as an overview of the most popular and successful techniques in single molecule studies. Because single molecules are the ultimate detection limit of biosensors, performance metrics such as limit of detection, sensitivity and bandwidth are important system considerations. A discussion on the sensor fundamentals has been adopted in Section 2.3.1, signal-to-noise ratio is discussed in Section 2.3.2 and general attributes of good single-molecule sensors in Section 2.4. Then in Section 2.4, representative single molecule techniques based on optical, force, tunneling, nanopore and field effect are discussed.

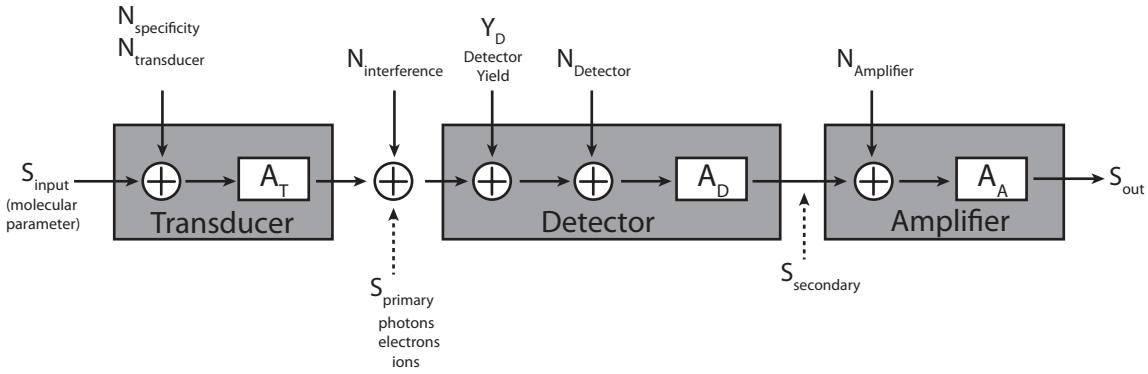

Figure 2.3: System block diagram.

2.3.1 Sensor Fundamentals

At its most fundamental level, the task of any sensor is to infer the internal state of a system through a set of external observables. Due to the limited signal levels available from single molecule sensors, a compromise is often made to observe only discrete states such as the presence or absence of a molecule or discrete conformational changes in a single molecule. Any real sensor will have some degree of variability in its output, leading to uncertainty in estimates of the systems state. The uncertainty can be expressed as measurement noise, but it is instructive to categorize the paths through which noise can appear in a measurement.

A conceptual schematic of a biosensor signal path is shown in Fig. 2.3. The system is separated into three parts, a transducer, detector and amplifier. The transducer is directly in contact with the biological system and produces a set of signals, which corresponds the presence or state of the biomolecule. Depending on the transducer, the output may take the form of photons, ions or electrons. The role of the detector is to convert the transducer output into an electrical signal (either current or voltage). An amplifier adjusts the signal level such that it is appropriate to interface with other electronic circuits and data converters. Ideally, the state of the biomolecule has been converted to a digital signal that can either be further processed or stored in memory.

Due to limitations in specificity, noise can appear at the transducer. Specificity refers to the ability of the transducer to only show a response to the biomolecule to be studied and not to other extraneous signals. This category of noise can include effects such

as nonspecific adsorption to the transducer or the degree to which the transducer produces a similar signal from other biomolecules in the solution. Noise (or unwanted signals) can also arrive later in the signal chain. In contrast to signals that originate at the sensor input, this noise is uncorrelated to the transducer output and can be categorized as part of the background detection limit. These effects include dark current of a photodetector or noise added from an amplification stage.

In order to quantify the noise better, it is useful to refer the noise contribution of the system back to the input. This can be achieved by dividing the noise by the total gain to that point in the signal chain. In this way, a high-gain transducer can reduce the contributions of noise which appears later in the signal chain. The input-refered noise power (N_{input}) of the system in Fig. 2.3 is given by:

$$N_{input} = N_{specificity} + \frac{N_{interferenc}}{A_T^2} + \frac{N_{Detector}}{(Y_D A_T)^2} + \frac{N_{amplifier}}{(A_D Y_D A_T)^2} \tag{2.7}$$

The noise formulation in Eqn. 2.7 includes all noise and interference sources which exist in the signal path. So far the assumption was made that the signals are continuous quantities. Often however, the weak signals produced by the single-molecule biosensors consist of a countable number of particles, which can make the intermediary signal $S_{primary}$ discrete. As a consequence, when interrogating biomolecular processes at short time scales (millisecond or microsecond timescales), the signal presented to the detector can be extremely quantized both in time and amplitude.

In traditional systems, the gain is defined as the ratio of the continuous amplitudes along a signal chain. However, this definition cannot be used in the case of weak discrete signals. Instead of using the amplitude, it is possible to specify the rate of a signal since the signal is made of discrete particles. For modeling purposes, the transducer output can be expressed by a homogeneous Poisson process. The probability of having k events in time τ is given by

$$P(\text{k events in time } \tau) = \frac{e^{-\lambda\tau}(\lambda\tau)^k}{k!} \tag{2.8}$$

The rate parameter λ is the expected number of events in unit time. If the gain of the transducer is low, then the rate parameter λ is also small and there is a high variance in the measurements, which can be described as either thermal or shot noise, depending on the context [25]. This noise is intrinsic to working with weak quantized signals and can only be reduced by increasing the gain of the transducer, thereby increasing the rate λ or by increasing the measurement time τ. In the limit of either infinite gain or infinite measurement intervals, the system approaches a continuous output.

2.3.2 Signal-to-Noise Ratio and Bandwidth

When comparing different biosensor platforms, a good performance metric is the signal-to-noise ratio (SNR), which is simply the signal at the input divided by the noise at the input, given by Eqn. 2.7. However, both the signal and the noise of a sensor are functions of frequency and a careful study of the biosensor system is necessary to optimize the SNR. First, it is crucial to understand the bandwidth of the biological system as well as the bandwidth of the transducer and noise. For example, if the noise spectrum is flat but the signal fluctuations are band-limited, then increasing the bandwidth will improve the SNR until the bandwidth exceeds the frequency content of the signal. Second, the optimum SNR depends on what information the sensor system is trying to extract from the biological system. A measurement of the average state of a single fluctuating molecule would be optimized with a lower bandwidth than a measurement of the molecules kinetic parameters.

2.4 Representative Single Molecule Systems

Given the above discussion on the system level description of single molecule biosensor systems, it is possible to look at general features that can optimize these sensors. In order to make single-molecule measurements at all, the system has to constrain the sensitivity to a very small physical volume because otherwise, the background noise can overwhelm the single-molecule measurement. In optical sensors, this localization is usually achieved with lenses and strategic illumination patterns. In electrochemical sensors such as nanopores and

field-effect based sensors, the small dimension of the sensor itself provides the sensitivity localization. However, just having a sensor with a very localized sensitivity is not enough since the sensor could also respond to other biomolecules in the sample. To get around this problem, specificity is introduced by making the transducer biological interface chemical selective. This is done through the use of proteins or functional group, which specifically bind to the target molecule.

Lastly, the ideal single-molecule sensor will also have high gain in the transducer. This will produce a high rate of observations, thereby increasing the SNR. A high gain transducer can ease the impact of noise later in the signal chain and can be leveraged either to increase the bandwidth of the system or lower the minimum detectable signal.

2.4.1 Fluorescent techniques

Over the last two decades, fluorescent techniques have arguably become the standard method for probing molecules at the single-molecule level both *in vivo* and *in vitro*. From a sensor perspective, a fluorescent molecule is used to label the biological system or biomolecule and it serves as the transducer. The energy from absorbed photons is used to excite electrons, which again emit photons when relaxing from excited states back down to bound states [26]. The emitted photon is slightly lower in energy due to energy given off to lattice vibration and heat and the shift in wavelength is called the Stokes shift. By using optical filtering, the background noise from the laser can be reduced and only the emitted photons from the fluorophore are imaged.

The spatial resolution of fluorescence has long been limited by the diffraction limit of light to around 200-300 nm and only very recent techniques have successfully overcome this limit through statistical reconstruction algorithms [27, 28]. Single molecule fluorescence has been used to study Brownian diffusion of single DNA molecules [29], one dimensional diffusion of proteins along DNA [30], the motion of the molecular motor myosin on actin [31] and molecular rotation [32]. However, spatial separation of two fluorescent particles in close proximity is very difficult to do especially at molecular dimension.

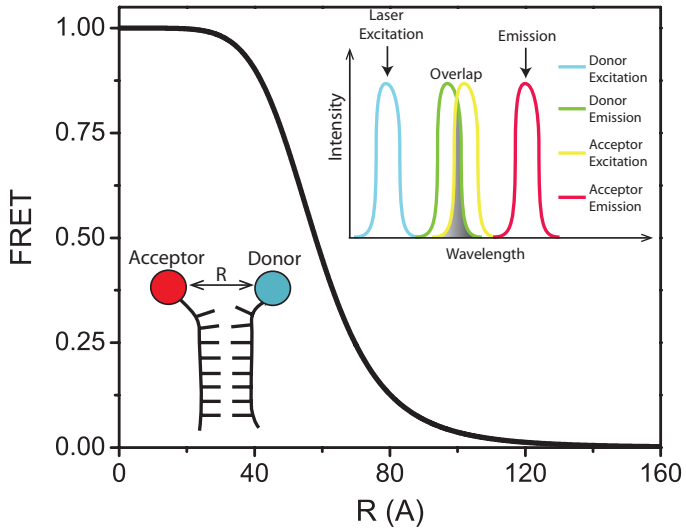

Figure 2.4: FRET ratio as a function of donor and acceptor fluorophore sepraation. Inset shows excitation and emission spectrum of the FRET pair.

Using Fluorescence Resonance Energy Transfer (FRET) [33, 34], events at much smaller length scales in the 1-10 nm range can be probed. In this technique, the dipole-dipole interaction of a donor and acceptor fluorophore is used to obtain information about their spatial separation. The donor fluorophores emission spectrum overlaps with the acceptor fluorophores excitation spectrum as depicted in Fig. 2.4. The donor fluorophore can transfer energy to the acceptor fluorophore according to the following relationship for the fraction of energy transfered,

$$E = \frac{1}{1 + (R/R_0)^6} \tag{2.9}$$

Where R is the distance separating the molecules and R_0 is the characteristic distance of the FRET pair (Fig. 2.4). Therefore by looking at the donor and acceptor intensities simultaneously, the distance between the two molecules can be accurately extracted. Since most biomolecules such as DNA, RNA and proteins are a few nanometers in size, the length scale of FRET is ideal to explore inter- and intramolecular dynamics. FRET at the single molecule level has been used to study surface tethered molecules down to millisecond time scales. It has been frequently used to study and probe proteins such as DNA helicases during unwinding [35] and translocation [36] of double stranded DNA, the transcription

mechanism of RNA polymerase [37] and the coupling of the ribosome to RNA [38]. FRET has also been used to look at protein folding in order to determine the folding landscape [39] and also DNA interactions in the form of the four-way Holliday junction [40].

Most of the biological systems or biomolecules in the above experiments have dynamics above 10 milliseconds. For temporal resolutions below 10 milliseconds to microseconds, FRET does not have sufficient SNR and fluorescent correlation spectroscopy (FCS) is used instead. This method focuses a laser on a very small detection volume and extracts the fluctuation rates by taking the autocorrelation of the intensity fluctuation. The advantage is that the signal originates from a very small ensemble of molecules thereby increasing the signal strength. FCS has been used to study molecular diffusion by recording the rates at which molecules enter and leave the detection volume [41] and molecular rearrangements inside of living cells [42].

FCS has also been used to study the loop kinetics of DNA hairpins. In a molecular beacon configuration, the single stranded DNA consists of a stem part at the two ends, which are complementary to each other and a loop part in the middle, which is not complementary. In order to study the kinetics, a donor and acceptor fluorophore is linked to the 5' and 3' end of the DNA. By recording both the donor and acceptor intensities and taking the autocorrelation of the normalized ratio, the hairpin opening and closing rates can be measured. Bonnet *et al.* [43] first recorded the hairpin kinetics and a similar measurement was later repeated by Wallace *et al.* [44] and Li *et al.* [45] By studying the kinetics as a function of temperature, the activation energies can be extracted from the Arrhenius plot. The advantage of the FCS in solution approach is that the results are independent of the diffusion rate and that the molecular interactions can be studied in equilibrium. In Chapter 6, these results will be compared to the data from the single-molecule carbon nanotube sensor, which results in a very similar Arrhenius plot.

For single molecule techniques based on fluorescence, the sensitivity and spatial resolution often results from the advanced microscopy techniques and optics and also low readout noise from the avalanche photodiodes (APD) or charged coupled devices (CCD).

This section describes the different microscopes that are used for single molecule fluorescent detection. One of the most common microscopy setups is the wide-field or epifluorescence microscope. A laser or uniform white lightsource with an excitation filter illuminates the sample and the fluorescent light is detected by a CMOS camera or a CCD sensor. While the epifluorescence microscope is able to uniformly illuminate a relatively large area of about 100 μm, the drawbacks are large background from the out-of-focus light and Raman scattering from the large volume [22]. To reduce the background, a confocal microscope can be used in which a pinhole is introduced in front of the detector. The pinhole can provide three-dimensional resolution by raster scanning in all directions.

While a confocal microscope uses a point detection method, further background reduction can also be achieved by a point illumination. In two-photon microscopy, a laser with energy at about half that necessary for excitation of the fluorophore is focused on a small volume. Excitation is only possible if two photons arrive at approximately the same time to excite the flurophore. Total internal reflection fluorescence microscopy (TIRF) uses an evanescent wave from a total reflection cavity to create a very thin illumination thickness at a liquid/glas interface. This dramatically reduces background so that a wide field microscope can be used to detect multiple molecules at the surface.

2.4.2 Force based techniques

Single-molecule force spectroscopy techniques include optical tweezers, magnetic tweezers and atomic force microscopy (AFM), which will be discussed in this section. A review of these can be found in [24, 46]. These techniques in general involve the application of force to a single molecule and the measurement of displacement. The transducer is the spring element such as the AFM tip or the bead that serves as a force transducer.

The atomic force microscope probes surface properties with a proximal probe at sub-nanometer resolution. A piezoelectric actuator manipulates a cantilever with a nanometer size tip in all three dimensions and the interacting force between the sample and the tip is measured by monitoring the deflection of a laser from the beam of the cantilever. AFM

has mostly been used as an imaging tool to capture topography images of surfaces both in ambient conditions and *in vivo* such as protein assembly [47], protein diffusion [48] and DNA origami [49].

AFM has also been used for one-dimensional force measurements. In this method, the cantilever is not scanned over the surface in the horizontal plane, but rather in the vertical direction at a single point. In this way, the force can be monitored as a function of tip extension and inter and intramolecular interaction forces and extensions can be studied. This method has been used to study the strength of covalent bonds [50], unfolding of proteins [51] and pulling apart of complementary DNA [52]. While the sample preparation for AFM based techniques is relatively straightforward, the disadvantage is the large tip of the cantilever, relative to the molecules, which makes it difficult to distinguish between interactions due to the molecule of interest and nonspecific adsorption to the tip [46]. Also, the relatively large and stiff cantilever results in a lower bound of the pulling force range.

Optical tweezers, also called optical traps, have become a standard method to probe single molecules. By focusing a laser to a diffraction-limited spot, a dielectric particle can be trapped. The laser light creates an optical dipole in the particle, which is attracted by the electric field gradient and therefore exerts a restoring force on the particle. For small particles and steep field gradients, this force dominates and is approximately linear with distance [46]. At the same time, the position of the bead can be monitored down to sub-nanometer resolution by detecting changes in the interference pattern resulting from light that is scattered by the particle with light that has not been scattered. When the particle is at the center of the trap, the interference pattern will be symmetric. Otherwise there are asymmetries in the pattern which can be detected.

Optical tweezers therefore provide a way to both manipulate particles and also record their position and forces. These particles can be polystyrene beads or silica microspheres but also single cells [53] and lipid vesicles [54]. There are two common setups for probing biomolecules with optical tweezers. In the first setup, one end of the molecule is attached to the surface while the other end is attached to the dielectric particle and pulled by the

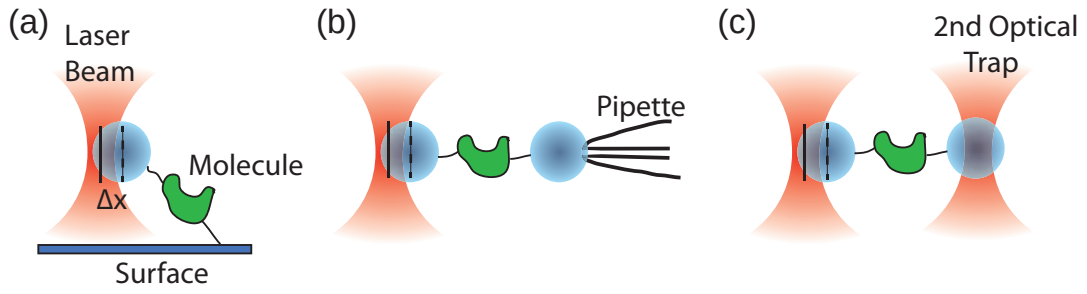

Figure 2.5: Optical tweezers with different configurations (a) Surface tethered (b) held by pipette and (c) held by another optical trap

field gradient, shown in Fig. 2.5a. The second setup sandwiches the molecule between two dielectric particles. One of them is held in place by a pipette (Fig. 2.5b) or another optical trap (Fig. 2.5c) while the other is pulled. Similar to the AFM experiments, it is possible to record force curves as a function of pulled distance but with much better timing resolution due to a much faster reaction time of the particles (millisecond). Optical tweezers have been used to probe the elastic properties of DNA [55,56], the transcription of DNA in RNA polymerase [57], folding of biomolecules such as the riboswitch [58] and the opening of an RNA hairpin [59].

Magnetic tweezers are based on a similar concept as optical tweezers. Instead of an electric field, the force on a magnetic particle is generated by the gradient of the square of the magnetic field. The magnetic field is generated by a permanent magnet based on rare earth magnets [60] or electromagnets [61]. Magnetic tweezers have been used in such experiments as supercoiling DNA by rotating an attached magnetic bead [60] and non-invasive measurements inside of cells [62]. However, the bandwidth and sensitivity of magnetic tweezers are limited by video detection, which does not enable the measurement of fast dynamics or small displacements [46].

2.4.3 Tunneling and molecular transport

The first tool to image individual atoms, molecules and atoms in a crystal lattice was the scanning tunneling microscope (STM). Similar to the AFM, a tip is controlled very precisely by a piezoelectric stage to about 0.1 nm lateral resolution and a bias is applied between the

conductive sample and the tip. A tunnel current results when the tip is brought in very close proximity to the surface. Because this tunneling current depends exponentially on the distance, atomic resolution can be achieved. The tunnel current also depends on the local density of states of both the tip and the sample, which makes the STM the ideal tool to probe molecular orbits.

The STM has been used to image the atoms on a silicon surface [63], atomic structure and density of states of different chiral carbon nanotubes [64, 65] and electronic structure of DNA molecules [66]. The STM has also been used to manipulate individual atoms such as Xeon atoms on a copper substrate [67] and create devices built up from single atoms such as the quantum corral [68]. Due to noise constraints and bandwidth limitations in the piezoelectric actuators and feedback control systems, STM has been primarily used to capture still images at frame rates of around 0.1 Hz or lower.

The concept of probing electronic structure by measuring tunneling currents into and out of molecules can also be achieved by creating nanometer sized gaps in electrodes, which are then bridged by the molecule of interest. These gaps have been made by mechanical [69] or electromigrated break junctions [70], high-resolution lithography [71] and by breaking a metal point contact made by an AFM tip on a conducting surface [72]. Many of these molecular electronics experiments have focused on measuring the electronic transport through individual molecules in solutions at room temperature or in high vacuum at cryogenic temperatures. Break junctions based on both a conducting AFM tip and surface provide a reliable and reproducible platform to measure average conductance values for different molecules.

Tunneling currents through single nucleotides and oligonucleotides have recently been measured by two different groups. Tsutsui *et al.* [73] used a mechanical break junction to create a controlled gap between gold electrodes in order to investigate the capture and release dynamics of single nucleotides between the gap. By measuring the tunneling current to millisecond temporal resolution, the experiments show that the amplitude of the current peaks can be used to identify different nucleotides. Huang *et al.* [74] and Chang *et al.* [75]

used a functionalized STM tip to study tunneling into nucleotides and short oligonucleotides. They obtained similar results and were able to distinguish all four DNA nucleosides by their respective amplitude changes of the tunneling current. In order to use tunneling spectroscopy for DNA sequencing, more development has to be done in order to control the speed at which the DNA passes through the tunnel junction and also separate the current amplitude further between the difference base pairs.

2.4.4 Nanopore

A nanopore sensor is made by connecting two fluid reservoirs with a small aperture in a thin membrane [24, 76]. This aperture is usually only a few nanometers in diameter, comparable in size with the molecules to be studied. When applying a small voltage bias between the reservoir electrodes, a baseline bias current can be measured which corresponds to the flux of dissolved ions moving from one reservoir to the other. When a charged molecule such as DNA is introduced in the electrolyte, the electric field inside the nanopore will translocate these molecules through the nanopore. Because the mobility of the molecules will be lower with respect to the ions, the presence of a molecule in the pore will result in a change in conductivity.

Since nanopores are very common in biology, the first demonstration of a nanopore and many subsequent experiments used biological nanopores from proteins in transmembranes such as the α-Hemolysin [77] (about 1.4 nm in diameter) and the Bacillus subtilis ion channels [78] (about 2 nm in diameter). Synthetic nanopores have also been fabricated from a silicon nitride [79] and silicon dioxide [80] membranes. The nanopore is created and then imaged by using an ion beam or transmission electron microscope (TEM). With this method, pores from 2-100 nm [24] can be reliably drilled in a thin membrane.

In order to optimize the nanopore biosensor, the pore diameter should be of the same size as the biomolecule because the pore size does not affect the signal strength. However, a larger pore increases the background current and the associated noise so that the signal can quickly be obscured. The membrane should also be as thin as possible in order to

maximize gain and bandwidth of the nanopore. Nanopores have been used to detect single and double stranded DNA and RNA molecules [81,82], differentiate between different DNA molecules [83], detect DNA hybridization [84] and filter out single stranded DNA molecules from a solution containing both single and double stranded DNA [85]. Nanopores have been proposed for DNA sequencing but this remains challenging because of the high speed of DNA molecules inside of the pores (1 bp/μs). For this purpose, nanopores with specificity to slow down translation and also nanoelectrodes for measuring tunneling currents are being explored [76].

2.4.5 Field effect techniques

Field effect based biosensors traditionally use a complementary metal-oxide-semiconductor (CMOS) topology as the sensing transducer as shown in Fig. 2.6. The exposed channel is sensitive to surface charges, which can be measured through changes in the capacitance or conductance of the sensor. Initially, ion sensitive field effect transistors (ISFETs) were developed to measure pH and ion concentrations [86]. Since the surface of these transistors is silicon dioxide, standard coupling reactions can be used to covalently attach biomolecules very close to the channel in order to increase specificity and render the ISFET sensitive to specific biomolecules.

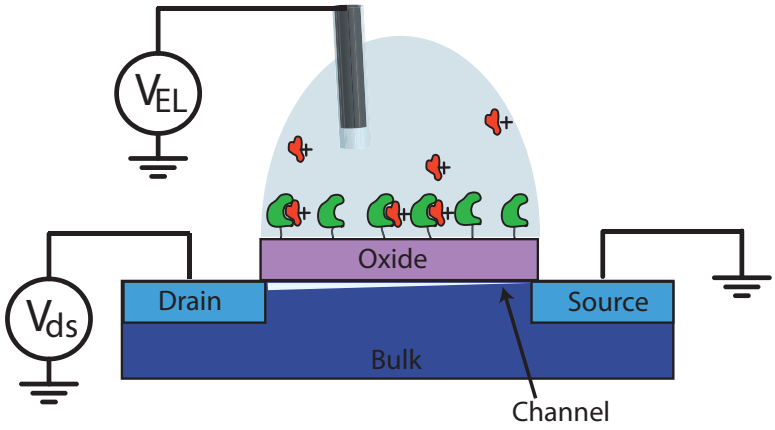

Figure 2.6: Schematic of ISFET.

Technological breakthroughs in lithography and chemical synthesis have lead to

the development of field effect biosensors made of one-dimensional nanostructures such as nanowires and nanotubes. The advantage of these nanostructures is that their diameter is comparable to the biomolecules of interest and that their surface to volume ratio is very large so that most atoms are close to the surface. The combination of these characteristics results in a higher sensitivity, higher signal-to-noise ratio and higher bandwidths.

A top down fabrication scheme has been implemented by Stern *et al.* [87] to lithographically define silicon nanowire transistors on a silicon-on-insulator substrate. These field effect biosensors were used for label-free immunodetection of proteins down to 10 fM concentrations. A bottom up synthesis of silicon nanowires using chemical vapor deposition was used to fabricate nanowire devices with a diameter below 10 nm [88]. These were used to detect cancer markers such as prostate specific antigen in solution with a detection limit of 0.9 pg/ml. The same group also used these nanowires to detect DNA molecules with peptide nucleic acid receptors (PNA) attached to the nanowire oxide [89]. Sensitivities down to the single molecule were demonstrated with nanowires when a single influenza A virus molecule first binds to the channel and then unbinds from it, resulting in a conductance step [90]. One recent commercial success of CMOS-based biochemical analysis is the Ion Torrent sequencing platform (recently aquired by Life Technologies), which uses CMOS-integrated pH sensors for ensemble sequencing-by-synthesis [91].

Carbon nanotubes have also been used as field-effect transistors for biosensing applications. Initially, biological experiments on carbon nanotubes were done by nonspecific binding of biomolecules [92,93]. Hydrophobic interactions between the nanotube surface and the biomolecules such as proteins cause them to adsorb strongly without preferences [94]. Star *et al.* [95] demonstrated that probe DNA molecules can be adsorbed to the nanotube sidewall in a nanotube network. When the devices are exposed to complementary DNA, hybridization will occur and a change in conductance can be measured. This label free approach was capable of detection target DNA with a detection limit of 12 pM.

In order to improve specificity, noncovalent and covalent attachments have been pursued. For the noncovalent attachements, 1-pyrenebutanoic acid [96] and surfactant

molecules [97] have been successfully used as anchors for protein immobilization. The advantage of the noncovalent attachement procedure is that the electronic properties of the nanotube remain relatively unperturbed by the chemical functionalization. A covalent approach is much more invasive and can render the nanotube insulating [98].

The carbon nanotube field effect biosensors described above have demonstrated the possibility of detecting molecules down to picomolar concentrations. However, they are not able to detect single molecule events because they have insufficient sensitivity localization since many biomolecules can adsorb along the nanotube sidewall and each will contribute to the change in conductance. They also have insufficient gain for detecting individual molecules. These issues can be overcome by two different approches. In the first approach, a small nanogap is etched into the nanotube channel by ultrafine lithography [71]. The carboxylic acid groups at each side on the nanotube gap can be used to covalently attach a biomolecule with the same dimensions inside the gap. The carbon nanotube acts as very small electrodes for a tunneling probe of the biomolecule, similar to an STM. In this way, conductance of small molecules and DNA molecules has been measured [71, 99].

Another approach is to create a defect in the nanotube channel in a controlled way. This has been achieved by using conductance controlled electrochemical oxidation [100], which will be further explained in Chapter 6. The advantage of this approach is that the resulting defect is both chemically reactive and electrically sensitive. Goldsmith *et al.* [101] used this method to study the binding of a small linker molecule (a reactive carbodiimide) to the carboxylic acid defect. Coulomb interactions between the molecule and the defect result in modulation of the scattering in the one-dimensional channel. A two level fluctuation in the device conductance with a change of more than 100 nS is observed.

2.4.6 Comparison

Despite their significant differences, it is worthwhile to find general metrics by which to compare these different single molecule techniques. A few important parameters are summarized in Table 2.1. The exact value of these parameters will depend strongly on the specifications

	Fluorescence	Force	Tunneling	Nanopore	CNT
Spatial Resolution	Rayleigh limit (∼200 nm); FRET ∼1 nm	Interferometry ≤1 nm	Tunnel gap ∼nms	Pore diameter ∼nms	Defect size ∼nms
Transducer Gain	Low	Moderate	High	Moderate	High
Specificity	High	Moderate	Low	Low	Moderate
Transducer Output	Photons	Mechanical Deflection	Electrons	Electrons	Electrons
Detector	Photodiode CCD PMT SPAD	Photodiode CCD	None	Ag/AgCl	None
Dominant noise	Shot noise	Thermal noise	Shot noise Thermal noise	Flicker noise Thermal noise	Flicker noise
Temporal Resolution	FRET∼ms FCS∼ns	$\sim 100\mu$s	$\sim 100\mu$s	$\sim 100\mu$s	$\sim 200\mu$s (parasitics)

Table 2.1: Single-molecule sensor comparison

of each sensor. The first comparison will regard spatial resolution. Whereas fluorescence can distinguish multiple fluorescent probes on the order of the diffraction limit [102] (∼200 nm), the localized resonance energy transfer in FRET can distinguish donor and acceptor fluorophore separations down to nanometer scales. Even higher spatial resolutions can be obtained by force-based methods down to sub-nanometer resolution using back focal plane interferometry for optical tweezers or very precise piezoelectric actuators in AFM. Tunneling and nanopore sensors have a spatial resolution dependent on their geometries such as gap size and pore diameter, usually around a few nanometers. The spatial resolution of carbon nanotubes with a defect is dependent on the localized defect state, but is also affected by the Debye screening in solution. This will be demonstrated in Chapter 7 of the thesis.

The gain in the transducers of the methods outlined above differs by several orders of magnitude. Fluorophore emission rates depend on the laser excitation power and is usually around 2500 photons per second for organic dyes and can be up to 50000 photons per second for quantum dots [102]. However, organic dyes are much more common in FRET applications because they are much smaller and minimize the perturbation of the biomolecule of interest and because their orientation with respect to the biomoelcule is much easier to control [103]. A higher gain can be achieved by increasing the laser power

but this leads to faster photobleaching. Force-based methods have higher gain because the laser intensity can be higher and a small deflection or change in position by the particle leads to a large change in the output. Nanopore, tunneling devices and field effect carbon nanotube transistors have a relatively high gain in the transducer because several billion electrons are transduced in the channel for a single molecule.

Another important criterion to describe biomolecular sensors is specificity. The specificity of proteins and functional groups used in fluorescent imaging techniques can be extremely high. Force based techniques have lower specificity because the probe or the AFM tip is usually larger and much more difficult to eliminate non-specific adsorption. In Tunneling experiments, specificity can be high because single molecules can be easily imaged and the small dimensions of the nanogap usually only allow for a single molecule to be trapped. Nanopores usually have relatively little chemical selectivity and instead distinguish molecules by their size and charge. Carbon nanotubes can achieve higher specificity by using probe molecules but still have non-specific adsorption to the nanotube sidewall away from the defect.

2.5 Model systems for SNR calculations

2.5.1 Autocorrelation and Spectrum

Suppose that in a chemical reaction, a reactant A can react to form a product B.

$$A \underset{k_r}{\overset{k_f}{\rightleftharpoons}} B \tag{2.10}$$

This is a unimolecular reaction since there is only one reactant A. According to law of mass action, the differential rate equation can be written as

$$-\frac{dc_A}{dt} = k_f c_A - k_r c_B \tag{2.11}$$

$$-\frac{dc_B}{dt} = k_r c_B - k_f c_A \tag{2.12}$$

with initial conditions $c_A = c_{A_0}$ and $c_{B_0} = 0$ [104]. The solution is given by

$$\frac{c_A - c_{A_e}}{c_{A_0} - c_{A_e}} = e^{-(k_f + k_r)t} \tag{2.13}$$

$$1 - \frac{c_B}{c_{B_e}} = e^{-(k_f + k_r)t} \tag{2.14}$$

where c_{A_e} and c_{B_e} are the equilibrium concentrations. Over time, the concentration of product B will increase and the concentration of reactant A will decrease as plotted in Fig. 2.7a until the equilibrium is reached. At equilibrium, the concentrations of reactant A and product B are constant over time and the equilibrium constant for the reaction is given by $K = \frac{k_f}{k_r} = \frac{c_{B_e}}{c_{A_e}}$. In the single molecule case, the chemical reaction will turn a single reactant molecule into a single product molecule and then back to a reactant molecule. To a first approximation, the traditional phenomenology based on the simple rate law for the large population should also be valid so that the single molecule kinetics should follow Poisson statistics [105, 106] described by Eq. 2.8. After equilibrium is reached, Fig. 2.7b shows the ideal trajectory of a molecule that fluctuates between two states. This is very different compared to the ensemble case because after equilibrium is reached, the ensemble concentrations are constant and information about the reaction rates cannot be extracted because the signal from many molecules is averaged. For the single molecule case, the dwell times follow an exponential distribution, given by the probability density function

$$f(t, \tau) = \frac{1}{\tau} e^{-\frac{t}{\tau}}, \tag{2.15}$$

for which the expected dwell time is τ. τ could be the same for the high and low states but for generality, the dwell time in the high state is expressed as τ_1 and in the low state as τ_0. If there existed an ideal detector without any variability in measuring the single molecule trajectories, it would give an output that would be identical to the fluctuations in Fig 2.7b with an amplitude variation between 0 and ΔI for the two states. This trajectory is called random telegraph noise because it is continuous in time and discrete in amplitude.

For this stochastic process X(t), the autocorrelation can be computed [107, 108]:

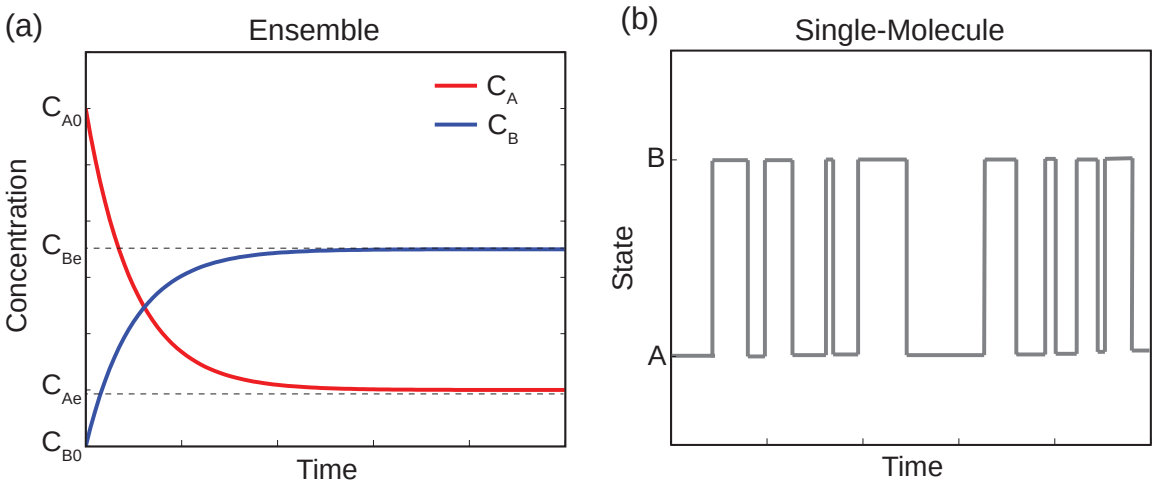

Figure 2.7: Kinetics of a chemical reaction. (a) Ensemble experiments and (b) Single Molecule Experiment (after equilibrium is reached).

$$R_{xx}(t,t+\tau) =< X(t)X(t+\tau) >$$
$$= \sum_{i,j} X_i X_j * \Pr(x(t)=x_i) * \Pr(x(t+\tau)=x_j \text{ given that } x(t)=x_i). \quad (2.16)$$

Since the amplitude of the low state is 0, all terms vanish except one [108],

$$R_{xx}(t,t+\tau) = R_{xx}(\tau) = \frac{\Delta I^2}{(\tau_0+\tau_1)^2}(\tau_1^2 + \tau_0\tau_1 e^{-\tau(\frac{1}{\tau_0}+\frac{1}{\tau_1})}). \quad (2.17)$$

The random telegraph noise is wide sense stationary (since the mean and autocorrelation functions are invariant to time shifts) and ergodic (the ensemble average can be calculated using time averages). Therefore using the Wiener-Khintchine-Einstein Theorem, the power spectral density for the random telegraph noise can be computed by taking the fourier transform of the autocorrelction function above.

$$\begin{aligned} S_{xx}(f) &= \int_{-\infty}^{+\infty} R_{xx}(\tau) e^{-j2\pi f\tau} d\tau \\ &= \frac{4\Delta I^2}{(\tau_0+\tau_1)} \frac{1}{[(\frac{1}{\tau_0}+\frac{1}{\tau_1})^2 + (2\pi f)^2]} \end{aligned} \quad (2.18)$$

2.5.2 Noise in single molecule systems

The different transducer output signals and system gains result in very different input referred noise characteristics. Optical systems are often limited at low frequencies by the detector dark current (or dark rate) and by shot noise at high frequencies due to the relatively low photon rates. Force based methods are limited by thermal drift and mechanical vibrations at low frequencies and thermal noise of the probe at high frequencies. Noise in scanning tunneling microscope and tunnel gap devices contains both 1/f noise at low frequencies and thermal noise at higher frequencies [109]. The exact noise shape depends on the setup such as servo feedback and position control which can further shape the noise [75]. Both nanopore and carbon nanotube have large flicker noise at low frequencies and thermal noise at high frequencies. In order to further study the trends in the signal-to-noise ratio, signal-to-noise ratios as a function of the two level fluctuation rate has been calculated for systems limited by shot noise (fluorescence), thermal noise (optical tweezer) and flicker noise (carbon nanotube). In all three cases, the signal spectrum was calculated using the spectrum in Eqn. 2.18 by varying Poisson rate parameter ($1/\tau$=$1/\tau_0$+$1/\tau_1$) from 1 Hz to 1 MHz. In general, the SNR can be written as

$$\frac{S}{N} = \frac{\int_{1/T_{meas}}^{+\infty} S_{xx}\ S_{MF}\ S_{BW}}{\int_{1/T_{meas}}^{+\infty} Noise\ S_{MF}} \tag{2.19}$$

where S_{MF} is the response of the matched filter and S_{BW} is the lowpass filter due to the detector, given by

$$\begin{aligned} S_{MF} &= \frac{S_{xx}}{S_{xx}(1/T_{meas})} = \frac{1}{1+(2\pi f\tau)^2} \\ S_{BW} &= \frac{1}{1+(\frac{f}{BW})^2} \end{aligned} \tag{2.20}$$

For fluorescence, the dominant noise is shot noise and the dark current of the detector. Assuming a photon emission rate of 5000 photons/s and a dark rate of equivalent to 50 photons/s, the noise can be represented by

$$N_{fluorescence} = N_{shot} + N_{dark} = 2q(50q + 5000q) \tag{2.21}$$

where q is the charge of the electron and the quantum efficiency was assumed to be 1. The signal is

$$S_{xx} = \frac{2\tau(5000q)^2}{4 + (2\pi f\tau)^2}, \tag{2.22}$$

with a detector bandwidth of BW=10 kHz.

Optical tweezers are dominated by thermal fluctuations of the probe so that the noise can be expressed as [46]

$$N_{tweezers} = \frac{k_B T}{\pi^2 \beta (f^2 + f_0^2)} \tag{2.23}$$

Where β is the hydrodynamic drag ($\beta = 6\pi\eta a$), which is a function of the viscosity of the medium (η) and the radius of the probe tip (a). f_0 is related to the stiffness of the optically trapped bead (α) and inversely proportional to the hydrodynamic drag ($f_0 = \frac{\alpha}{2\pi\beta}$. The signal is assumed to be a 5 nm displacement and there are no other bandwidth limitations. The SNR was calculated for a 2 μm probe, stiffness of 0.1pN/nm and and viscosity of water.

In chapter 5, it will be shown that flicker noise is due to random fluctuations of charge in the environment of the channel. The noise model can be expressed as

$$N_{CNT} = \frac{A}{f} \tag{2.24}$$

where $A = 1$ nA^2. The signal is 20 nA and a signal roll-off beginning at 5 kHz due to electronic parasitics. For each system, a matched filter corresponding to the Lorentzian spectral content of the fluctuations follows the sensor for optimal signal-to-noise ratio. The results for these models are shown in Fig. 2.8. The plot shows the SNR as a function of average rate of molecular fluctuations. The SNR is defined as the ratio of the root mean square power after the matched filter. Clearly, there are different trends in the three systems. The fluorescent and optical tweezer system have a flat noise spectrum and as a result, the SNR decreases steadily with bandwidth. The carbon nanotube has a flicker noise

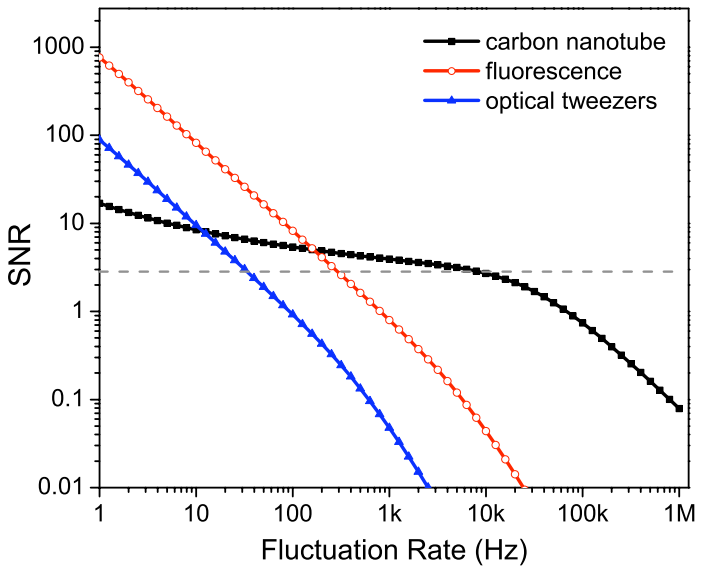

Figure 2.8: Simulated SNR of two-level fluctuating systems for carbon nantoube, FRET pair and optical tweezers.

spectrum yielding an SNR, which is relatively insensitive to bandwidth. In all models, the SNR begins to decrease more rapidly after the transducer bandwidth is exceeded.

Even though Fig. 2.8 is simulated for a very specific case, this simple model can be used to improve the SNR performance for each sensor. The FRET based SNR can be improved by increasing the laser intensity, thereby decreasing the flicker noise and shifting up the SNR curve. The carbon nanotube can be built on a better dielectric with lower traps and dangling bonds, thereby reducing the flicker noise and also shifting up the SNR curve. At the same time, the parasitics can be significantly improved so that the bandwidth based rolloff can be pushed out. Finally for the optical tweezers, the viscosity of the medium and the size of the particle can be increased thereby shifting up the SNR curve but reducing the bandwidth at the same time.

Chapter 3

Electronic properties of carbon nanotubes

3.1 History of carbon materials

With its ability to form several distinct types of valence bonds, carbon based materials can come in very different structural forms [110]. In its natural form, configurations of pure carbon exist in both the three-dimensional diamond structure with diamond cubic crystal structure and graphite made from stacked sheets of honeycomb crystals. Even though Thomas Edison was able to engineer light bulb filaments from carbon fibers in the 19th century, it took until the end of the 20th century for carbon materials to show their real potentials. In 1985, the zero dimensional carbon fullerenes were discovered by Kroto *et al.* [111], consisting of a truncated isohedral structure similar to a football. In 1991 Sumio Iijima synthesized carbon nanotubes ranging from 2 to 50 shells [112]. Transmission electron microscope confirmed the one-dimensional structure with diameter of a few nanometers and length up to 1 μm. Finally in 2005, the two dimensional form of carbon, graphene made from a single sheet of carbon atoms in a honeycomb crystal lattice was created [113, 114].

3.2 Energy dispersion in graphene

Carbon nanotubes are an especially interesting material since they are truly a one-dimensional (1D) structure, which results in many unique properties, including quantization of conductance, strong electron-electron interactions which deviates from the usual Fermi liquid behavior and gives rise to Luttinger liquid behavior and finally strong singularities in the density of states. In order to understand electronic properties of carbon nanotubes, it is essential to first examine the electron transport in graphene. In fact, carbon nanotubes can be seen as small cut out strips of graphene that are rolled up into cylindrical shape. Carbon atoms consist of 6 electrons which occupy the $1s^2$, $2s^2$ and $2p^2$ orbitals. However, since the energy levels for the $2s^2$ and $2p^2$ orbitals are very close, they start to mix and can form different hybridization configurations such as sp, sp^2 and sp^3. Graphene and carbon nantoubes are formed by sp^2 hybridization by creating one 2s and 3p atomic orbitals in the following manner [110]:

$$\begin{aligned} sp^2_{a\pm} &= \frac{1}{\sqrt{3}}(|2s\rangle \pm \sqrt{2}|2p_x\rangle) \\ sp^2_{b\mp} &= \frac{1}{\sqrt{3}}(|2s\rangle + \sqrt{2}(\mp\frac{1}{2}|2p_x\rangle + \frac{\sqrt{3}}{2}|2p_y\rangle)) \\ sp^2_{c\mp} &= \frac{1}{\sqrt{3}}(|2s\rangle + \sqrt{2}(\mp\frac{1}{2}|2p_x\rangle - \frac{\sqrt{3}}{2}|2p_y\rangle)) \\ 2p_z &= 2p_z \end{aligned} \tag{3.1}$$

In the above equations, the sp orbitals are newly formed σ orbitals made from the mixed 2p orbitals. The remaining $2p_z$ orbital is called the π orbital. It is the π orbital that forms the covalent bond between neighboring atoms and also conducts electrons. In Fig. 3.1, the σ orbitals are in the plane of the graphene sheet and the π orbital is in the out of plane direction. As carbon atoms bond with each other, a graphene sheet is formed that consists of a honeycomb lattice where each atom has three closest neighbors shown in Fig. 3.2. As a direct consequence of the covalent bond, neighboring atoms share electron pairs, which leads to a delocalization of electrons in the 2pz orbital. These delocalized electrons

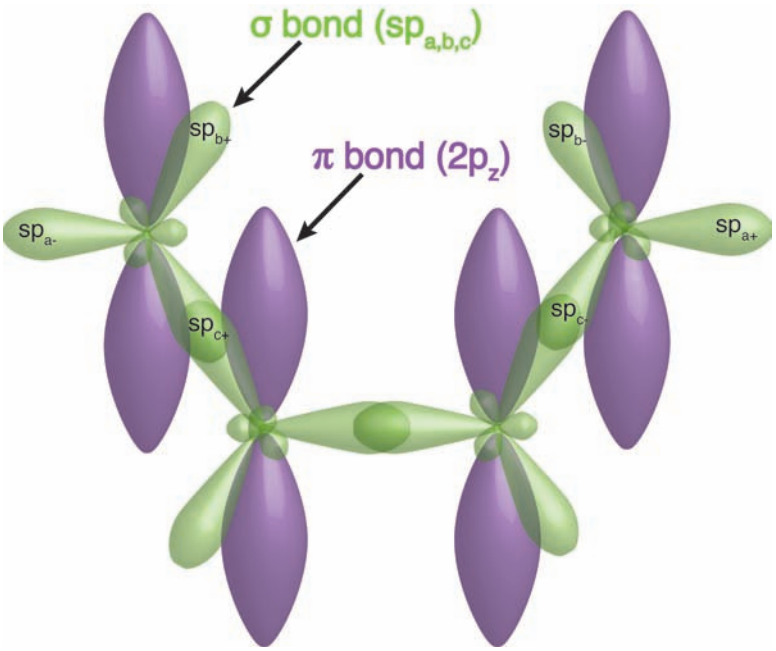

Figure 3.1: Sp^2 hybridization in graphene.

are free to move around in the crystal, but still feel the effect of the underlying period potentials from the carbon ions, which leads to energy bands.

The band structure of graphene can be calculated by considering the tight binding approximation, in which the electrons wavefunction is approximated by the original atomic orbitals. In a periodic lattice, electrons wavefunction has to satisfy Bloch theorem [115]

$$\phi_{nk} = \sum_R e^{ikR}\phi_n, \tag{3.2}$$

where k is the wavevector of the plane wave and R is the position of all ions in the crystal. If the localized atomic wavefunction solves the Schroedinger equation, given by

$$H_{at}\phi_n = [\frac{\hbar^2}{2m}\nabla^2 + U_{at}(r)]\phi_n = E_n\psi_n \text{ where } U_{at}(r) = -\frac{ze^2}{r}, \tag{3.3}$$

the delocalized states can be built up from the local atomic wavefunctions. If the primitive basis (or unit cell) of graphene contains two atoms, given by atoms A and B in Fig. 3.2 and only the pz atomic orbital is taken into account, the Bloch function for an electron in the crystal can be written as a superposition of the atomic orbitals at position

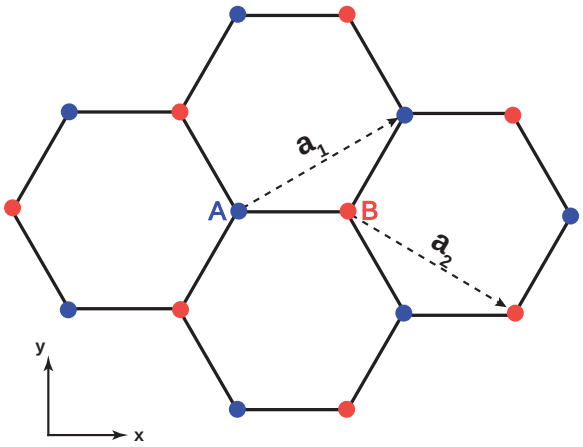

Figure 3.2: Graphene lattice.

A and B,

$$\psi = c_A\phi_A(r) + c_B\phi_B(r), \tag{3.4}$$

which can solve the modified Schrdinger equation and satisfy Bloch theorem at the same time.

$$\widetilde{H}\psi_k = [\frac{\hbar^2}{2m}\nabla^2 + U_{at}(r) + \sum_{R\neq 0} U_{at}(r-R)]\psi_{nk} = (E_{at} + \Delta U)\psi_{nk} \tag{3.5}$$

The energies of the Schrdinger equation above are given by

$$\langle\phi_n|\widetilde{H}|\psi_{nk}\rangle = E_{nk}\langle\phi_n|\psi_{nk}\rangle. \tag{3.6}$$

In order to solve for the energies E_{nk}, the tight binding assumption is made. This means that only the closest atomic orbitals (one A atom with the three surrounding B atoms and one B atom with the three surrounding A atoms) are overlapping. The overlapping integral from two neighboring atoms and the transfer integral are defined as

$$\begin{aligned} \alpha &= \langle\phi_A|phi_B\rangle \text{ (overlap integral) and} \\ \gamma &= \langle\phi_A|\Delta U|\phi_B\rangle \text{ (transfer integral)} \end{aligned} \tag{3.7}$$

The two equations at the A and B atoms are

$$\begin{aligned} \langle\phi_A|\widetilde{H}|\psi_{nk}\rangle &= E_k\langle\phi_A|\psi_{nk}\rangle \text{ and} \\ \langle\phi_B|\widetilde{H}|\psi_{nk}\rangle &= E_k\langle\phi_B|\psi_{nk}\rangle \end{aligned} \tag{3.8}$$

Which can be simplified to

$$\begin{aligned} E_{at}c_A + \xi\gamma c_B &= E_k(c_A + \xi\alpha c_B) \\ E_{at}c_B + \xi^*\gamma^* c_A &= E_k(c_A + \xi^*\alpha^* c_B). \end{aligned} \tag{3.9}$$

The function ξ above can be calculated by considering the position of the three closest atom and summing up the equivalent phase contributions, so that

$$\xi = \frac{e^{ikxa}}{\sqrt{(3)}} + 2e^{-\frac{ikxa}{2\sqrt{3}}}cos(\frac{k_y a}{2}). \tag{3.10}$$

$$\begin{pmatrix} (E_{at} - E_k) & (\xi\gamma - E_k\xi\alpha) \\ (\xi^*\gamma^* - E_k\xi^*\alpha^*) & (E_{at} - E_k) \end{pmatrix} \begin{pmatrix} c_A \\ c_B \end{pmatrix} = \begin{pmatrix} 0 \\ 0 \end{pmatrix} \tag{3.11}$$

which results in the energy dispersion relationship for graphene:

$$E_k = E_{at} \pm \frac{\gamma|\xi|}{1 \pm \alpha|\xi|} \approx E_{at} \pm \gamma\sqrt{(1 + 4cos(\frac{\sqrt{(}3)k_x a}{2})cos(\frac{k_y a}{2}) + 4(cos(\frac{k_y a}{2}))^2)} \tag{3.12}$$

The energy dispersion of graphene is symmetric around the origin and the conduction and valence band are touching at 6 points, which is why graphene is refered to as a semimetal. The energy dispersion of graphene is ploted in Fig. 3.3. Around these points, the dispersion relationship is roughly linear given and often written in terms of the Fermi velocity ν_F so that $E_k \approx \hbar\nu_F\sqrt{k_x^2 + k_y^2}$.

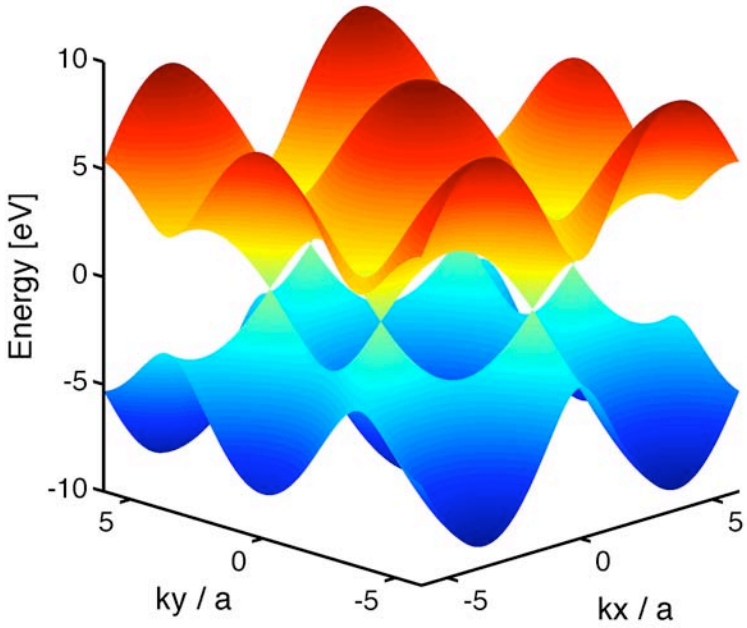

Figure 3.3: Energy dispersion in Graphene.

3.3 Energy dispersion and density of states in carbon nanotubes

Having derived the band structure of graphene, the band structure of carbon nanotubes can be found by imagining the single walled carbon nanotube to consist of a cut out sheet of graphene that is rolled up. A SWCNT can be characterized by its chirality, in which the circumferential direction (around the tube) is expressed by the primitive vectors a_1 and a_2:

$$\begin{aligned} a_1 &= a_{c-c}(\frac{3}{2}\widehat{x} + \frac{\sqrt{3}}{2}\widehat{y}) \\ a_2 &= a_{c-c}(\frac{3}{2}\widehat{x} - \frac{\sqrt{3}}{2}\widehat{y}) \end{aligned} \tag{3.13}$$

where a_{c-c} is the carbon-carbon distance of 0.144 nm. An (n,m) nanotube means that the chiral vector is $C_h = na_1 + ma_2$, which is demonstrated for a (4,2) nanotube in Fig. 3.4. The dotted line is the unit cell of the nanotube and the vector T is in the direction of the continuous wavevector along the length of the nanotube, which can go from a few nanometers up to centimeters.

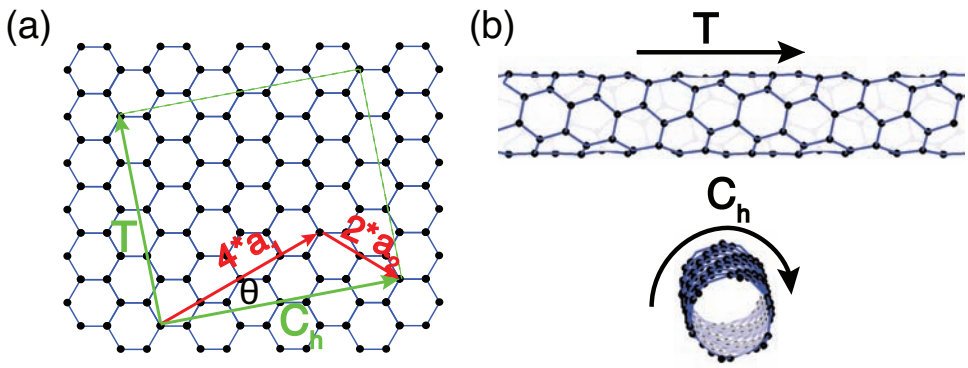

Figure 3.4: Rolling up a sheet of graphene into a carbon nantoube. (a) Showing the chiral vector C_h and the translational vector T written in terms of the unit vectors for the (4,3) carbon nanotube. (b) The same vectors of the rolled up carbon nanotube.

Due to the small dimension in the chiral direction, a new boundary condition exists in this direction and the wavevector is discretized. By calculating the reciprocal lattice vectors and applying the boundary condition, the energy dispersion of the carbon nanotube can be found. This has been done in [110] and leads to the dispersion relationship:

$$E_{cnt}(k) = E_{graphene}(kK_2 + \mu K_1) \tag{3.14}$$

Where K_1 and K_2 are the reciprocal lattice vectors and k is the new wavevector with the condition $\pi/T < k < \pi/T$ and u is an integer between 0 and N-1 where N is the number of hexagonals per nanotube unit cell. Since μ is discretized, the dispersion will consist of discrete subbands shown in Fig. 3.5a for a (10,0) nanotube. This tube is semiconducting since the subbands do not pass through the K or K points shown in Fig. 3.5b. In general, metallic nanotubes have a n-m value that is a multiple of 3, so any (3n,0) nanotube is metallic, also called zigzag nanotube, or any (n,n) nanotube is metallic, also called armchair.

The density of states (DOS) can be calculated by

$$D(E) = \sum_u D_u(E) = \sum_u \frac{dN_u}{dk}\frac{dk(E)}{dE} \tag{3.15}$$

Here, $\frac{dN_u}{dk}$ is $\frac{2L}{2\pi}$ where L is the length of the tube. In Fig. 3.6a, the density of states has been calculated for a (9,0) SWCNT, which is expected to be metallic. The DOS show

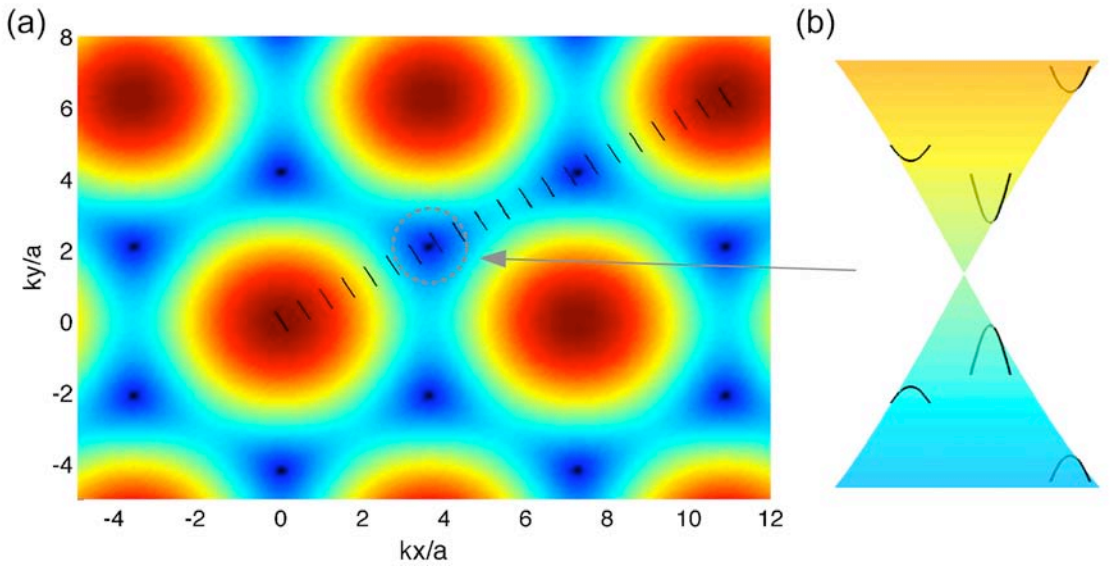

Figure 3.5: Energy dispersion in carbon nanotube. (a) Discrete energy bands of (10,0) nanotube (b) Closeup at Dirac point. Since the (10,0) nanotube is semiconducting, the energy bands do not intersect at the Dirac point.

that there is a subband at zero energy and the conductance and valence band are touching. The (10,0) nanotube clearly shows a bandgap since the DOS is zero at zero energy show in Fig. 3.6b. It is interesting to note that there are energies where the DOS diverge. These are called van Hove singularities and characteristic of one-dimensional systems. Such a singularity appears when a subband threshold is passed. Theoretical density of states can be verified through STM [116] and through optical absorption and emission [117, 118].

A simple approximation for the one dimensional density of states was derived by [119]. The 1D nanostructure has quantized energies in the x and y dimensions given by $E_{i,j}$ where i and j are the quantum numbers for the quantized energies. Assuming that the z direction is continuous, the dispersion can be written as

$$E = E_{i,j} + \frac{\hbar^2 k^2}{2m} \tag{3.16}$$

From Eqn. 3.15, the density of states for a subband can be written as

$$D_{i,j}(E) = \frac{2L}{\pi}\sqrt{\frac{m}{2\hbar^2(E - E_{i,j})}}. \tag{3.17}$$

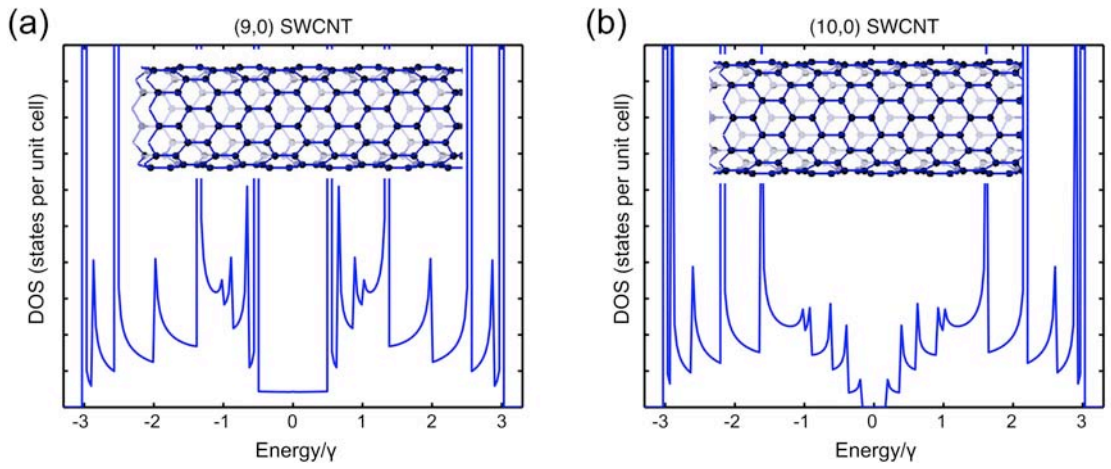

Figure 3.6: Density of States.(a) for the metallic (9,0) nanotube and (b) for the semiconducting (10,0) nanotube with a clearly visible energy gap.

Now using the carrier velocity $\nu(k) = \frac{1}{\hbar}\frac{dE}{dk}$, the density of states for a subband can be written as

$$D_{i,j} = \frac{4L}{h\nu_{i,j}}. \tag{3.18}$$

This equation will be used later to derive the quantum capacitance for carbon nanotubes.

3.4 Carbon nanotube conductance

The current through an ideal 1D conductor can be calculated using the following expression [110, 120]

$$I = \frac{2e}{h}\int [f(E-\mu_1) - f(E-\mu_2)]M(E)T(E)dE \tag{3.19}$$

where M(E) is the number of conduction channel, f(E) is the Fermi Dirac distribution, given by $f(E) = 1/(1+e^{\frac{E}{kT}})$, $2e/h$ is the quantized conductance and T(E) is the transmission probability. Eqn. 3.19 can be used to calculate the current for any 1D transport regime where effects from contacts, barriers or scattering are included in the transmission probability. To illustrate the different transport regime, the following sections

discuss ballistic transport, diffusive transport and transport through a barrier.

3.4.1 Ballistic carbon nanotube ($L < L_M$)

At zero temperature, ideal transmission (T(E)=1) and two available energy bands (since the conduction and valence band are touching at the Dirac points), the above expression simplifies to $I = \frac{4e^2}{h}\frac{\mu_1 - \mu_2}{e}$, which can be written as

$$R = \frac{h}{4e^2} = 6.5\ k\Omega\ (G = 1/R = 153\ \mu S). \tag{3.20}$$

This model is valid for a short carbon nanotube less than the mean free path ($L < L_M$) with perfect contacts to the channel. By using ohmic contacts to the nanotube at short channel length, it was shown that the device behaves like an ideal ballistic conductor [121]. The concept that a ballistic conductor should have a finite resistance seems counterintuitive. However, the current has to be redistributed from many modes at the contacts to only a few modes inside the 1D conductor, which leads to a interface resistance [122]. In a perfectly ballistic 1D conductor, both contacts will have equal contributions to the resistance and there is no resistance drop inside of the conductor, which is demonstrated in the voltage profile in Fig. 3.7a.

3.4.2 Diffusive carbon nanotube ($L > L_M$)

In a real crystal, there are imperfections such as impurities and lattice vibrations, which interfere with the carriers in the channel. Therefore the electrons (or holes) can collide and transfer momentum by scattering. This leads to the concept of mean free path (L_M), which describes the distance that a carrier can travel before undergoing a collision. Eqn. 3.19 above can be modified to take the diffusive component into account. Purewal *et al.* [123] showed that the diffusive component of the resistance increases linearly with channel length, so that the resistance will be

$$R = \frac{h}{4e^2}(\frac{L}{L_M} + 1) \tag{3.21}$$

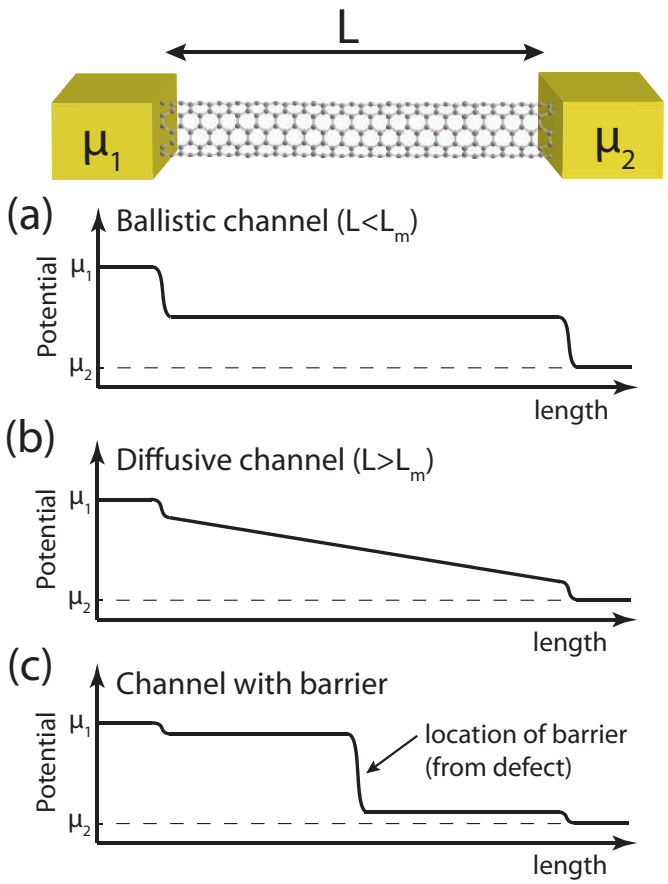

Figure 3.7: Conductance profile. for (a) a ballistic channel, (b) diffusive channel and (c) channel with barrier.

The diffusive component scales with temperature and saturates to a finite value at low temperatures. This happens because ineleastic scattering is due to acoustic phonons and the phonon modes freeze out. It was shown both experimentally [123] and theoretically [124] that metallic carbon nanotubes are insensitive to long range disorder whereas semiconducting carbon nanotubes are not. Therefore the mean free path of metallic carbon nanotubes is much longer (on the order of μm) compared to semiconducting nanotubes (more than 1 order of magnitude lower). As shown in the voltage profile in Fig. 3.7b, a carbon nanotube with diffusive transport will have a finite resistance at the contacts and the channel also has a finite resistance. In a practical device, the contacts are not completely transparent so that another contribution to the resistance is due to small barriers between the contacts and the channel. The total resistance will be

$$R = \frac{h}{4e^2}(\frac{L}{L_M} + 1) + R_c \tag{3.22}$$

where the value of R_c depends on the metal that is used for the contact and also on work function difference and wetting [125]. Some of the lowest contact resistance to carbon nanotubes have been achieved using palladium [121].

3.4.3 Carbon nanotube with barrier

Because single-walled carbon nanotubes have all their atoms at the surface, the perfect crystalline lattice can be disturbed relatively easily. If the nanotube is a ballistic conductor with a single barrier, it was shown by Landauer et al. [126] that the resistance of the barrier for a single channel can be expressed by

$$R_{barrier} = \frac{h}{e^2}\frac{1-T}{T} \tag{3.23}$$

where T is the transmission probability and 1-T is the reflection probability at the barrier. The barrier can be the result of a defect due to a Stone-Wales defect, adatoms, lattice vacancies, electrostatic pn junctions and pn junctions due to chemical doping. The total resistance in the device can be expressed as

$$R_{total} = R_{barrier} + R_c + R_Q = R_c + \frac{h}{4e^2}(1 + \frac{1-T}{T}). \tag{3.24}$$

If the barrier is large, the device resistance will be dominated by the scattering at the defect so that the potential will mostly drop across the defect as seen in Fig. 3.7c.

3.5 Summary

The electronic properties of carbon nanotubes have been reviewed in this chapter. The dispersion in graphene and carbon nanotubes was derived leading to carbon nanotubes with metallic and semiconducting properties. Also, a qualitative picture of transport through a carbon nanotube with a defect has been given, which is going to be useful in the later

chapters. This defect accounts for a large percentage of the resistance in the channel so the carbon nanotube device is very sensitive to the location of the defect. Also, a simple expression for the density of states in terms of the carrier velocity has been given which will be later used for calculating the quantum capacitance.

Chapter 4

Carbon nanotube synthesis and integration

4.1 Introduction

In 1993, two different groups demonstrated the first growth of single-walled carbon nanotubes with a relatively small diameter distribution [127, 128], which created tremendous excitement because theoretical calculations had already been done to show the outstanding electrical [129] and mechanical [130] properties of these novel structures. Control of diameter and chirality is crucial to characterize the properties of carbon nanotubes and eventually use them as building blocks for applications. Three different growth techniques have been mainly used since then, which are arc-discharge, laser ablation and chemical vapor deposition (CVD) [131]. Both arc-discharge and laser ablation use solid-state carbon sources (graphite powder). Synthesis is done at high temperatures (1200°C) with a high-energy source such as a plasma or laser, which results in relatively high quality carbon nanotubes. While there are also large amounts of byproducts such as metal catalyst, amorphous carbon and carbon fibers, these methods are good for bulk production of carbon nanotubes and can yield a small distribution of diameters in large quantities.

Chemical vapor deposition has been mainly used to create high quality nanotube

devices for electronic measurements on solid substrates. In this method, hydrocarbon gases such as ethanol, methanol, ethylene and acetylene are used a sources for the carbon material and the nanotubes are grown from catalyst seed particles such as iron, cobalt and nickel at lower temperatures (500-1000 °C) [131, 132]. The diameter of the grown carbon nanotube matches approximately the diameter of the catalyst particle from where it starts to grow out with a dome-closed end. The advantage is that the nanotubes will adhere to the substrate after growth by van der Waals forces. The nanotube location and density of the films can be approximately controlled by patterning the catalyst particles and also by varying the catalyst density and growth conditions.

4.2 Techniques for assembly and integration of carbon nanotubes

Several problems arising from the bottom up assembly of carbon nanotubes have slowed down their progress and have limited their use in commercial products. First of all, the crystal structure of the nanotubes during growth cannot be reliably controlled. Even through the existing techniques are able to get high yield of single walled carbon nanotubes, there are still multiwalled nanotubes and small bundles of nanotubes in the products. Also the chiral angle and diameter of the nanotubes cannot be precisely controlled so that both metallic and semiconducting tubes exist after synthesis. This makes their use in electronic application impractical since there will be metallic in parallel with semiconducting nanotubes, which cannot be fully depleted resulting in a poor transistor behavior with high off currents. Second, the exact placement of nanotubes cannot be perfectly controlled during growth. By patterning the catalyst during CVD, some control of nanotube location can be achieved but the length and direction of the growth is fairly random. More recently, it was demonstrated that well aligned, dense arrays of nanotube can be grown on quartz substrates with as many as 1 nanotube per 100 nm on average [133]. Third, the growth substrate (quartz, silicon, silicon with thin oxide film) is not necessarily the same substrate

as the final application. For example, carbon nanotubes have shown their potential as thin film transparent electrodes on flexible plastic substrates. Another application is as interconnects or vias for standard complementary metal-oxide-semiconductor (CMOS) chips. None of these substrates are compatible with the growth temperatures of high quality carbon nanotube synthesis [134]. The plastic substrate would simply melt and the CMOS chips cannot sustain the thermal stress and also diffusion of dopants, which the high temperatures would cause.

In order to overcome these difficulties, techniques to both control the carbon nanotube assembly and also to transfer them to a different substrate are necessary. In particular with regard to this thesis, being able to integrate carbon nanotube sensors with active CMOS substrate chips would have several advantages. First, the CMOS chip could multiplex many different devices on an electrode array and therefore many different devices could be measured simultaneously. For example, if the high-density array from the quartz growth could be transferred to a CMOS chip with an electrode array with a 10 μm spacing (electrodes of 7.5x7.5 μm^2 with 2.5 μm gaps patterned afterwards) which connects to the underlying circuitry, as much as 400x400=160000 devices could be measured in a 4x4mm^2 area. The chip could therefore be used to locate the randomly grown and transferred nanotubes and measure their electronic properties. The second reason to integrate carbon nanotube sensors directly with a CMOS substrate is to reduce parasitics in the electrodes and cables. This could tremendously increase the bandwidth and lower the amplifier noise so that very high kinetics could be measured (see Chapter 2). In the following section, different available transfer and alignment techniques for carbon nanotubes will be discussed.

4.2.1 Spin-on

In the early days of carbon nanotube research, carbon nanotubes grown from arc discharge or laser ablation were suspended in solvents such as acetone or dichloroethane and then spin onto an insulating substrate [135–137] because CVD synthesis was not available. Nanotubes in these suspensions were often short ($< 1\mu m$) and assembled primarily in

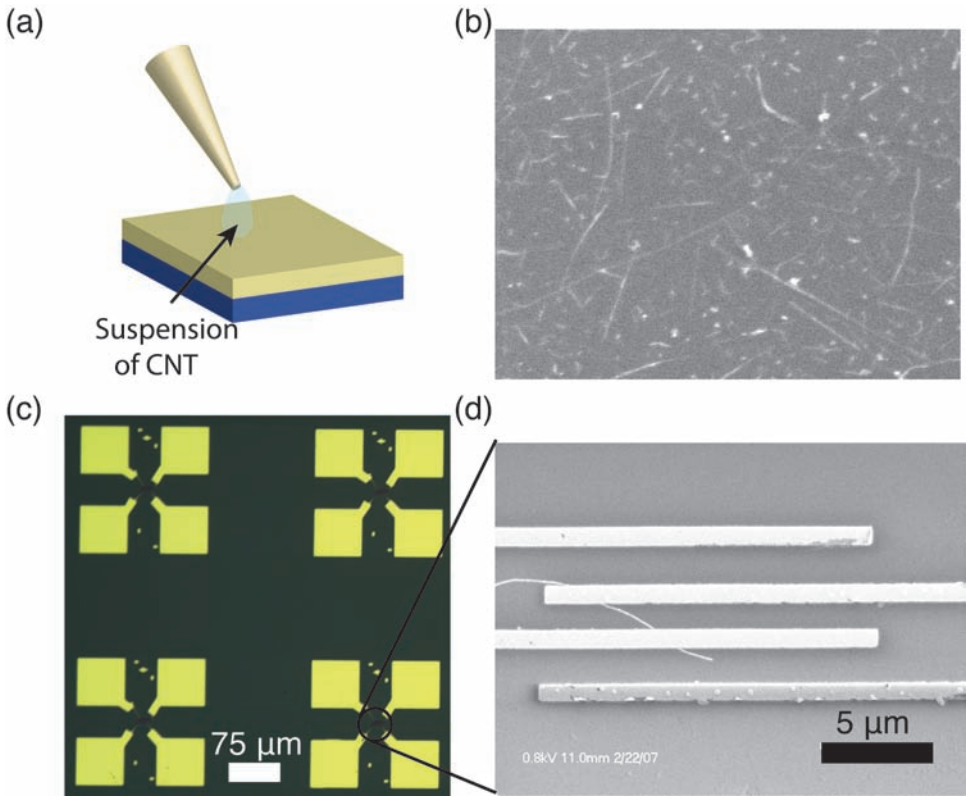

Figure 4.1: Spin on process. (a) Nanotube suspension is spun onto the chip. (b) SEM image of chip surface after spinning showing randomly distributed nanotubes. (c) Optical image of metal electrode array which leads to nanotubes bridging electrodes in (d).

bundles and ropes depending on the solvent used. By using alignment markers on the substrate, single nanotube ropes could be located and connected by metal electrodes for electronic measurement. This method is straightforward but fairly time consuming because the individual nanotubes have to be located.

Another way to make devices is to create random arrays of electrodes after the nanotubes have been spun onto the substrate (Fig.4.1 a). Carbon nanotubes grown by the arc discharge method have been suspended in Dichloroethane and then spun onto a silicon chip with a thin thermal oxide (285 nm). Metal electrodes are then patterned in arrays as shown in the optical image in Fig. 4.1b and c. By tuning the nanotube concentration in the suspension and the spinning process, several electrodes will be bridged by a single carbon nanotube shown in the scanning electron microscope image in Fig. 4.1d.

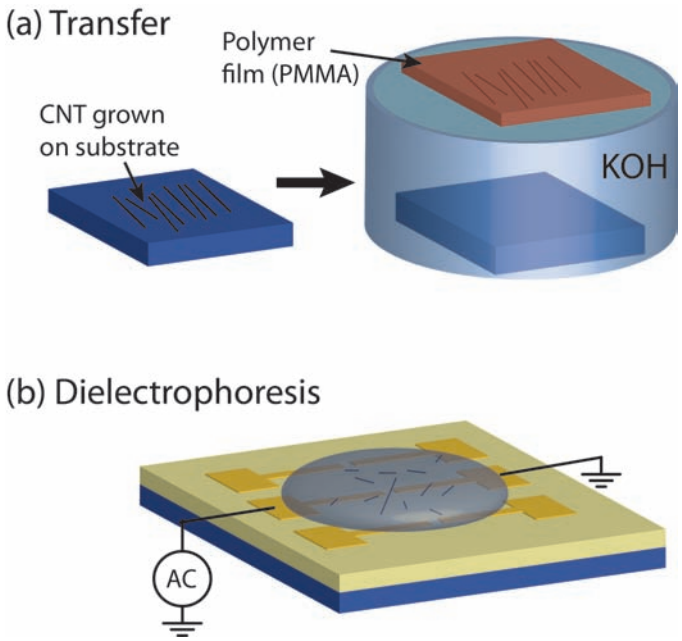

Figure 4.2: (a) Transfer process of carbon nanotubes grown on surface with polymer film. (b) Schematic of alternating current dielectrophoresis for alignment of nanotubes between metal electrodes.

4.2.2 Polymer film transfer

Arrays of carbon nanotubes grown by CVD on regular substrates have been successfully transferred using three different methods. In the first method [138], a thin polymer film such as polymethylmethacrylate (PMMA) is spun on the substrate with nanotubes and baked to encapsulate the nanotubes in the film. The film can be peeled off in basic solution (1M KOH) by hydrolyzation as shown in Fig. 4.2a and can be transferred to a different substrate. In another method [139], a stamping mold made from polydimethylsiloxane (PDMS) is used to pick up nanotubes and then transfer them to a different substrate with a high surface energy to peel the nanotubes off. This can be achieved by oxygen plasma and vapor silanization. In the third method [140, 141], a thin gold film is evaporated onto the carbon nanotubes. Because gold does not adhere well to the substrate, the film together with the nanotubes can be picked up by a thermal release tape or PDMS stamp and transferred to a different substrate. Gold etch is then used to dissolve the gold film and leave the nanotubes on the receiving substrate.

4.2.3 Dielectrophoresis

Both transfer and spinning approaches do not provide substantial control over the precise positioning and alignment of carbon nanotube. As an alternative, radio frequency dielectrophoresis (DEP) can be used to align polarizable nanotubes through gradients in an applied electric field [142] as shown in Fig. 4.2b . The dielectrophoretic force on a ballistic nanotube can be expressed as [143]

$$F_{DEP} = \epsilon_m \frac{\epsilon_p - \epsilon_m}{\epsilon_p + 2\epsilon_m} \nabla E^2 \tag{4.1}$$

where ϵ_p and ϵ_m are the dielectric constants of the particle and medium and is the magnitude of the electric field. Metallic SWCNTs have a very large dielectric constant ($\epsilon_p \gg \epsilon_m$) so that the dielectrophoretic force is always positive for any tube ($F_{DEP} \approx \epsilon_m \nabla E^2$). Semiconducting nanotubes, however, have a dielectric constant that varies with their bandgap as $\epsilon_p \approx 1 + (\frac{\hbar\omega_p}{5.4E_g})^2$ [142]. Assuming $E_g = |\xi|\frac{a_{cc}}{d}$ with the energy of the plasma frequency $\hbar\omega_p = 5eV$, the graphite overlap integral $|\xi| = 2.5eV$ and the carbon nearest neighbor distance $a_{c-c} = 0.142$ nm, F_{DEP} is a strong function of diameter. If $\epsilon_p < \epsilon_m$, the dielectrophoretic force is negative, which will repel any particle. This puts an upper limit on the dielectric constant so that the dielectric force will be positive for diameters $d > \sqrt{\frac{\epsilon_m - 1}{6.76}}$. In order to trap nanotubes down to 1.2 nm, a dielectric constant of the medium has to be below 10.8.

The simulated ∇E^2 is shown in Fig. 4.3a for an applied bias of 2.5 V between two electrodes and a dielectric constant of 10.3 (for dichloroethane) on top of a glass substrate, showing the magnitude and direction that the force is pulling the particle between the electrodes. Another configuration is to apply the time varying field between one electrode and the substrate, which creates a force perpendicular to the electrode as shown in Fig. 4.3b. Both methods have been used to align carbon nanotubes specifically between one pair of electrodes or randomly along a single electrode.

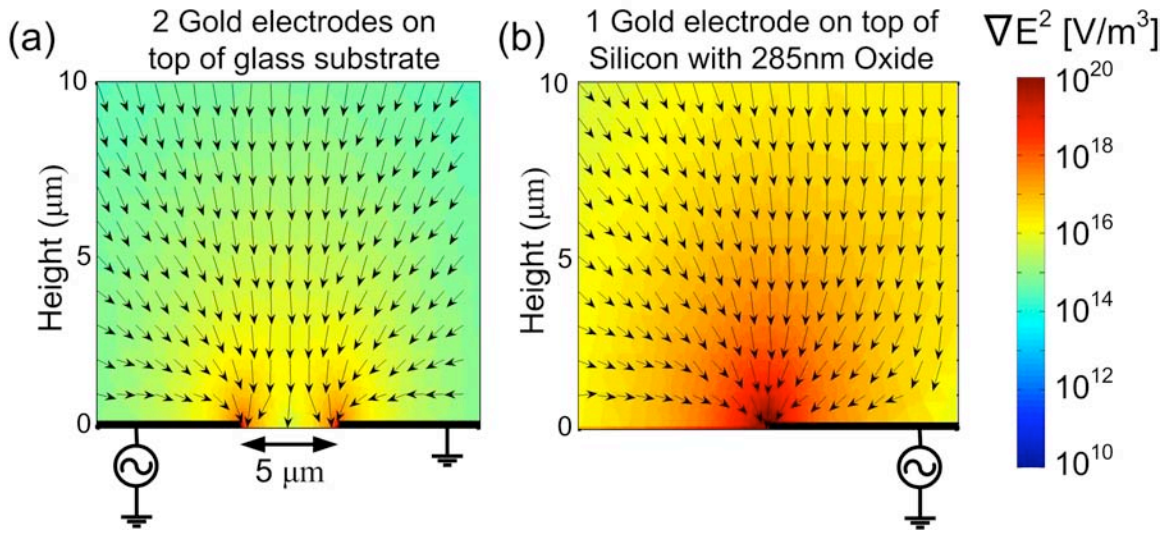

Figure 4.3: Simulation of ∇E^2 in Eq. 4.1 for two different geometries. In (a) two electrodes are on top of a glass substrate. (b) shows the fringing field for a single electrode with a silicon substrate and a thin oxide.

4.3 DEP with carbon nanotubes

In order to achieve the goal of bridging two electrodes with an individual single-walled carbon nanotube with high yield, several parameters need to be optimized.

4.3.1 Nanotube Suspension

For random spinning on nanotubes and dielectrophoresis, a crucial part is making a good suspension of nanotubes. Even if the growth yielded perfect control over the nanotube chiralities, nanotubes tend to aggregate into bundles and ropes because of their high van der Waals binding energy [144]. Since carbon nanotubes are non-polar, they can best be suspended in non-polar solvents or polar aprotic solvents such as dimethylformamide [142], dichloroethane [145] and chloroform [146]. Another way is to use polar solvents or water in combination with surfactants such as sodium dodecyl sulfate (SDS) [144] to coat the nanotubes and result in well dispersed suspension.

The carbon nanotubes used in this experiment were synthesized by the arc discharge method (from Carbon Solutions) and dispersed in 1,2 dichloroethane (DCE) by ultra-sonication for 2 h and centrifugation at 8000 rpm for 2 h, resulting in a concentration

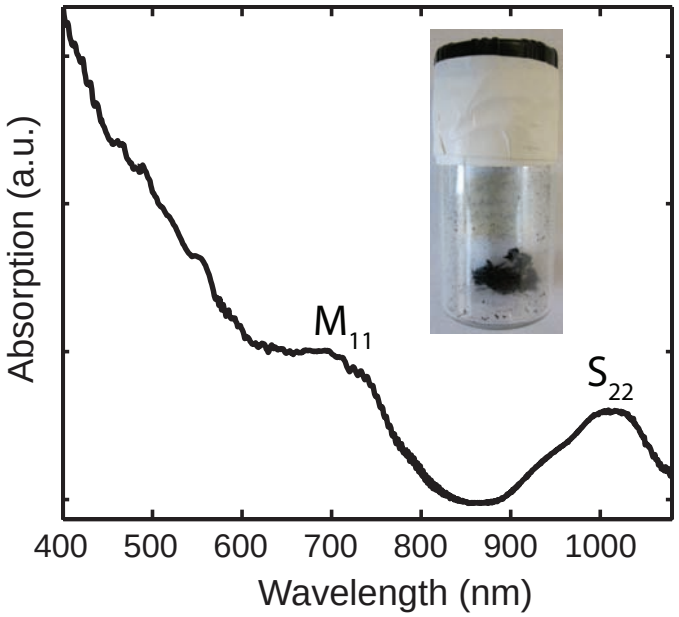

Figure 4.4: UV-Vis absorption of carbon nanotube suspension using 1,2 Dichloroethane. The inset shows the nanotube raw material after synthesis.

of approximately 6 ng/ml. DCE has a dielectric constant of 10.3, which leads to a positive DEP force for semiconducting nanotubes with diameters greater than 1.2 nm. The quality of the suspension is verified by ultraviolet to visible absorption (UV-Vis), which is shown in Fig. 4.4. Three distinct absorption peaks are visible (after subtracting the DCE background), which are attributed to the pairwise excitations in the density of states between van-Hove singularities [142]. There is a S_{22} peak for the 2nd semiconducting excitation bands and the M_{11} for the 1st metallic excitation bands. The UV-Vis data is comparable to published data for suspensions containing both metallic and semiconducting nanotubes. DCE suspension allows surfactants to be avoided, which coat the nanotubes and affects contact resistance. Several other solvents were tried to for suspensions including acetone, isopropanol, ethanol, toluene and methanol but did not result in stable suspensions.

4.3.2 Metal Electrodes

The electrodes for the DEP experiment were fabricated on a glass substrate in order to limit the fringing fields to the susbtrate and reducing the number of tubes attaching to the sides

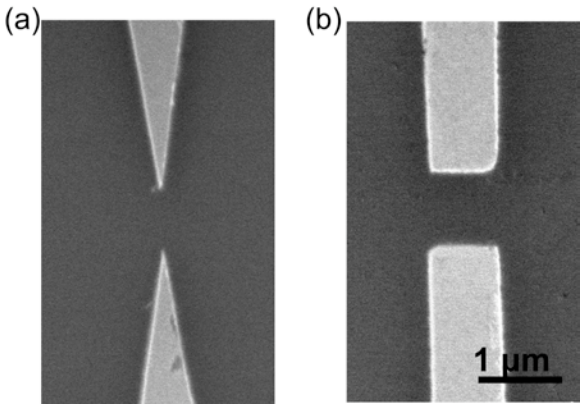

Figure 4.5: Metal electrodes with (a) sharp and (b) square geometry.

of the electrodes away from the gap. Since nanotube length range from 500 nm to 3 μm, a gap of 1 μm was chosen so that most nanotubes can bridge the gap. The electrodes were fabricated by standard electron-beam lithography, metal evaporation of 5 nm chromium and 50 nm gold and lift off in acetone. Both sharp triangular electrodes as well as square electrodes were fabricated as shown in Fig. 4.5. The geometry of the electrodes did not substantially affect the dielectrophoresis process and most of the devices were made from square electrodes. After fabrication, the electrodes are wire-bonded to a standard chip carrier to facilitate the electrical measurments.

4.3.3 DEP parameters

Unlike larger particles such as bacteria, multiwalled nanotubes or nanowires, carbon nanotubes cannot be imaged by an optical microscope in real time while they deposit on the surface. This makes the DEP experiment tedious because it involves an iterative process involving SEM and AFM to optimize the parameters such as applied electric field (or potential), the concentration of nanotubes in the suspension and the time that the field is applied. Qualitatively, Fig. 4.6 shows the effects of these parameters on the number of nanotubes that bridge the gap between the electrodes. The optimum conditions to get a single bridging nanotube is a 1x concentration (around 6 ng/ml) at 2.5 V/μm and 2 minutes application of the field. Doing DEP for longer times, at higher potentials and at higher concentrations increases the number of tubes that bridge the electrode.

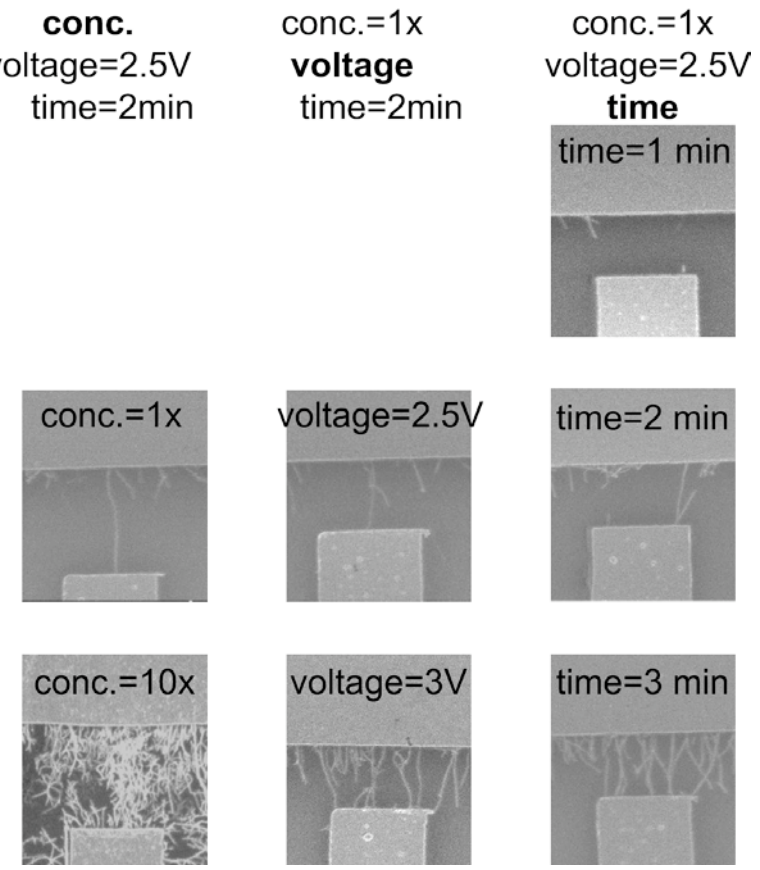

Figure 4.6: Effect on cnt concentration, voltage and time on the yield of trapping a single nanotube between the electrodes. In each SEM image, the bottom electrode is 2 μm wide.

4.4 Use detection system to improve yield of single tubes

A recent report demonstrated the real-time detection of dielectrophoretically trapped multiwalled carbon nanotubes by measuring a decrease in gap impedance [147]. There have been no reports of the *in situ* control of the dielectrophoretic assembly of SWCNTs, which represents a significantly more formidable challenge because of the much smaller dimensions involved, the variability in chirality and the complexity in the measured electrical response. The approach described here not only enables the real time determination of the trapping of a carbon nanotube, but also allows the evaluation of the metallic/semiconducting nature of the trapped species.

The lock-in detection system is shown in Fig. 4.7a and is implemented on a custom printed circuit board as shown in Fig. 4.8, which has been described in [148]. Two ac

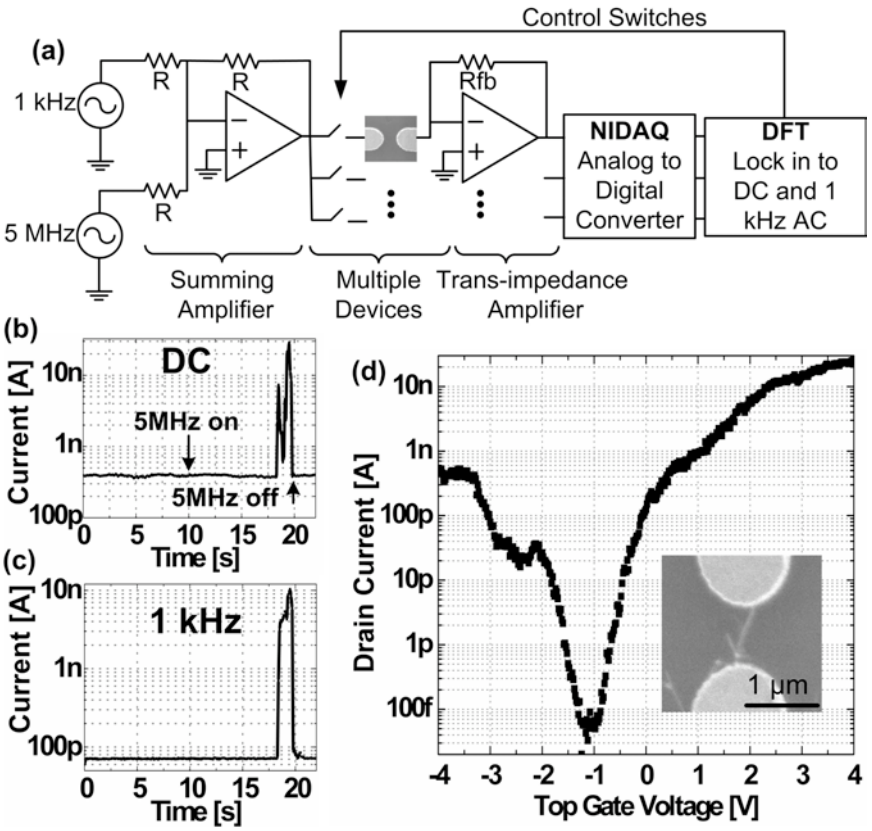

Figure 4.7: (a) Lock-in detection setup allowing DEP to proceed along with real-time measurement. (b,c) Real time measurement during DEP deposition of I_{dc} and I_{ac} respectively. (d) Source to drain current as a function of top gate sweep for the deposited nanotube shown in the inset.

potentials are superimposed through a summing amplifier: a signal at $f_2 = 5$ MHz, which is used to manipulate the carbon nanotubes, and a signal at $f_1 = 1$ kHz, with a constant 100 mV amplitude. Both the dc (I_{dc}) and f_1-component (I_{ac}) of the device conductance are monitored in real time.

For the DEP protocol, a small drop of the nanotube suspension (40 μL) is introduced onto the chip at the area of the electrodes. The 2.5 V 5 MHz signal is turned off less than 2 seconds after a change in both I_{ac} and I_{dc} is observed, avoiding the deposition of multiple tubes across the gap. After deposition, the chip is carefully rinsed with DCE and isopropanol followed by a gentle dry in nitrogen. This careful rinsing is necessary because otherwise, the nanotube suspension will dry and nanotubes will be dispersed randomly on the surface. Bridged carbon nanotubes are not removed through rinsing. The devices are imaged with

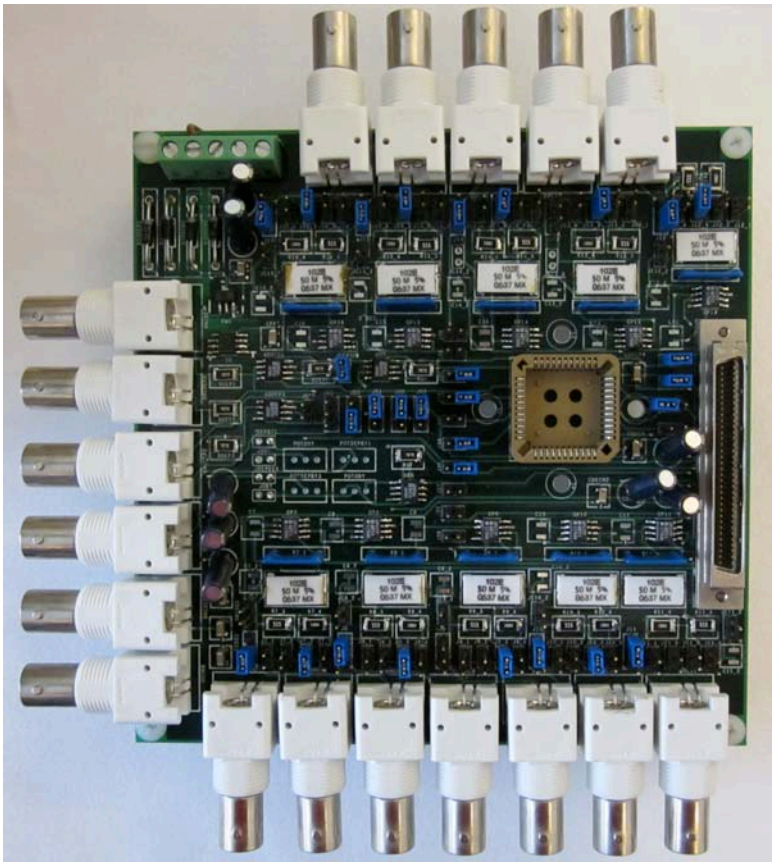

Figure 4.8: PCB board design of DEP system shown in Fig. 4.8a.

a scanning electron microscope (SEM) and atomic force microscopy (AFM) to determine how many nanotubes bridge each electrode pair. The electrical properties of the deposited nanotubes are independently characterized by creating a top gate by depositing 15 nm of hafnium oxide by atomic layer deposition and a gate electrode through electron-beam lithography.

The results from a representative DEP deposition are shown in Fig. 4.7b-d. Fig. 4.7b-c show I_{ac} and I_{dc} as a function of time; deposition stops at t=20 s. A clear change in the current magnitudes is evident at t=18 s as the electrodes are connected by a deposited nanotube. The SEM image of the inset in Fig. 1d confirms that a single tube (or small bundle) connects the electrodes. Fig. 4.7d shows the subthreshold characteristics of the deposited nanotube device at Vds = 0.1 V, demonstrating an I_{on}/I_{off} ratio of 10^5 and a subthreshold slope of 240 mV/decade. Contact resistances generally range from 500 kΩ-10

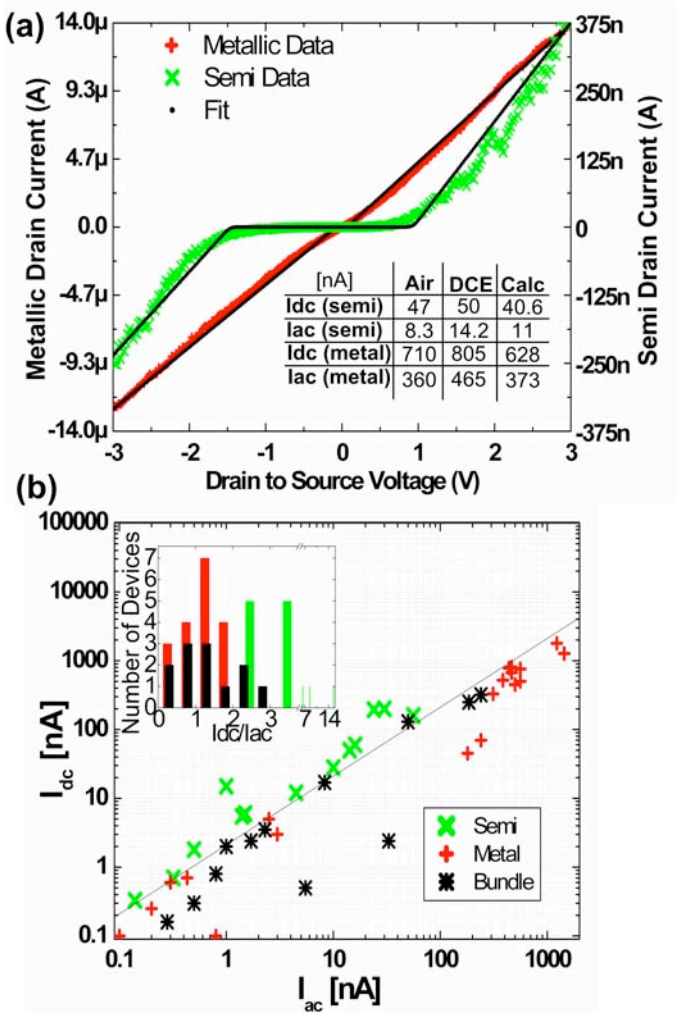

Figure 4.9: (a) Drain current (I_{ds}) as a function of drain to source voltage (V_{ds}) for a typical semiconducting and metallic carbon nanotube. Measured data and the associated fit to Eq. 4.2 are shown. (b) Distribution of I_{ac} and I_{dc} values for 43 representative nanotube devices.

MΩ, consistent with other reported results for gold bottom contacts [149].

In order to understand the increase in I_{ac} and I_{dc} when a nanotube bridges the electrodes, the nanotube device is modeled as a Schottky barrier with a series resistance, so that the current-voltage characteristics of the nanotube can be approximated by [150, 151]:

$$I = \frac{k_B T}{qR_D} \ln\left[1 + \frac{I_{0D} q R_D}{k_B T} e^{\frac{qV}{k_B T} + \frac{I_{0D} q R_D}{k_B T}}\right] - I_{0D} + \frac{k_B T}{qR_S} \ln\left[1 + \frac{I_{0S} q R_S}{k_B T} e^{\frac{qV}{k_B T} + \frac{I_{0S} q R_S}{k_B T}}\right] + I_{0S} \quad (4.2)$$

where R_D and R_S are the resistance of drain and source, I_{0D} and I_{0S} are the diode drain and source saturation currents, q is the electric charge, V is the applied drain-to-source

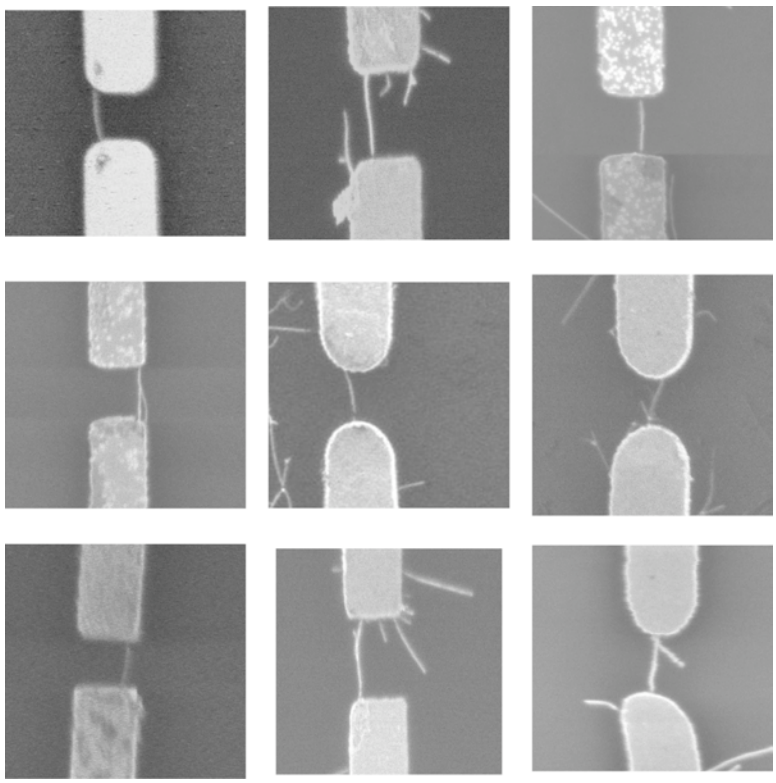

Figure 4.10: SEM image of carbon nanotube devices deposited by the DEP detection system.

bias, T is the temperature, and k_B is Boltzmanns constant. In Fig. 4.9a, this equation is fit to a high bias drain to source sweep of a representative semiconductor and a representative metallic nanotube with I_{0D}, I_{0S}, R_D, and R_S as fitting parameters. Because the saturation currents I_{0D} and I_{0S} increase exponentially with decreasing barrier height, one finds that for metallic nanotubes, $I_{0D} \gg \frac{k_B T}{q R_D}$ and $I_{0S} \gg \frac{k_B T}{q R_S}$. In this case, a nearly linear relation results with $I \approx V/R_D$ for $V > 0$ and $I \approx V/R_S$for $V < 0$.

In contrast, semiconducting nanotubes have large, unequal source and drain barriers, resulting in very nonlinear and asymmetric current-voltage characteristics. We can use Eq. 4.2 and a Fourier analysis to estimate the I_{dc} and I_{ac} values that result from the applied potential $V = A_{1kHz}cos(2\pi f_1 t) + A_{5MHz}cos(2\pi f_2 t)$. The table in Fig. 4.9a shows the calculated values that result for the two characterized tubes. These match closely those measured in air and in DCE before creating the top gate. Large I_{ac} values are observed when the electrodes are bridged in Fig. 4.7c due to the fact that the large-amplitude 5 MHz signal moves the bias point throughout the whole curve to increase the conductance at f_1

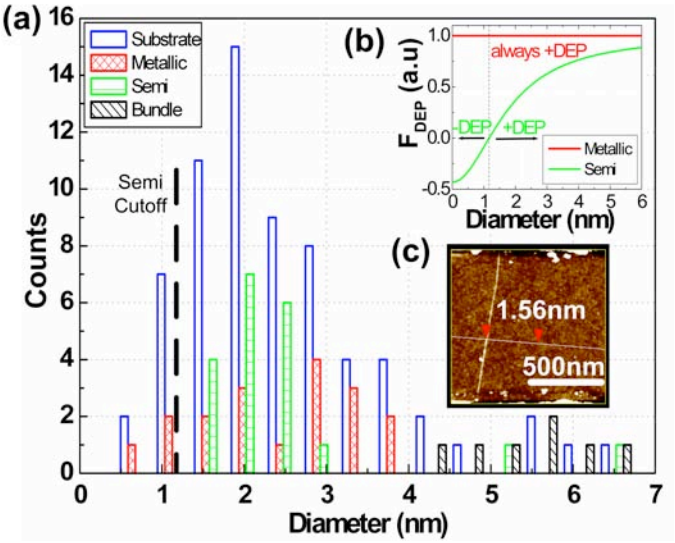

Figure 4.11: Diameter distribution for nanotubes randomly dispersed on substrate and metallic, semiconducting and bundled nanotubes deposited by DEP. (b) Claussius Mosotti function for metallic and semiconducting nanotubes. (c) A representative AFM image of a single tube.

even for semiconducting devices that do not have significant conduction for small, applied biases.

In Fig. 4.9b, the results for 43 representative devices are plotted as a function of I_{dc} and I_{ac}. Semiconducting nanotubes are characterized by I_{on}/I_{off} ratios greater than 3 as measured for top-gated field-effect structures fabricated from these nanotubes with $I_{off} < 10$ pA, while metallic nanotubes are characterized by I_{on}/I_{off} ratio of 3 or smaller. Devices with I_{on}/I_{off} ratios in excess of 3 but without a bandgap ($I_{off} > 10$ pA) are called bundles. The inset of Fig. 4.9b indicates how the I_{dc}/I_{ac} ratio can be used to distinguish metallic from semiconducting tubes during DEP. I_{dc}/I_{ac} ratios of greater than 2 are a confident indicator of semiconducting tubes, while I_{dc}/I_{ac} ratios of less than 2 are a confident indicator of metallic tubes or bundles.

Fig. 4.10 show a few deposited carbon nanotube devices. Fig. 4.11a shows the distribution of tubes randomly dispersed on a substrate (labeled "substrate") and the distributions of metallic, semiconducting and bundled nanotubes, as characterized by their electronic properties, which are deposited by DEP. We only count devices with a single bridging nanotube as verified by AFM (Fig. 4.11c). The distributions for single nanotubes

are centered around 1.6-2.1 nm indicating that nanotubes are being deposited in a manner that closely matches the original distribution of the nanotube soot [152]. It is important to note that semiconducting nanotubes with diameters less than 1.2 nm are not present, consistent with the prediction of Fig. 4.11b. As a result, there is a slightly higher affinity for metallic tubes, resulting in deposition of metallic to semiconducting tubes in the ratio of 1:1 compared to 1:2 in the original distribution.

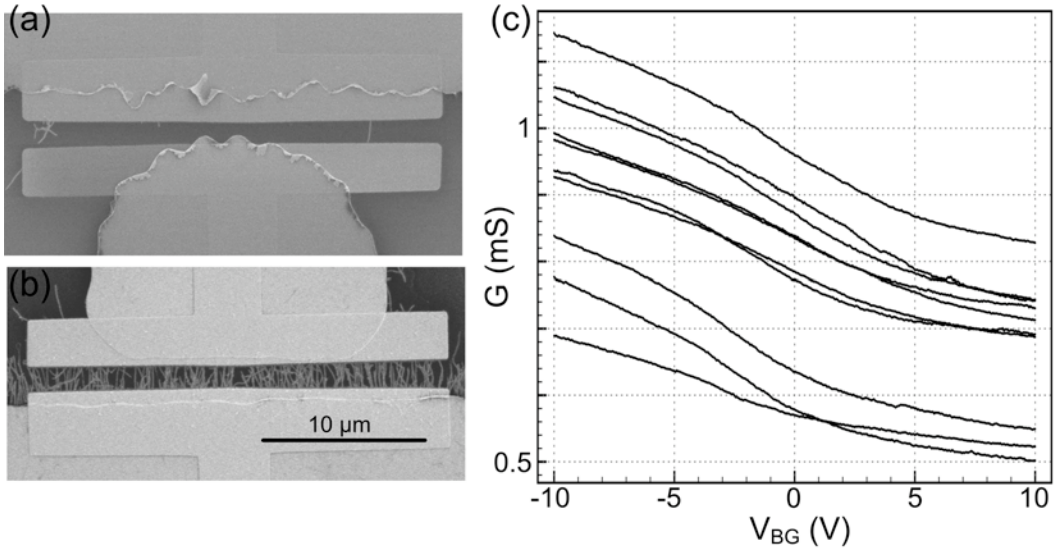

Figure 4.12: Random DEP using parameter for low density of tubes bridging electrodes (a) or high density of bridging tubes (b). These devices have low variability as shown in (c).

4.5 Random DEP for many devices or many tubes

When applying the electric field between an electrode and the substrate, nanotubes will align along the electrode. This can be used to make large arrays of nanotubes and by using different conditions devices with few bridging nanotubes (Fig 4.12a) to many bridging nanotubes (Fig 4.12b) can be achieved. In these devices, carbon nanotubes have been first deposited by DEP on a gold electrode and another palladium electrode has been deposited on top to sandwich the nanotube and the bottom electrode which results in low contact resistances. Fig. 4.12c shows the electronic properties of several devices fabricated in the same processing step. Each of these 25 μm devices is bridged by several metallic and

semiconducting nanotubes, which explains the high off currents. Because the electronic properties are averaged out, the variability between devices is relatively low.

4.6 Summary

In conclusion, several methods have been presented to allow the fabrication of carbon nanotubes on different substrate. This is particularly important for substrate like CMOS chips that cannot withstand the high CVD growth temperatures.

Chapter 5

Pristine carbon nanotubes in aqueous environment

In order to use carbon nanotubes as sensing elements for biosensors, a thorough understanding of their behavior in a liquid environment is necessary. This chapter reviews the metal/electrolyte interface, which can be used to electrolytically gate the carbon nanotube field-effect transistor and reviews the design and fabrication considerations for the nanotube transistor in an aqueous environment. The dominant noise will be measured and an ensemble measurement of protein in solution will be discussed.

5.1 Solid liquid interface

A large part of the electrochemistry field deals with the properties of an electrode/electrolyte interface and in particular with charge transport at the interface [153, 154]. There are in general two types of reaction, a faradaic and a nonfaradaic process. In the faradaic process, an electron charge is transferred through the interface when a chemical reaction happens. Examples are galvanic cells such as fuel cells or batteries in which chemical energy is converted to electrical energy or electrolytic cells, in which an external potential is applied to a chemical cell such as electroplating or recharging of a lead acid battery. In a nonfaradaic process, no charge transfer occurs and the interface itself charges up similar

to a capacitor. In this chapter, the focus will be on the nonfaradaic process to explain how carbon nanotubes can be electrolytically gated. The next chapter will explain how a controlled faradaic process can lead to a chemical oxidation reaction at a single point in the nanotube to create a defect.

An electrolyte is a conducting solution in which charged ions can diffuse (with the exception of solid electrolytes and molten electrolytes). The resistivity of the electrolyte is dependent on the concentration of the ions since the ions are responsible for charge transport. However, the resistance due to the electrolyte is usually small in aqueous electrolytes. The resistivity of phosphate buffered saline (1X PBS), which is the buffer used for the biological measurements in Chapter 6 & 7 is about 0.65 Ωm. In a nonfaradaic process, the metal/electrolyte interface is ideally polarizable so that the potential is dropped across this interface. Several different models for this interface capacitance have been developed since the beginning of the 20th century. One of the most popular models is based on the Gouy-Chapman-Stern model [155]. In this model, the interface capacitance is given by a series combination of the Helmholtz capacitance C_H and the Gouy-Chapman capacitance C_{GC} as

$$1/C_d = 1/C_H + 1/C_{GC} \tag{5.1}$$

The Helmholtz capacitance is the result of the ions having a finite radius so that the ions cannot approach the surface closer than their radius. Due to counterion adsorption to the surface, there will be a potential drop due to that layer so that $C_H = \epsilon\epsilon_0/x_2$. The distance x_2 away from the electrode (same order of magnitude as the ion radius) is called the outer Helmholtz plane. Further out from x_2, the ions will be mobile and can diffuse into the bulk solution. This diffusive layer can be modeled by the Poisson equation [153],

$$\nabla^2\Phi(x) = \frac{\rho(x)}{\epsilon\epsilon_0} \tag{5.2}$$

where the electrostatic potential $\Phi(x)$ is related to the charge density $\rho(x)$. In order to solve Eqn. 5.2, the assumption is made that the ions follow a Boltzmann distribution,

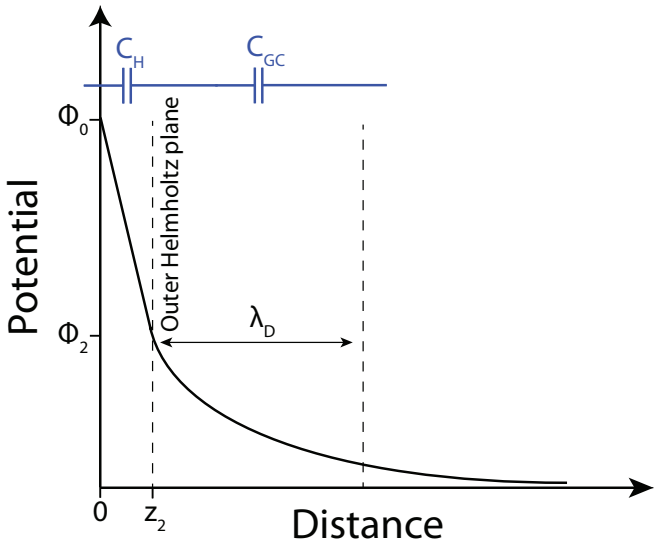

Figure 5.1: Potential profile between a metal electrode and an electrolyte according to the Gouy-Chapman-Stern model.

$$n_i = n_i^0 e^{\frac{z_i e \Phi}{k_B T}} \tag{5.3}$$

where z_i is the charge of ion i and n_i^0 is the bulk ion concentration. Eqn. 5.2 can then be rewritten as the Poisson-Boltzmann equation

$$\nabla^2 \Phi(x) = -\frac{e}{\epsilon \epsilon_0} \sum_i n_i^0 z_i e^{\frac{z_i e \Phi}{k_B T}}. \tag{5.4}$$

Assuming a symmetric electrolyte (only one anionic and one cationic species with equal charge), the equation for the potential is

$$\frac{\tanh ze\Phi_2(x)/4k_BT}{\tanh ze\Phi_0/4k_BT} = e^{-\frac{x}{\lambda_D}}. \tag{5.5}$$

λ_D is the Debye length which will be discussed in more detail in Chapter 7. The Debye length is related to the bulk concentration of the buffer (n_0) such that

$$\lambda_D = \sqrt{\frac{\epsilon \epsilon_0 k_B T}{2 n_0 z^2 e^2}}. \tag{5.6}$$

The potential profile between a metal electrode and an electrolyte is shown in Fig. 5.1. Close to the metal electrode, the Helmholtz layer leads to a linear decrease in the

potential. After the outer Helmholtz plane, the diffusive layer roughly falls off exponentially. The capacitance of this Gouy-Chapman diffusive layer can be written as

$$C_{GC} = \frac{\epsilon\epsilon_0}{\lambda_D}\cosh(\frac{ze\Phi_0}{2k_BT}). \tag{5.7}$$

For small applied potentials (Φ_0), the potential drop can be expressed as an exponential decay with $\Phi(x) = \Phi_0 e^{-\frac{x}{\lambda_D}}$ and the Gouy-Chapman capacitance as $C_{GC} \approx \frac{\epsilon\epsilon_0}{\lambda_D}$. Since C_H and C_{GC} are in series, the smaller capacitance will dominate. At low bias and low buffer concentration, the interface capacitance can be approximated by the Gouy-Chapman capacitance. At high bias and high buffer concentration, the diffusive layer falls off very quickly and the capacitance is dominated by the Helmholtz term.

5.2 Gate and quantum capacitance

As shown in Chapter 3, single walled carbon nanotubes can be metallic or semiconducting, depending on their chirality. If the nanotube is fabricated as a field-effect transistor in a three terminal fashion, a nearby gate electrode can capacitively tune the Fermi level inside the nanotube and change the carrier density inside the nanotube channel. Under ambient conditions, carbon nanotubes are usually p-type, which means that holes carry the electric current in the channel and the Fermi level lies within the valence band. This is most probably due to the metal contacts and also doping from adsorbed chemical species to the sidewall [156]. However, the Fermi level can be changed from the valence band into the bandgap and into the conduction band by increasing the gate voltage. Fig 5.2 shows the energy band modulation in the channel. Because of Fermi level pinning at the source and drain metal electrodes, there will be small barriers at the contacts in n-type operation, which usually limits the electron transport to a lower level than the hole transport.

In a standard carbon nanotube field-effect transistor, the gate usually couples to the channel via a thin oxide. This is usually done by growing the carbon nanotubes on a silicon wafer with a thin thermal oxide ($\sim$ 300 nm) and using the silicon as a back gate. The

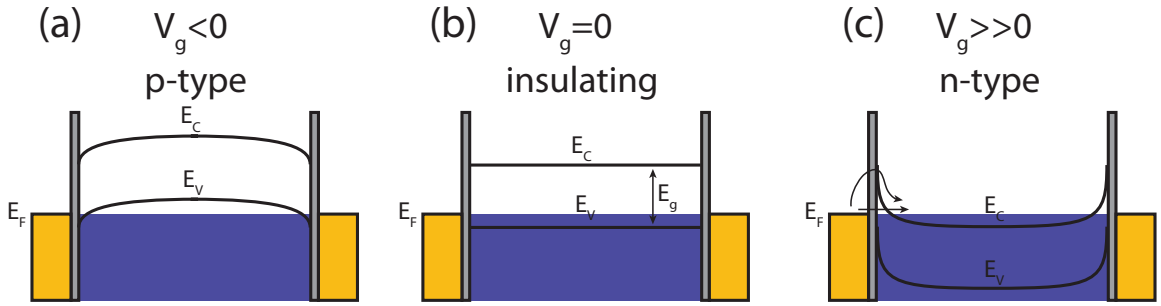

Figure 5.2: Schematic of energy bands as a function of gate voltage. (a) At negative gate voltage, the device is p-type with small barriers at the contacts. (b) At zero gate voltage, this particular device is insulating since the fermi level is inside of the bandgap. (c) At large positive voltages, the energy bands have shifted down so that the device is n-type with large barriers at the contacts.

capacitance to the channel can be modeled as an infinite plane to a cylinder of diameter d, which is distance h apart. The capacitance from this configuration can be derived as [157]

$$C_{ox} \approx \frac{2\pi\epsilon\epsilon_0}{ln(\frac{4h}{d})} \tag{5.8}$$

For a 300 nm SiO_2 oxide, the capacitance comes out to 33.9pF/m. In order to improve the capacitance, the oxide thickness can be decreased and the dielectric constant can be increased. This has been done using high-k dielectrics such as hafnium oxide for ballistic carbon nanotubes [121].

The capacitance in an aqueous environment will be very different. As shown in Section 5.1, the electrode/electrolyte capacitance will be set by the high dielectric constant of water (ϵ=80) and the thickness is on the order of the Debye length. Assuming that the water wraps around the nanotube, the capacitance can be approximated by a coaxial cable with the distance between the inner and outer radius equal to the Debye length so that

$$C_{el} = \frac{2\pi\epsilon\epsilon_0}{ln(\frac{2\lambda_D+d}{d})}. \tag{5.9}$$

This capacitance is about 7.6 nF/m for 1X PBS and more than 200 times larger than the oxide capacitance. However this is not the capacitance that will actually appear at the gate. In low dimensional systems such as the 1D carbon nanotube, the density of states is relatively low, so that there are not enough states that can be filled by the electrolyte

gate. In order to model this capacitance, the geometric capacitance is in series with another capacitance, called the quantum capacitance, C_Q:

$$C_Q = \frac{dQ}{dV} = \frac{edN}{d(E/e)} = e^2 \frac{dN}{dE} = e^2 g(E) \tag{5.10}$$

Not surprisingly, the quantum capacitance is proportional to the density of states. From Eqn. 3.18 in Chapter 3, the quantum capacitance can be written in terms of the Fermi velocity, v_F, so that

$$C_Q = \frac{4e^2}{hv_F} \tag{5.11}$$

Assuming a Fermi velocity of about 8×10^5 m/s, the quantum capacitance is around 386 pF/m. If the nanotube is gated through the oxide, the geometric capacitance is much smaller than the quantum capacitance, so the total gate capacitance is equal to the geometric capacitance. However, with very thin high-k dielectrics or electrolyte gating, the quantum capacitance term is much smaller so that the device is limited by the quantum capacitance. This has been plotted in Fig. 5.3 where the total capacitance is plotted as a function of NaCl concentration. This clearly demonstrates that the quantum capacitance dominates the gate capacitance in electrolyte, even down to very low buffer concentrations. The total capacitance in electrolyte therefore is about 8-11 times larger than the back gate capacitance.

5.3 Device Fabrication

While the transfer techniques discussed in Chapter 4 are necessary for "on-chip" CMOS measurements, the overall process can be reduced by several steps if the nanotubes are not transferred. For the proof of principle carbon nanotube biosensors, the nanotubes are directly grown on a silicon chip with a thin oxide. This allows far better control over the carbon nanotube and several devices per chips can be made from the same chirality tube. The fabrication steps can be divided into four parts, which are nanotube growth, fabrication

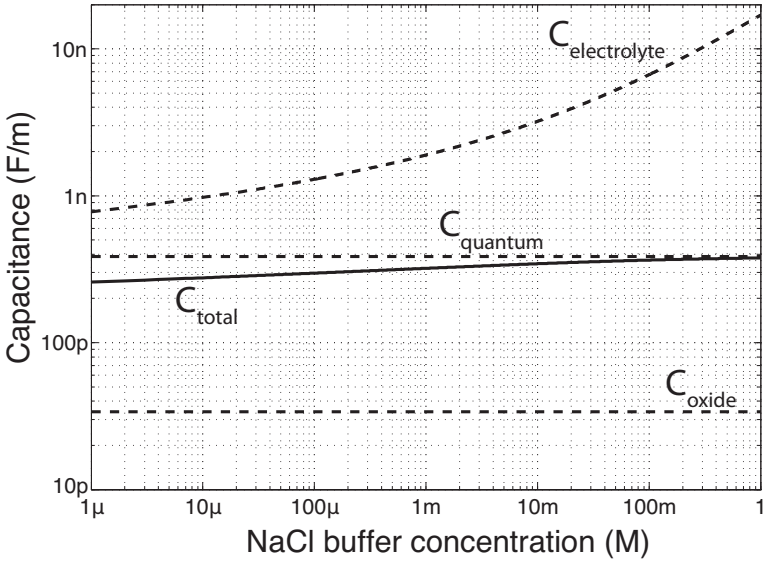

Figure 5.3: Plot of device capacitance as a function of buffer concentration. Since the electrolyte capacitance is always larger than the quantum capacitance, the total capacitance is roughly equal to the quantum capacitance.

to create metal electrodes, nanotube mapping and post processing to define a single tube and cleaning of the chip as shown in Fig. 5.4.

5.3.1 Nanotube growth

The most important part to fabricate the sensor is growing individual single-walled carbon nanotubes. A simple CVD based process has been adopted from [158]. The catalyst solution for the nanotube growth was composed of p-methyl methylacetoxy calyx[6]arene (MC6, Toluyama Corp.) and Fe(III) acetylacetonate ($Fe(Acac)_3$, Aldrich) in monochlorobenzene. A solution of 1.0 wt% MC6 and 0.1 wt% $Fe(Acac)_3$ was carefully brushed onto one edge of a piranha-cleaned SiO_2 substrate (300 nm) and then subjected to a preheated (500°C) furnace for 10 min in air to remove the resist. After flushing the system with argon at the same temperature for 10 min, the temperature was ramped to 750°C and connected to the reducing gases of argon and hydrogen (642 sccm and 115 sccm, respectrively) to activate the iron nanoparticles for 1h. Carbon nanotubes were then grown at 880°C for 1h by chemical vapour deposition (CVD) process from the iron nanoparticles, using ethanol as the carbon

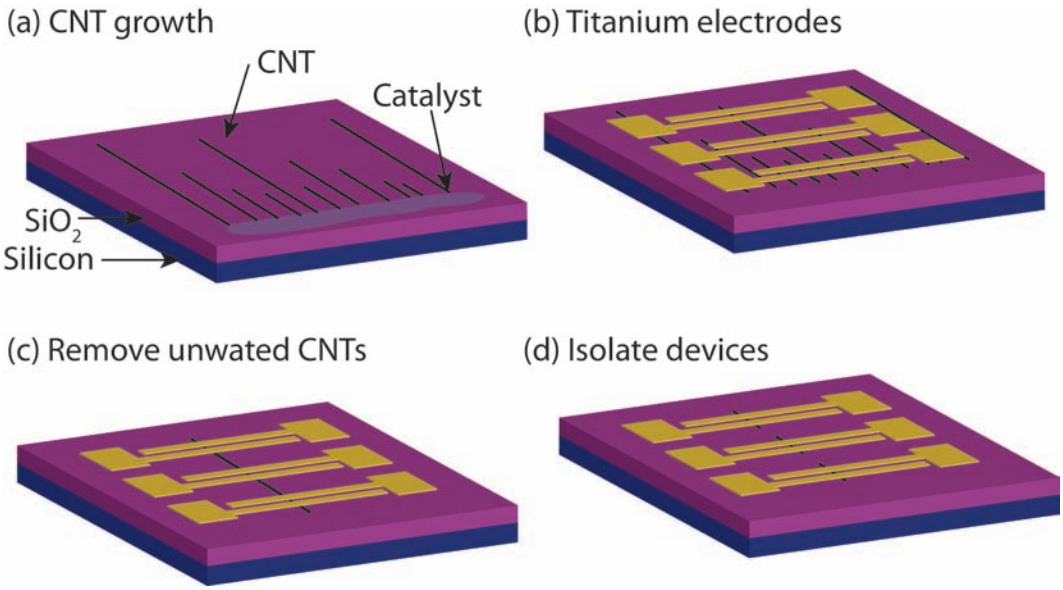

Figure 5.4: Overview of main processing steps. (a) Growth of carbon nanotubes on chip in CVD furnace from catalyst particles. (b) Evaporation of titanium electrodes. (c) After mapping out location of nanotubes, oxygen plasma etch to remove all nanotubes except for one. (d) Also remove nanotube between devices to avoid shorting out all devices during electrochemical oxidation (in Chapter 6)

source [159]. The flow rates for growth were 138 sccm for argon and 18 sccm for hydrogen. In general, the nanotubes grown were several millimeter long (most of them were much shorter) and had a spacing of around 50-200 μm as shown in Fig. 5.5a.

5.3.2 Metal electrodes

For device fabrication, nanotubes were grown on degenerately doped silicon substrates ($\rho = 0.01$ Ωcm). Electrodes to the nanotubes were defined using optical lithography in a bilayer resist for simple lift-off (120 nm LOR1A/1.3 μm Shipley S1813 both available from Microchem Corp.) as shown in the SEM image in Fig. 5.5b, followed by electron-beam evaporation of a 75 nm titanium film and lift-off in PG Remover. The overall electrodes are shown in the optical image in Fig. 5.5c and d.

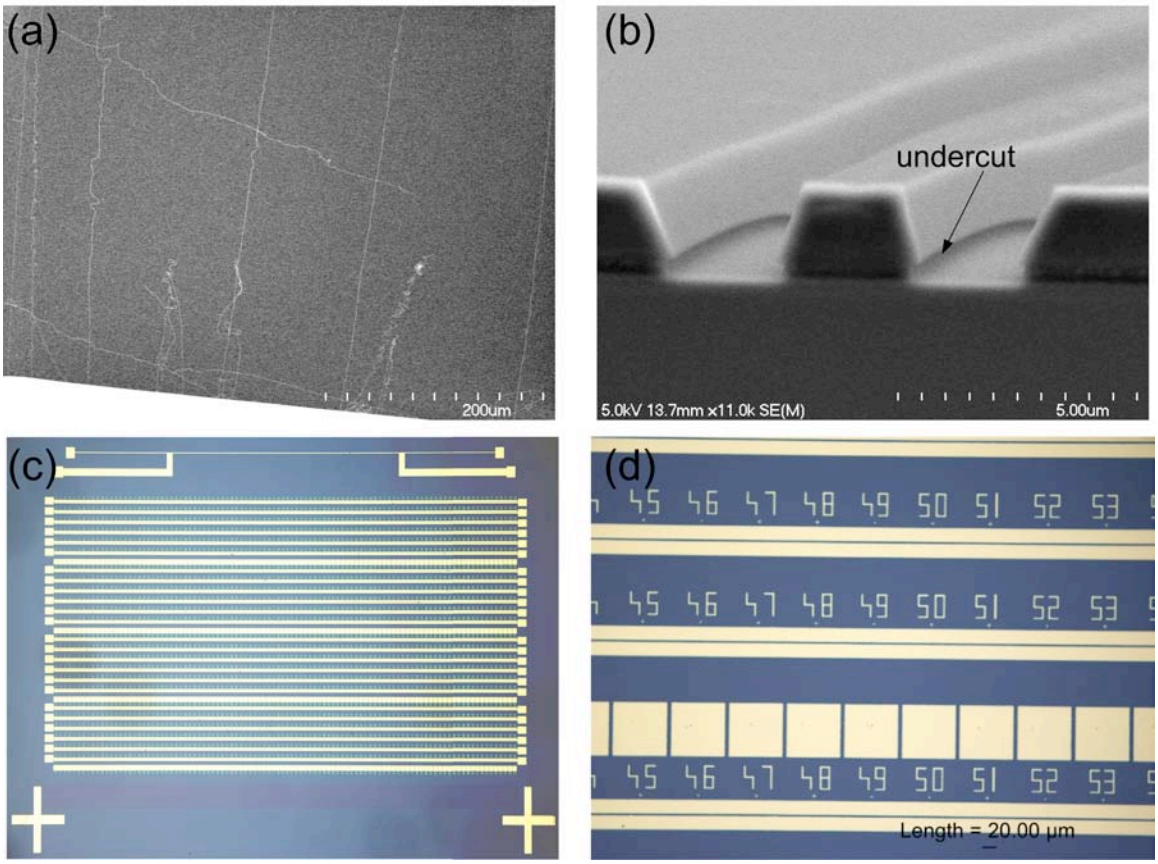

Figure 5.5: Creating carbon nanotube devices. (a) SEM image of CVD grown carbon nanotubes on chip with density of around 1nanotube/100 μm. (b) Side view of bilayer photoresist showing undercut for metal liftoff. (c) Optical image of electrodes on chip with zoomed in view in (d).

5.3.3 CNT mapping

Scanning electron microscopy and atomic force microscopy are used to locate the nanotubes relative to alignment marks and electrodes on the substrate as shown in Fig. 5.6a and to measure their diameter (only tubes with a diameter less than 2 nm were chosen). Afterwards, another lithography step is used to cover a selected nanotube followed by an oxygen plasma etch (Technics Series 800 RIE machine, 50 W RF power, 250 mTorr oxygen for 10 s) to remove all other nanotubes. This etching step is crucial because it guarantees that only a single tube bridges the electrodes and that neighboring electrodes are electrically isolated as shown in Fig. 5.6b.

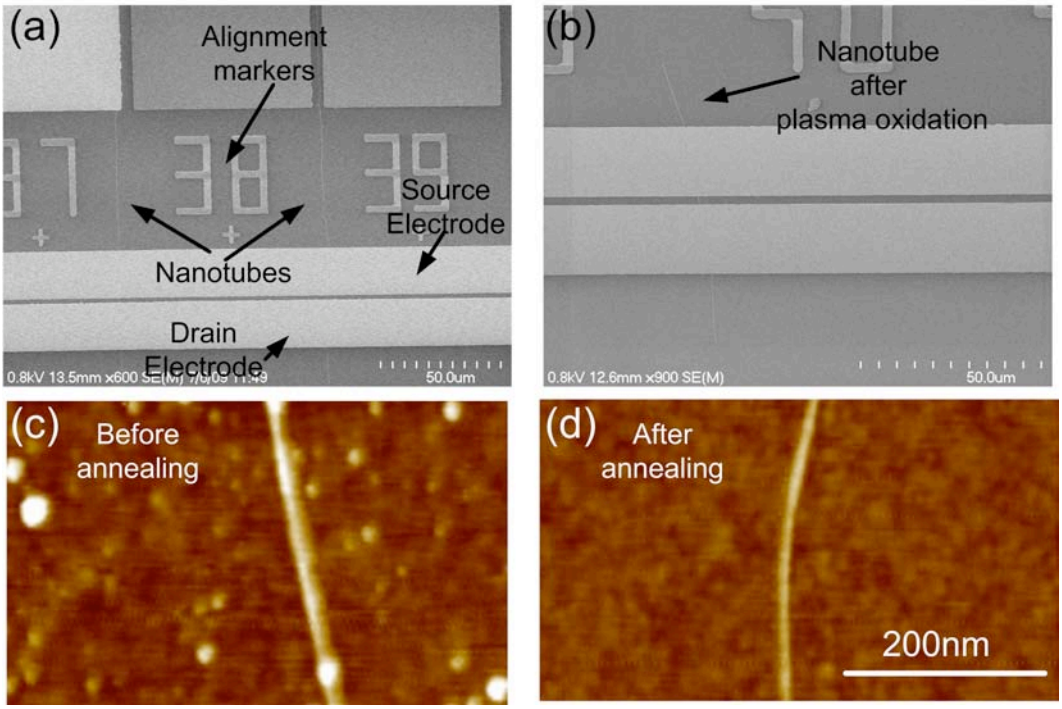

Figure 5.6: (a) SEM image of carbon nanotubes on substrate with titanium electrodes and alignment markers. (b) Electrically isolated remaining nanotube after oxygen plasma etch. (c) AFM image of nanotube after fabrication with resist residue. (d) cleaned nanotube after hydrogen/argon anneal.

5.3.4 Surface cleaning

After the fabrication steps above, the surface of the chips is covered by a thin film of residual resist as shown in the AFM image in Fig 5.6c. Due to the strong van der Waals interaction with the hydrophobic surface of the nanotube, the resist molecules cannot be easily removed by lift-off. A simple method to clean the surface is used similar to the one used to obtain clean graphene [160]. The chip is annealed in hydrogen/argon (premixed at 1:10 ratio) for 2 hours at 400 degrees. The chip is now clean and free of residual resist as shown in the AFM image after annealing in Fig. 5.6d.

5.3.5 Aqueous measurement

After wire-bonding the chips to a 44 pin J-leaded chip carriers (Chelsea Technology), the wirebonds were electrically and mechanically insulated by standard epoxy (EPO-TEK GE120 and EPO-TEK 302-3M for damming and filling). A small glass tube was fixed on

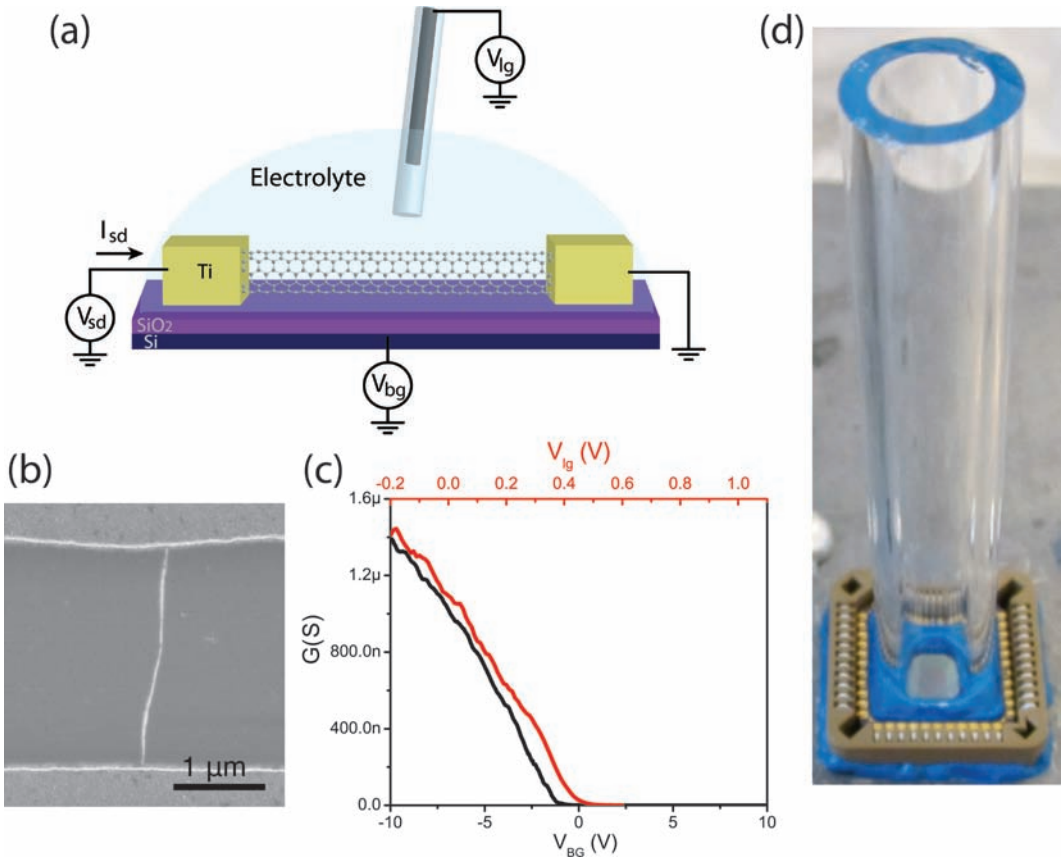

Figure 5.7: (a) Measurement setup for liquid gated carbon nanotube. (b) SEM of carbon nanotube device with a channel length of 2.5 μm. (c) Current as a function of back gate (black) and liquid gate (red). (d) Implementation of setup with small glass tube over device after wire-bonding and encapsulation.

top of the epoxy to create a 3 ml cavity for the aqueous experiments as shown in Fig. 5.7d.

Electrochemical experiments have a standard potentiostat configuration. Here, the potential of the solution is set through a platinum electrode which is controlled by a feedback system so that the Ag/AgCl reference electrode measures the potential that is applied to the amplifier. The advantage of this setup is that there is no current flowing into the reference electrode so the potential of the solution as measured by the reference electrode is very well controlled. Also, the platinum electrode is able to supply large currents while any changes at the interface do not have any affect.

A more common liquid gate configuration is using either a platinum or Ag/AgCl as a pseudo reference electrode. Minot et al. [93] showed that using an Ag/AgCl reference electrode, which is separated from the analyte by a porous glass frit can be used to gate

the carbon nanotubes. The advantage of this configuration is that changes in the interface of the platinum electrode with the analyte by binding of biomolecules can be avoided. Therefore the sensor response only from the nanotube can be measured which is important for biosensor applications, which only have a one-time event such as binding of biomolecules to the sidewall. Alternatively, a platinum electrode can be used for gating of the nanotube, which leads to the same gating efficiency except with a 330 mV offset (the same current appears at a gate voltage 330 mV higher when using the platinum electrode than the Ag/AgCl electrode). This is advantageous in harsh electrochemical environments and can be used for biosensor measurements that do not have a one-time event. Here, the measurement is done at equilibrium after the biomolecules have been introduced into the analyte and the response is not due to adsorption of biomolecules to the platinum pseudo-reference electrode. Another advantage of the platinum electrode is that it can be cleaned easily after the experiment by grinding away the outer layer with fine sandpaper and then rinsing it with deionized water.

The carbon nanotube field effect transistor in aqueous 1X PBS buffer solution is shown in Fig. 5.7. Here an Ag/AgCl electrode is used to gate the device, which is made from a semiconducting carbon nanotube. The gating is compared to the back gate through the 300 nm oxide in air when a 100 mV source to drain bias is applied. Because of the much larger capacitance in the electrolye (C_{lg}/C_{BG})$\approx$10), the device can be turned off at much smaller voltages with the electrolyte gate than with the back gate. Using titanium electrodes for source and drain contacts is advantageous because the thin oxide on the titanium significantly reduces the faradaic currents and prohibits leakage through the solution during measurement. The leakage current through the electrolyte is around 100 pA, several orders of magnitude smaller than the device current. As an alternative, resist such as poly(methyl methacrylate) or SU-8 (available from Microchem Corp.) can be patterned to open windows only over the carbon nanotube. Because the electrodes are not in contact with the solution, there will be no leakage current. However, the simple titanium electrodes reduce the processing steps significantly so for all the experiments described here, this configuration has

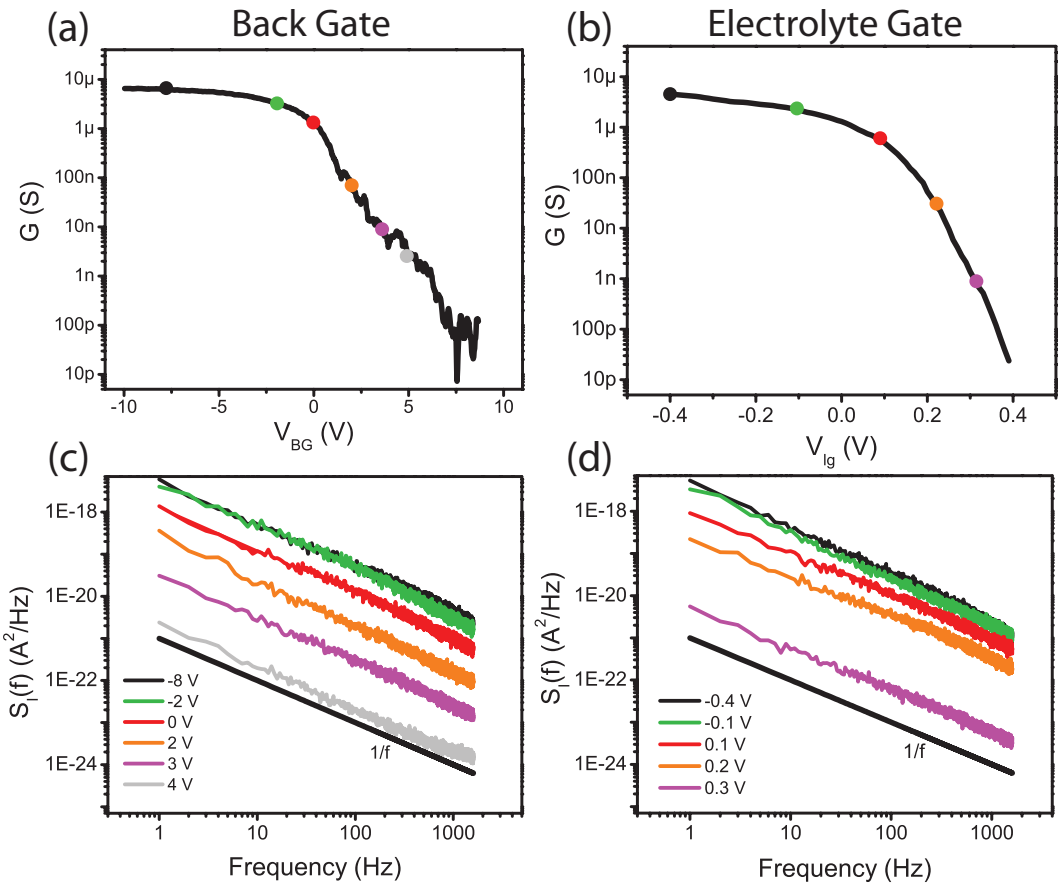

Figure 5.8: Gate sweep with back gate (a) and electrolyte gate (b) and corresponding flicker noise measurement (c) and (d).

been used.

5.4 Noise measurements

An essential attribute of any biosensor is their inherent noise and background limitations. Since carbon nanotubes have nanoscale diameters and all channel atoms are at the surface, they have shown tremendous sensitivities to biomolecules. The same characteristic also makes them very vulnerable to charge fluctuations in their environment. Several reports have described their low frequency noise characteristics with a typical flicker noise or 1/f noise spectrum. In this section, a comparison is made between the back gated transistor and electrolyte gated transistor in terms of noise characteristics.

The noise was measured [161] with a transimpedance current amplifier (Stanford

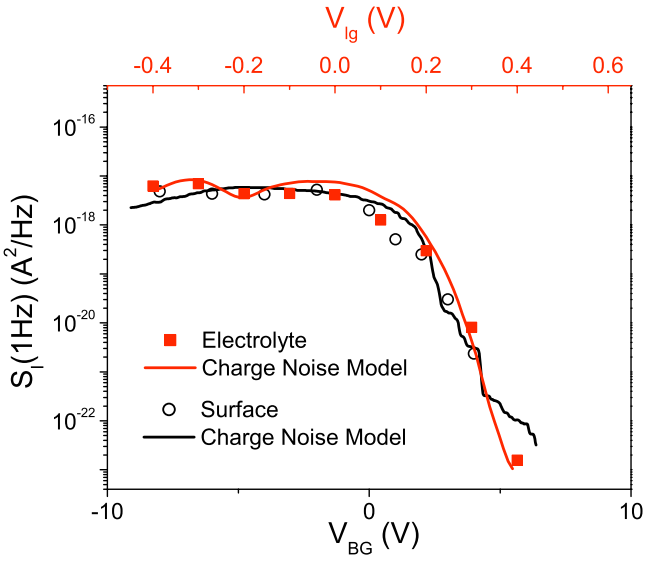

Figure 5.9: Current noise spectral density at 1 Hz showing fit using charge-noise model.

Research SR570) to set a small 20 mV source and drain bias (less than the thermal voltage) and convert the current to a voltage. The spectrum at the output is taken with a Dynamic Signal Analyzer (Agilent 35670A). The gate bias in both cases is applied with a voltage source (Agilent 4155C Semicondutor Parameter Analyzer). Fig. 5.8 shows the noise power spectral density of the carbon nanotube current as a function of bias both for the back gate configuration and the electrolyte gate (with Ag/AgCl pseudo-reference electrode in 1X PBS buffer). Both experiments show that the noise has a flicker noise spectrum and the noise amplitude is very similar. Overall, the flicker noise was measured at several different bias points both for the back gated and electrolyte gated device.

There are two different models for the cause of flicker noise in carbon nanotubes. The first is the empirical Hooge model [162], which suggests that noise is caused by independent scattering events of charge carriers and therefore scales inversely with the number of charge carriers in the nanotube. Recent experiments compared the Hooge model to data from ambipolar devices and showed that the Hooge model does not fit the data [163]. A much better fit was found using the charge noise model [164]. This model is attributed to random fluctuations of charge in the environment of the channel.

The flicker noise obtained in Fig. 5.8 better fit to the charge-noise model with the

spectrum proportional to

$$S_I \propto \frac{1}{C_g^2}(\frac{dI}{dV_g})^2 \tag{5.12}$$

The noise spectrum at 1 Hz has been plotted in Fig. 5.9 and fitted to the above equation. The only difference between the back gate and electrolyte gate are the gate capacitance. This result demonstrates that the liquid itself does not contribute significant noise, which is important for biosensor applications in aqueous environments. The other important result is that the majority of the noise is due to charges very close to the nanotube channel because otherwise the counterion screening (Debye length is about 0.7 nm in 1X PBS) would reduce the effect of 1/f noise in the electrolytic gated device compared to the back gate device.

5.5 Subthreshold slope

The electronic properties of carbon nanotubes are mostly controlled by the nanotube/metal contacts because of Schottky barriers at the interface. Even though Ohmic contacts have been demonstrated using palladium as a metal contact [121], the variability in the contact resistance is still large from device to device. Experiments with Schottky barrier devices have shown limited ability to turn off as a function of gate voltage [165]. However, the turn off characteristics can be improved by reducing the gate oxide thickness and also reducing the barrier at the metal/nanotube interface [166] so that the subthreshold characteristics approach the bulk switching limit in field-effect transistors [167, 168].

Assuming that the subthreshold slope is given by a thermionic emission over a barrier, the hole carrier concentration can be written in terms of the density of states and the Fermi dirac distribution,

$$p(E) = g_v(E)(1 - f(E)) \sim g_v(E)e^{\frac{E_v - E_F}{k_B T}} \tag{5.13}$$

The change in energy of the valence band can be approximated by an effective gate

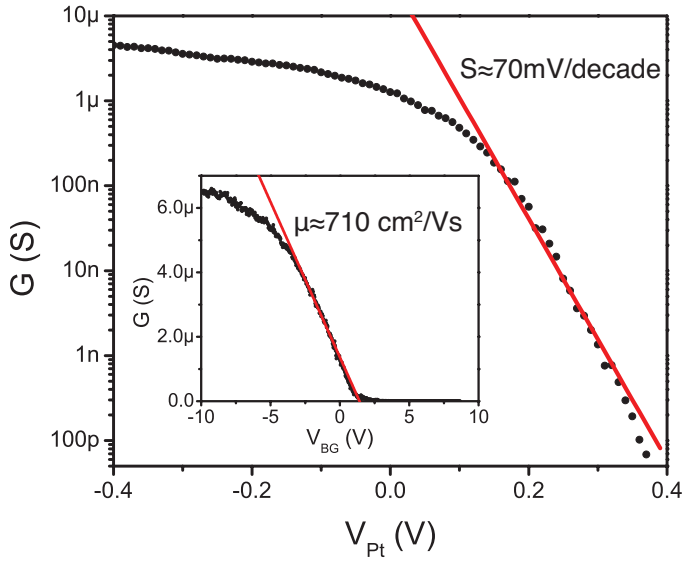

Figure 5.10: Gate sweep showing extraction of subthreshold slope of 70 mV/decade. The inset shows fit to linear region to extract mobility from Eqn. 5.16.

coupling α with $E_v = e\alpha V_g$. The conductance can then be written as

$$G = Lpe\mu = Leg_v(E)\mu e^{\frac{e(\alpha V_g - E_F)}{k_B T}}. \tag{5.14}$$

The subthreshold slope is given by

$$S = (dlog(G)/dV_g)^{-1} \approx 1/(logee\alpha e/k_B T) = ln10\frac{k_B T}{\alpha e} \tag{5.15}$$

Ideally, $\alpha = 1$ and the ideal thermal limit of the subthreshold slope is 60 mV/decade. From Fig. 5.10, the subthreshold slope for the electrolytically gated device is about 70 mV/decade, very close to the ideal limit. Other studies on carbon nanotube in aqueous electrolytes have observed similar values of 80 mV/decade [169] and 75mV/decade [163].

5.6 Mobility and Transconductance

From the Drude model, the conductance for a nanotube device can be written as $G = L\sigma = Lne\mu$. In the linear region, the gate can directly modulate the carrier density so that $n = C_g V/e$. Taking the derivative with respect to the gate voltage and rearranging for μ, the mobility can be expressed as

$$\mu = \frac{L}{C_g}\frac{dG}{dV_g}. \tag{5.16}$$

The extracted mobilities for this device is about 720 cm^2/Vs, which is considerably smaller than the highest reported limit of 79000 cm^2/Vs [170]. This value was extracted from the subthreshold region when the device started to turn off and the linear region mobility was around 10000. The transconductance for this device can be found by differentiating the current with respect to gate voltage as $gm = dI/dV_g$

In the linear region (with V_{ds}=100mV), which is important for sensor applications, this value is around 4.5 μS. This normalized value of 3.2 μS/nm is slightly lower than previously reported [169]. This is both because of the long channel (2.5 μm) and also because the contacts are far from ideal. By changing the metal contacts from titanium to palladium, both the mobility and the transconductance could be improved. This would however lead to more processing steps as the leakage current through the metal becomes comparable to the device current and another passivation layer (oxide or resist) has to be patterned over the electrodes.

5.7 Ensemble biosensing experiments

The carbon nanotube field-effect transistor described above is the ideal candidate for label-free detection. The device can operate in aqueous environment that is compatible with biomolecules, exhibits long-term stability and is extremely sensitive to environmental changes and local charge density. Since biomolecules usually have local charges such as the negative phosphate backbone in DNA molecules and side chain bases in proteins, they should lead to a current change in the nanotube upon adsorption to the nanotube sidewall. Experiments have been conducted either with specific adsorption using coated nanotubes [171] or non-specific adsorption with pristine nanotubes [92, 93].

As an example of ensemble sensing, bovine serum albumin (BSA) has been used. After the annealing step, the pristine carbon nanotube in the AFM image in Fig. 5.11a is immersed in 50 nM BSA in 1X PBS solution for 1h. Afterwards, the chip is rinsed

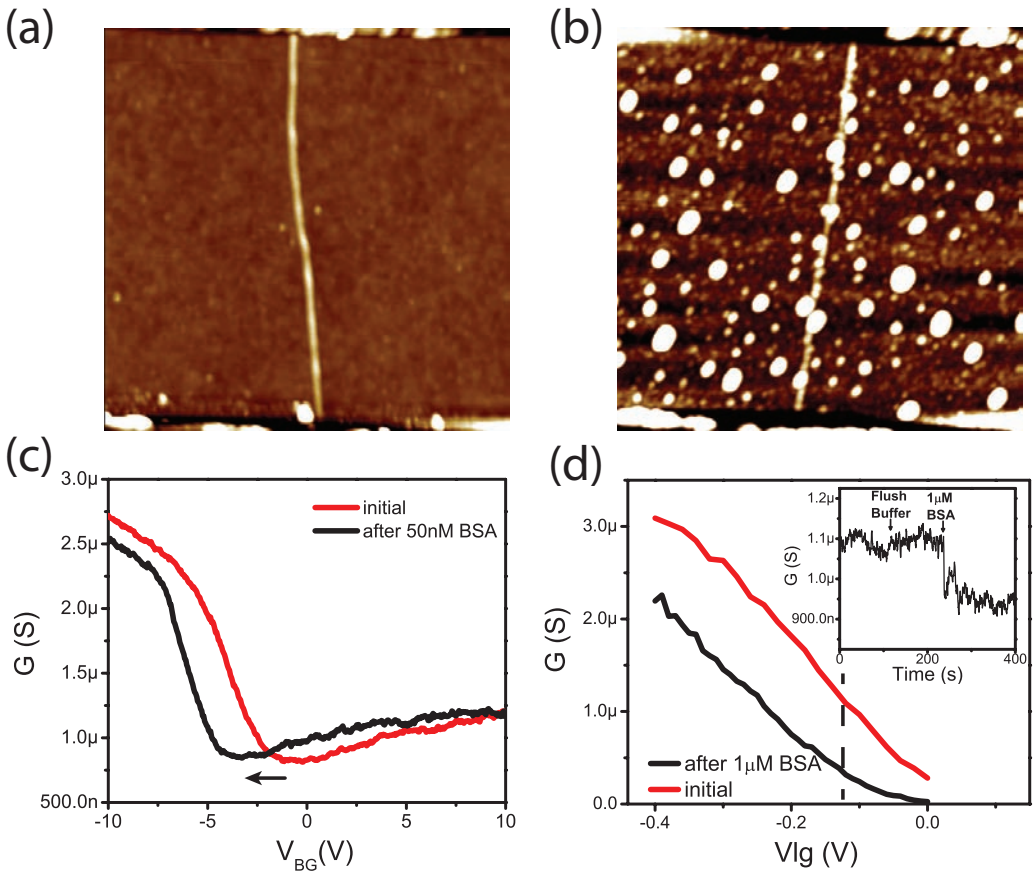

Figure 5.11: AFM image of pristine device (a) and device after exposure to 50 nM BSA for 1 hour (b). Back gate sweep (c) and electrolyte gate sweep (d) before and after exposure to BSA. The inset in (d) shows real time detection of BSA.

thoroughly with deionized water and dried in a stream of nitrogen. As shown in the AFM image afterwards (Fig. 5.11b), the adsorption of proteins tends to be preferentially to the carbon nanotube. A simple experiment is to measure the device before and after this exposure using the back gate. This has been done in Fig. 5.11c. The BSA protein causes a shift in the threshold voltage (this device is a metallic device with a small bandgap that does not turn off so the threshold voltage is defined as the minimum in the conductance) to a negative value with a threshold shift of around -3 V. This result would indicate that the biomolecule is positively charged and donates electron.

Initially this might be a surprise because the isoelectric point (pI) of BSA is about 4.7, indicating that the total charge on the molecule is negative at neutral pH. In order to verify that there have not been any artifacts due to the drying of the chip, the experiment

was also done under aqueous buffer. Fig. 5.11d demonstrates that the Ag/AgCl electrolyte gate response is shifted by around -120 mV when exposed to 1 μM BSA buffer. This can also be seen in the real time conductance plot in the inset of Fig. 5.11d. Here, the device was held under constant bias and the conductance was recorded using a lock-in amplifier. The device shows no response when only buffer is used but a clear drop when the device is immersed in BSA solution. This result is now consistent with the back gate sweep indicating that there is a threshold shift to the negative direction.

Several other groups have also reported negative shifts using BSA [93, 172] and Streptavidin (with pI$\sim$5) [92, 173]. An explanation was given by [92] who noted that these proteins contain several arginine and lysine residues with amine groups. These amine groups actually donate electrons to the nanotube similar to studies using ammonia in solution. Therefore the negative threshold voltage shift due to the BSA molecules can be explained by amine groups in close proximity to the nanotube channel. While the above biosensing experiment has demonstrated the sensitivity of carbon nanotubes, the current version does not have enough sensitivity to detect single molecules. The specificity is low even when coated with surfactants to reduce nonspecific adsorption and there is no localization of the sensitivity. These issues will be addressed in the next Chapter.

Chapter 6

A label-free single-molecule field-effect sensor

Single-molecule measurements of biomolecules can provide information about molecular interactions and kinetics that are hidden in ensemble measurements. However, techniques with improved sensitivity and time-resolution are required to explore biomolecular systems with fast dynamics. In this chapter, the detection of DNA hybridization at the single-molecule level using a carbon nanotube field-effect transistor is reported [174]. By covalently attaching a single-stranded probe DNA sequence to a point defect in a carbon nanotube, two-level fluctuations in the conductance of the nanotube in the presence of a complementary DNA target can be measured. The kinetics of the system are studied as a function of temperature, allowing the measurement of rate constants, melting curves and activation energies for different sequences and target concentrations. The kinetics show non-Arrhenius behaviour, in agreement with DNA hybridization experiments using fluorescence correlation spectroscopy. This technique is label-free and could be used to probe single-molecule dynamics at microsecond timescales.

6.1 Introduction

Studies at the single molecule level have revealed intramolecular dynamics and conformational changes in many biomolecular systems as described in Chapter 2. The intramolecular chain diffusion of nucleic acids, particularly the hairpin configuration, has been extensively studied by optical techniques such as fluorescence correlation spectroscopy (FCS) [43–45]. In these studies, labels are attached to the DNA hairpin and the opening and closing rates of a small number of molecules can be monitored at sub-microsecond time-scales. One of the disadvantages of FCS, however, is that observation time is limited to the diffusion time of molecules through the observation volume [23]. Single-molecule fluorescence resonance energy transfer (smFRET) has also been used to study conformational changes in biomolecules [38] but provides only tens of millisecond time-scales for kinetic studies. Label-free technologies for biomolecular detection include nanowires [90], microcavities [175], mechanical cantilevers [176], optical waveguides [177] and optical tweezers [178], but none have combined high enough sensitivity for label-free detection with the high temporal resolution necessary to monitor the kinetics of biomolecular processes to microsecond time-scales.

One-dimensional (1D) conductors such as single-walled carbon nanotubes (SWCNTs) act as high-gain field-effect sensors whose conductance varies strongly with local charge density. As described in Chapter 5, initial experiments with both specific adsorption with coated nanotubes [171] and non-specific adsorption with pristine nanotubes [171] have not demonstrated sufficient sensitivity to detect single biomolecules with the highest reported sensitivity for DNA detection of 14 pM [95]. Other studies have employed carbon nanotubes as electrodes. Small gaps are etched into the tubes, bridged by molecular junctions, the conductance of which is monitored for sensing. These devices are able to distinguish between fully complementary bridging DNA duplexes and ones with a single mismatch but DNA hybridization kinetics could not be measured [99].

Recently it has been shown that single point defects can be electrochemically created in nanotubes in a controllable manner and can be used to covalently bind biomolecules at the scattering site [100]. The resulting device has been demonstrated to exhibit sensitivity

to the binding of a single molecule (with a conductance change of more than 100 nS for binding of a reactive carbodiimide), due to Coulomb interaction between the molecule and the defect which modulates scattering in the 1D channel [101]. Compared with molecular-bridge devices, these devices can be prepared with much higher yield due to the real-time monitoring of conductance during defect generation. In this chapter, the defect-dominated conductance in nanotubes is used to produce the first measurements of DNA hybridization kinetics in which sufficiently high signal-to-noise ratio (SNR) and bandwidth have been achieved to measure single-molecule kinetics and thermodynamics through a label-free field-effect-based approach.

6.2 Defects in carbon nanotubes

Single-walled carbon nanotubes are often regarded as clean, defect-free, rolled up cylinders of graphene. Many experiments have provided evidence of this claim through low temperature studies of interesting quantum mechanical effects such as Mott insulators [179], ballistic transport [121], long mean-free paths [123] and Kondo effects [180] and also scanning tunneling microscopy on pristine nanotubes [64]. However, defects in carbon nanotubes such as lattice vacancies, structural defects, deformations and nanotube junctions have been theoretically predicted [181–183] and several experiments have shown the effect of a defect on electronic transport in CVD grown nanotubes [184, 185], solution processed devices from dielectrophoresis [186] and carbon nanotube intramolecular junctions [187, 188]. In order to utilize a defect in a sensor application, a controlled method for defect engineering is necessary.

These methods can roughly be divided into electrical, mechanical, irradiation and electrochemical based defect creation and they have mostly been used for low temperature electronic transport measurements such as coulomb blockade and quantum dots. Electrical oxidation of a carbon nanotube has been demonstrated by applying a voltage pulse between an AFM [189] or STM [190] tip and the carbon nanotube sidewall. While the STM provides atomic resolution, the experimental setup is difficult and requires the nanotube to be placed

on top of a conducting surface. The AFM tip has been used to define a quantum dot by locally nicking a carbon nanotube at two different locations 50 nm apart. An AFM has also been used to mechanically deform a carbon nanotube [191] to create a barrier in electronic transport or to cut a nanotube and move the two ends together [192]. This has been used to experimentally verify electron tunneling into a nanotube as described by Luttinger liquid theory, which will be further discussed in Section 6.3.3. Irradiation of carbon nanotubes has also been used for defect generation by irradiation with argon ions [193] and electron irradiation [194]. None of the methods mentioned above have a very good control over the functional group that appears at the defect. This is crucial for biosensors since the defect has to be chemical reactive for specificity.

6.3 Electrochemical method to create point-defect

As an alternative, point functionalization of carbon nanotubes can be achieved by a conductance controlled electrochemical method similar to the one previously reported: Goldsmith *et al.* [100, 195] reported that electrochemical oxidation of carbon nanotubes can break the sp^2 carbon lattice and lead to sp^3 carbon, which will eventually make the nanotube insulating. Similar experiments have been previously done in bulk where strong acids lead to intercalation on the surface of highly oriented pyrolytic graphite (HOPG) [196].

The fabrication of the nanotube devices has been described in Chapter 5. After wire-bonding and epoxy encapsulation, a platinum counter electrode was used in a pseudo reference configuration to control the liquid potential during oxidation with a small 30 mV bias applied between source and drain electrodes. For the electrochemical oxidation, sulfuric acid (1M H_2SO_4 in deionized water) has been used. For small, applied potentials to the platinum electrode (-0.7 V $< V_{Pt} <$ 0.7 V), the sulfuric acid electrolyte can be used to gate the device, very similar to other electrolytes such as NaCl buffers. However, if an oxidation potential, slightly greater than the oxidation threshold (between -0.9 and -1V), is applied through the platinum electrode, the conductance of the device decreases as the nanotube is oxidized.

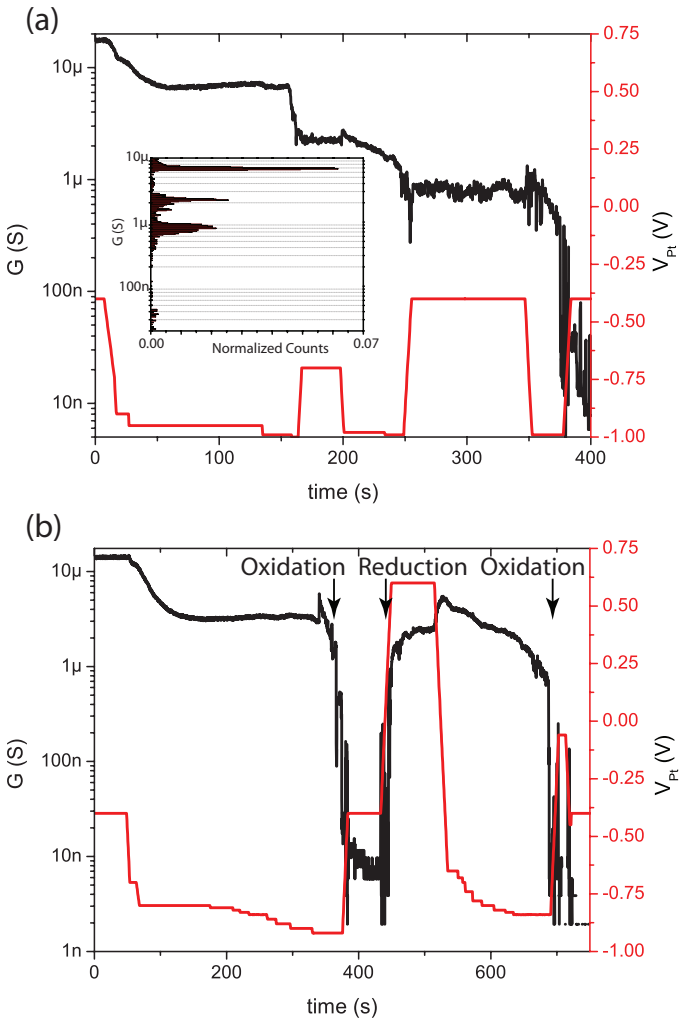

Figure 6.1: Conductance-controlled electrochemical oxidation of a nanotube in 1M sulfuric acid. (a) Typical oxidation with conductance decreasing to almost zero. Conductance drops in discrete steps as shown in the inset. (b) After oxidation, conductance can be recovered by inverting the solution potential (Reduction) and then device can be oxidized again.

A typical conductance controlled electrochemical oxidation is shown in Fig. 6.1a. After a slowly decreasing period, which has been attributed to the buildup of positively charged scatterers in the channel [195], the conductance starts to decrease in discrete steps. The stochastic nature of this process can be seen since sudden drops are often followed by reversals of similar amplitude. The histogram of the conductance shows several discrete conductance levels before the conductance drops to zero and the device is insulating. By reversing the solution potential to positive values, the initial conductance can be partially restored as shown in the oxidation in Fig. 6.1b.

Theoretical calculations on the effects of oxygen functional groups on the conductance of carbon nanotubes [197] show that single oxygen atoms do not account for the large change in conductance. However, a small cluster of oxygen atoms can lead to conductance changes in metallic carbon nanotubes (zigzag CNT) around one order of magnitude, which is similar to the one observed experimentally. This is reasonable, because once a carbon bond is broken, the atoms around it will be more chemically reactive so that the closest bond could also be broken. The destruction of the hexagonal lattice by sp^3 hyrbridization with sulfuric acid intercalation will lead to a transport barrier, which reduces the conductance. It was proposed [100] that after reduction of the insulating device, the resulting sp^2 lattice is again highly conducting but slightly lower than the initial value because the functional group is an ether.

Devices were electrochemically oxidized by two different protocols. When the oxidation is terminated at an approximately 90% reduction in the conduction level, 88% (23 out of 26) of the devices remained conductive out of which 19% yield functional single molecule devices for measuring DNA hybridization kinetics. At a greater than 99% reduction in the conductance level [100], the percentage of conductive devices decreased to 18% (7 out of 38) out of which 28% yield functional single molecule devices. The low yield in this final step is attributed to a number of factors including the possibility of generating unreactive C-O and C=O defects [198], multiple reactive defects and over-oxidation that yields insulating devices. As shown in the following section, a single drop to about 10% of the original value in conductance is sufficient to guarantee that the carbon nanotube devices has a single point defect. Futher oxidation would only destroy the nanotube lattice futher and increase resistance. After the drop in device conductance, the oxidation potential is reduced and the device is immersed in 6.5 mM $KMnO_4$ in order to create a carboxyl functional group on the freshly created defect. Overall, seven functional devices (out of 64) were fabricated, which are characterized by the two-level conductance fluctuations described below when functionalized with probe DNA in the presence of complementary target.

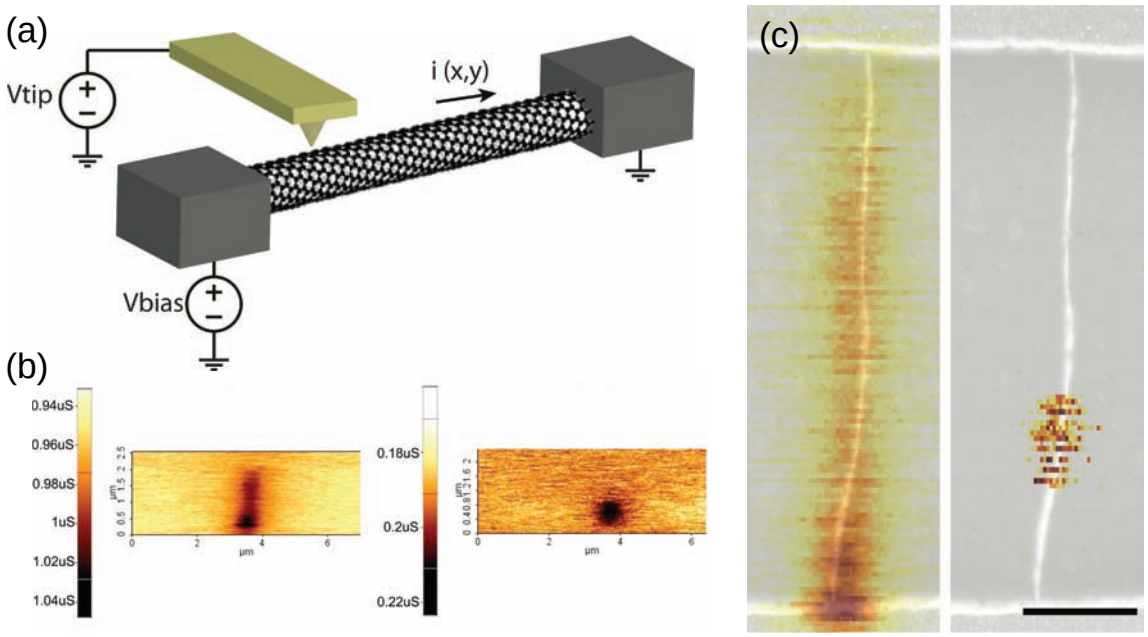

Figure 6.2: Scanning gate microscopy of carbon nanotube. (a) In SGM, the tip of an AFM is used to bias the device and the conductance is recorded as a position of the tip. (b) Raw data of SGM with a pristine device on the left and an oxidized device on the right. The total current is decreased by over a factor of 5. (c) Combined topography/SGM image of a semiconducting nanotube. Scale bar is 500 nm. In the overlaid SGM image, the darker yellow colour corresponds to lower current at a fixed bias voltage of 100 mV.Before oxidation (left image), the current is enhanced near the source where the Schottky barrier forms. After oxidation (right image), the well localized region of highest sensitivity shows up in the middle of the tube, indicating the defect site.

6.3.1 Scanning gate microscopy

Since only a few carbon atoms are altered during the electrochemical oxidation, common spectroscopy techniques such as Raman spectroscopy, atomic force microscopy and x-ray photoelectric spectroscopy are not sensitive enough and cannot be used to determine the position of the point defect and type of functional group. Instead, scanning gate microscopy (SGM) provides a way to determine the location of the point defect.

During normal gating of the device, either the back gate or electrolyte gate is used to induce or deplete carriers in the whole channel. This is sufficient to modulate the Fermi level and the Schottky barriers and increase or decrease the conductance of the device. In scanning gate microscopy, a local gate is applied to the cantilever of an AFM to a small region of the nanotube, while the conductance of the device is monitored as shown in

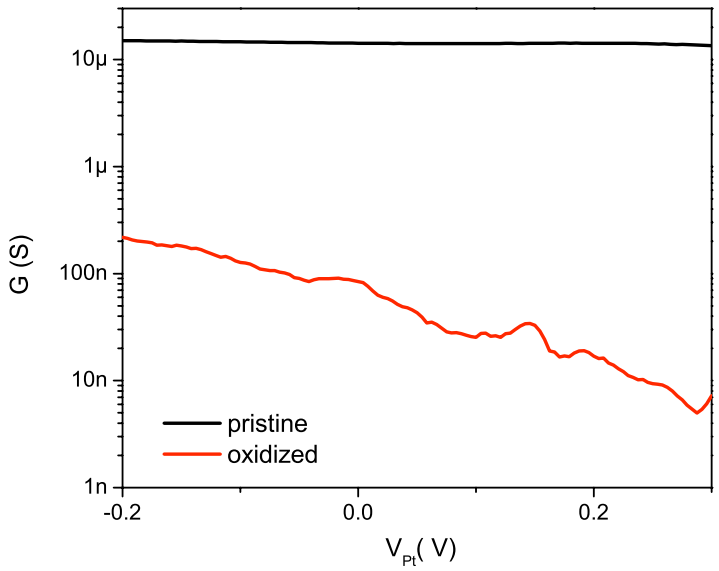

Figure 6.3: Conductance as a function of potential on the platinum electrode relative to the source-drain potential of the nanotube. Initially, the nanotube is metallic but shows a large gate response after oxidation.

Fig. 6.2a. Therefore this gate only acts very locally and the sensitivity of the device to the local gate can be spatially mapped out. Fig. 6.2c shows an SGM image of a typical semiconducting carbon nanotube device with a channel length of 2.5 μm. While the silicon back gate is left grounded, the chrome/gold tip of the AFM cantilever is biased at -2 V and scanned 30 nm above the surface. The pristine device is slightly p-type and the negative bias of the tip actually increases the conductance through local tip gating (the raw data is shown in Fig. 6.2b). Both the topography and SGM image are leveled without further processing. The conductance of the device increases by about 8% when the tip is over the Schottky barrier at the bottom contact.

The oxidized device has an overall conductance about 10 times smaller than the pristine device. Now the gate sensitivity is found at the location of the defect and the conductance can be modulated by about 22% over the defect. Both metallic and semiconducting devices have been used and they generally show a large gate dependence after oxidation. A representative current/voltage characteristic for a device in its pristine and

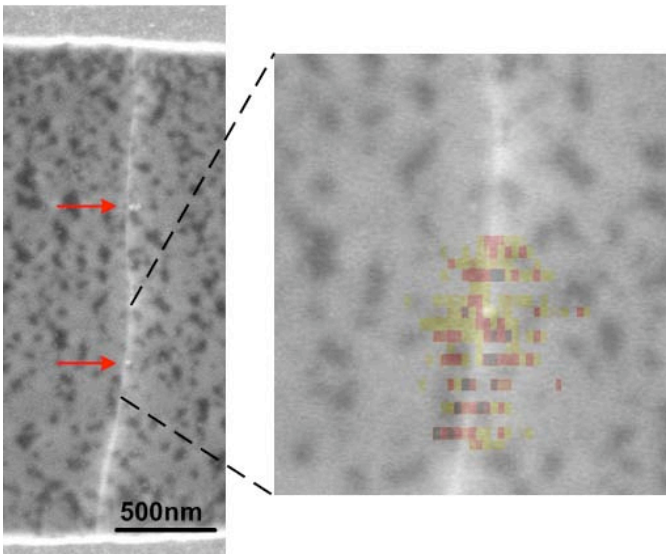

Figure 6.4: Point-functionalized nanotube after electrochemical oxidation after coupling with streptavidin labeled gold particle. There are two 40 nm gold particles in the SEM image. One of them is directly at the position of the highest sensitivity.

oxidized state is shown in Fig. 6.3.

6.3.2 Chemical reactivity

While the electrochemical oxidation introduces a defect in sulfuric acid, the short immersion in potassium permanganate for 45 s afterwards increases the yield of defects with a carboxylic acid functional group. In order to investigate the chemical reactivity of the freshly created defect, a gold-labeled streptavidin nanoparticle of 40 nm diameter was used. The streptavidin is a protein with many available amine groups so it can be coupled by a standard coupling reaction to the carboxylic acid defect. At the same time, the gold nanoparticle can be easily imaged by an SEM or AFM.

The coupling reaction is done in 0.05 M EDC (1-ethyl-3-[3-dimethylaminopropyl] carbodiimide hydrochloride) and 0.1M sulfo-NHS (N-hydroxylsuphosuccinimide) overnight. In order to reduce nonspecific adsorption, the surfactant Tween 20 is used (0.1 wt%). After overnight coupling, a gold nanoparticle can be found at approximately the same position where the gate sensitivity is as shown in the SEM image in Fig. 6.4. This ensures that the device is both chemically reactive and sensitive at the defect site. Another gold nanoparticle

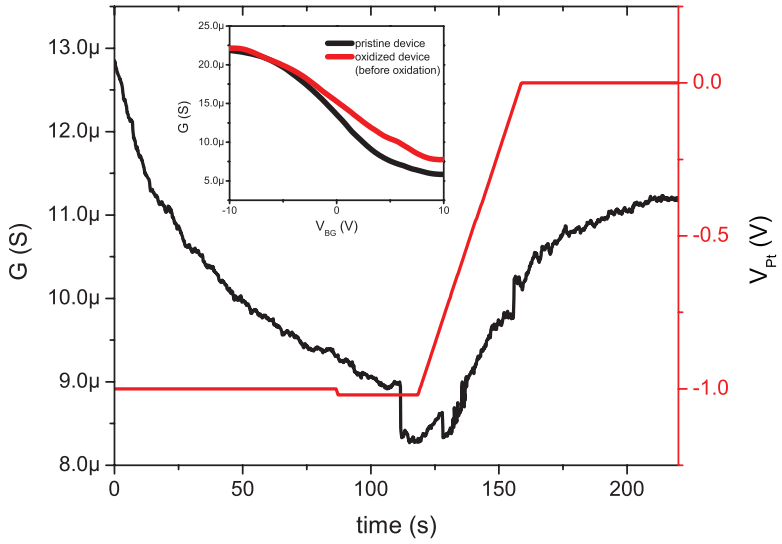

Figure 6.5: Oxidation of device used for low temperature measurement. A very small drop in the conductance can be seen at around 110 s. Initially, the pristine device and the functionalized device before oxidation show a very similar low bias behavior as a function of back gate as shown in the inset.

is found further up along the nanotube. This could be either a small minor defect or non-specific adsorption to the nanotube sidewall.

6.3.3 Low temperature measurement

In order to investigate the physical transport mechanism created by the electrochemical oxidation, temperature-dependent transport studies were done with a pristine and point defect device in a vacuum cryostat after the oxidation step. All the devices were made from the same carbon nanotube and showed almost identical low bias conductance as a function of gate bias before oxidation as shown in the inset of Fig. 6.5. For the device used for transport measurments after oxidation, the drop in conductance during the oxidation process is shown in Fig. 6.5. Here, only one small drop is observed after which the oxidation potential is reduced to avoid further oxidation and more than one dominant defect. The device is rinsed with deionized water and then immediately placed in the vacuum cryostat holder and pumped down to base pressure (around 10^{-6} mbar). At this pressure, the device was stable and temperature dependent measurements could be done.

The stability diagram in Fig. 6.6a for the pristine device shows the differential

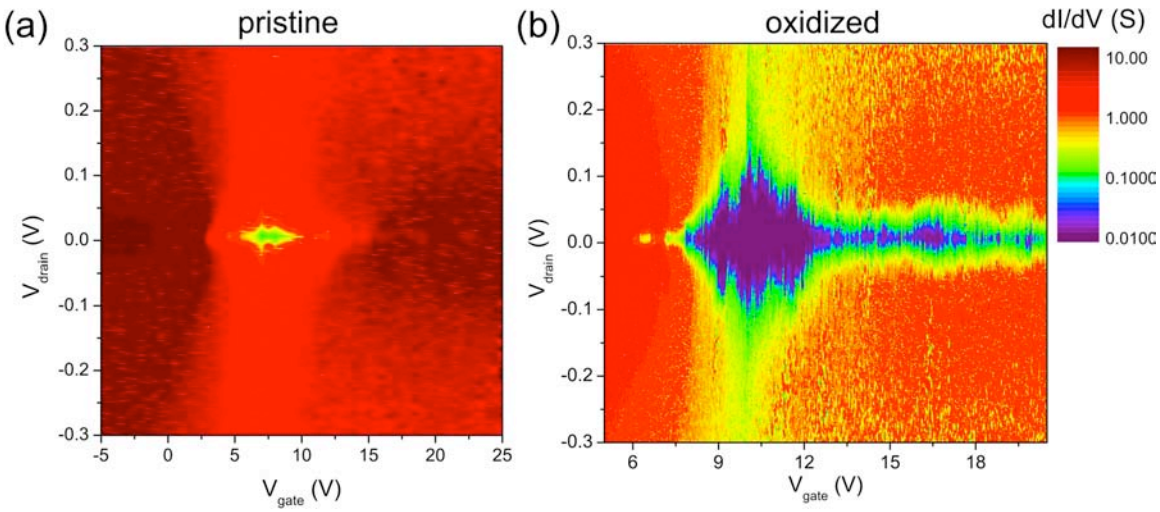

Figure 6.6: Differential conductance at low temperature (2.1 K). (a) Pristine device shows a very small bandgap that is less than 10 meV. (b) the oxidized device shows a barrier around 100 meV with a long low conductance tail at large back gate voltages.

conductance (dI/dV_{ds}) as a function of drain-to-source and gate voltage, which is taken at a temperature of 2.1 K. The diagram shows that the pristine device has a very small bandgap (or barrier) of less than 10 meV. This has often been observed in metallic carbon nanotube and is attributed to curvature effects [199] and also small barriers at the contacts especially for metallic carbon nanotubes with a small diameter [200]. This small bandgap is different from semiconducting carbon nanotubes that have a gap inversely proportional with their diameter of the order $E_g = 450$ meV/d [110]. If the 1.4 nm diameter nanotube used here was semiconducting, the bandgap would be around 320 meV, more than an order of magnitude larger than the measured bandgap. Besides the small bandgap, there are otherwise no particular features in the stability diagram. The scanning gate microscope image in Fig. 6.7a shows some sensitivity around the top contact area around 8%, which is attributed to a small barrier at the top contact.

The scanning gate microscopy image of the electrochemically-oxidized device is shown in Fig. 6.7b. The sensivity of the device is far away from the contacts and the modulation is around 15%. For this device, the stability diagram is shown in Fig. 6.6b. At low gate voltage ($V_g < 6$ V), where the carriers are holes, the differential conductance does not have any particular features and the values is similar to the pristine device. In

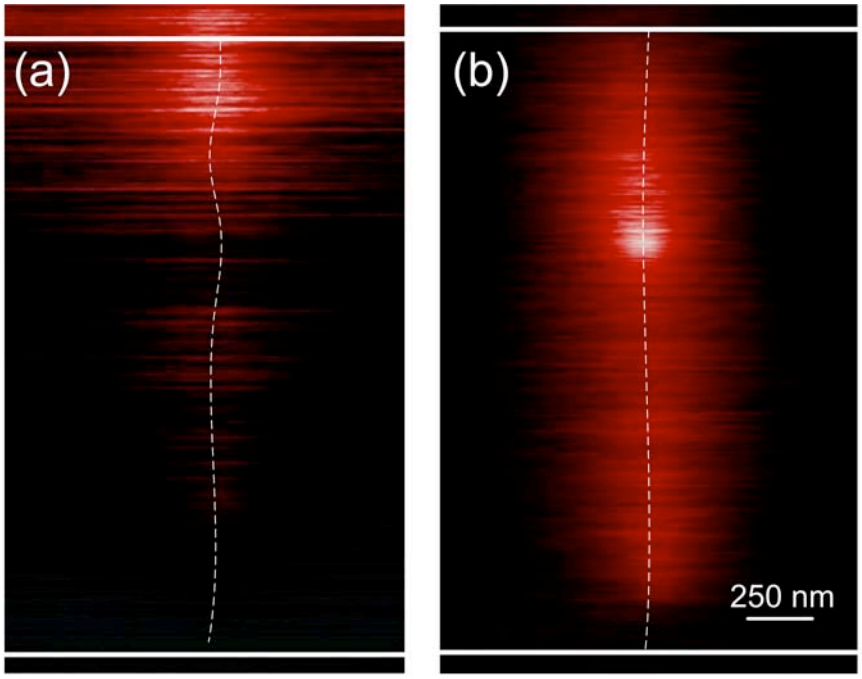

Figure 6.7: SGM of low temperature devices. (a) Pristine device showing small sensitivity at top contact due to Schottky barrier and (b) oxidized device with sensitivity over defect. Solid white lines indicate the contacts and dashed white lines the position of the carbon nanotube.

the middle of the gate range (6 V$\leq V_g \leq$13 V), there is a large region with low differential conductance. This region is much larger than in the pristine device at the same temperature and because of the strong localization in the scanning gate image, it is concluded that the barrier is the result of the defect. The stability diagram has another interesting region at the electron side. At large back gate potentials (V$_g \geq 13V$), the differential conductance has a long tail with low conductance. The height of this tail is approximately 13 meV.

Temperature dependent low bias transport measurements were done to investigate the barrier and the long tail in the stability diagram further as shown in Fig. 6.8 with extracted values in Fig. 6.9. The pristine device has temperature dependence that is typical for a diffusive device: As the temperature is lowered, the conductance at energies far away from the barrier (V$_g \leq -10$ V and V$_g \geq 10$ V)increases and then saturates to a finite value around 100°C. This is associated with phonons that freeze out and has been previously reported [123]. The minimum of the barrier has some temperature dependence. The barrier extracted from this low bias data is approximately 4.2 meV, similar to the

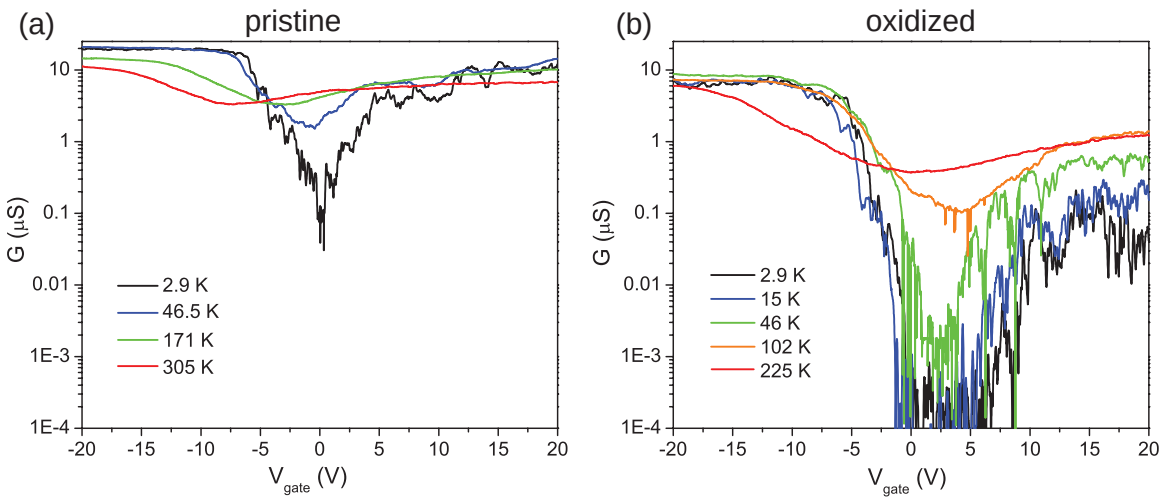

Figure 6.8: Low bias voltage sweep at different temperatures showing (a) pristine and (b) oxidized device.

differential conductance stability diagram.

The oxidized device has very similar temperature dependence for holes, which saturates at low temperatures. The conductance is only approximately 3 times lower in the oxidized device compared to the pristine device indicating the small perturbation for holes from the defect. At intermediate gate voltages (-10 V$\leq V_g \leq$10 V), however, there is a much larger barrier, which comes out to be 35 meV from the exponential fitting. Also, there is an interesting temperature dependence at the electron side that is proportional to T^{α} where α is 0.95. Because of hysteresis and spreading of the coulomb peaks, integrated conductance has been used, similar to previous analysis [191].

Due to their 1D structure, defects are expected to have a strong effect on electron transport in carbon nanotubes. Theoretical simulations have predicted quasibound states and strong backscattering in metallic carbon nanotubes with defects, which is not allowed in pristine metallic carbon nanotubes. This situation is similar to acceptor and donor states in bulk semiconductors [201]. The T^{α} temperature dependence has been previously observed in carbon nanotubes [191, 192, 202, 203]. The origin of this behavior is believed to be due to strong electron-electron interaction in a 1D conductor, which is described by a Luttinger liquid model. This model best describes tunneling into and out of a one dimensional conductor. This would imply that at positive gate voltages, the defect creates

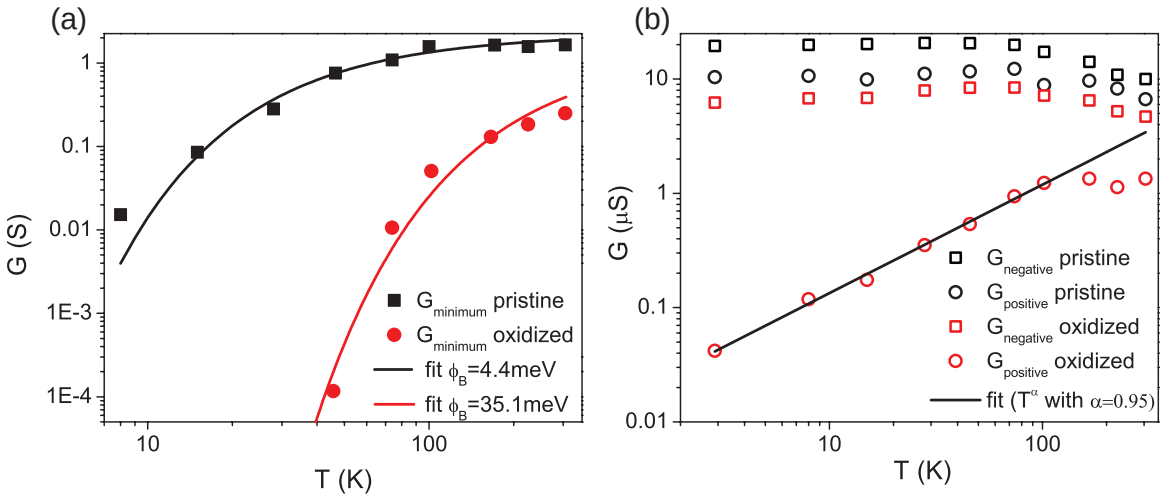

Figure 6.9: (a) Temperature dependence of minimum conductance point for both devices, which follows an exponential as expected from barrier activated transport. (b) Temperature dependence of conductance away from minimum point. The data over gate voltage has been averaged from -20 to -15 for the $G_{negative}$ values and 15 to 20 V for the $G_{positive}$ to reduce the variability and hysteresis effects.

a tunnel barrier for electrons which does not appear in the pristine device. From the T^{α} temperature dependence, the extracted α is also consistent with a Luttinger liquid model for end tunneling. This is a consequence of tunneling into a one-dimensional channel. Assuming that the quantum dot can be described by a sequential tunneling model, the conductance should have a temperature dependence of $G \approx T^{\alpha_{end}}$ [191, 204]. Theoretical predictions for a carbon nanotube have predicted a Luttinger interaction parameter of g$\sim$0.19-0.25 which leads to $\alpha_{end}=\frac{1}{4}(\frac{1}{g}-1)$ $\sim$0.75-1.06. From this model, the g value turns out to be roughly g=0.21 consistent with the theoretical predictions.

6.4 Electrical detection of DNA hybridization

The above investigation has shown that the defect can be modeled as a barrier in the carbon nanotube. In this section, these point-functionalized devices (as functionalized in Fig. 6.10b) are used to study the kinetics and thermodynamics of DNA hybridization for two different 10mer duplex DNAs with the experimental setup shown in Fig. 6.10a. Here, the experimental reservoir for the experiment is heated by a larger water reservoir that is controlled

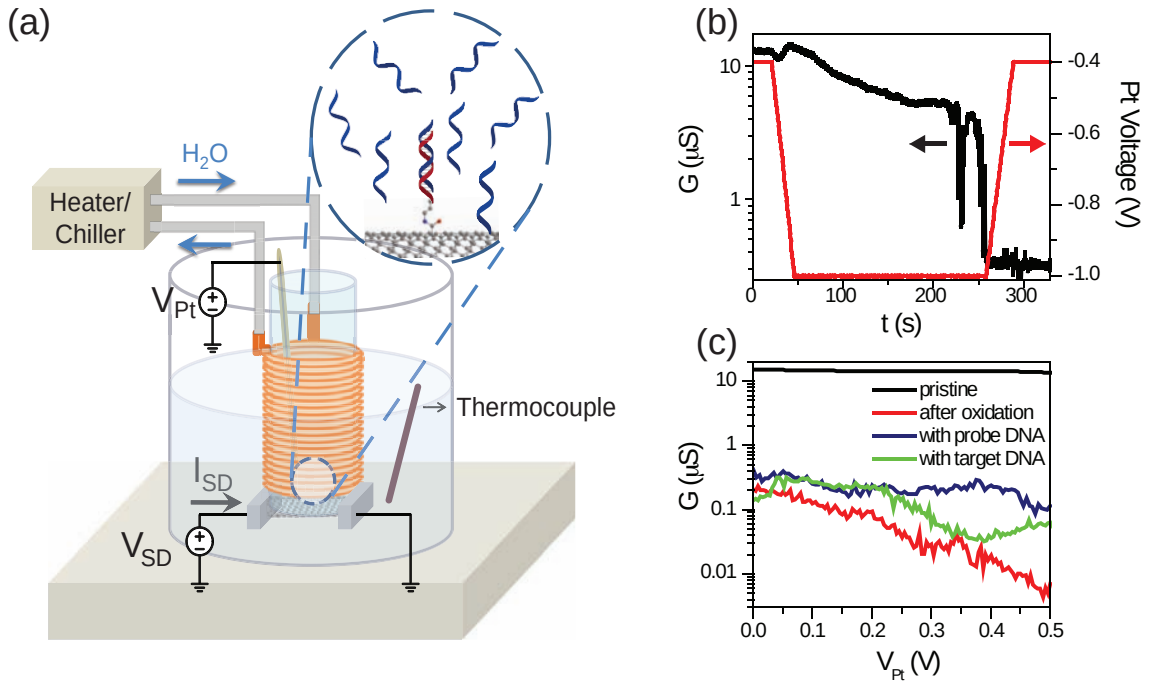

Figure 6.10: (a) Schematic of the nanotube device with external heater/refrigerator to control the temperature. (b) Typical conductance controlled oxidation in 1M H_2SO_4(aq) with 30 mV bias. After a finite drop in conductance, the oxidation potential is reversed to avoid further oxidation. (c) Conductance as a function of potential: before oxidation, after oxidation, after overnight coupling with probe DNA and after exposure to target DNA at 100 mV source-drain bias.

by a circular heater/refrigerator. Because of the large thermal mass, the smaller reservoir has the same temperature as the large reservoir. Probe DNA, terminated with an amine group and a three-carbon linker at the 5′ end is covalently attached to the carboxyl defect on the nanotube through a standard coupling reaction using sulfo-N-hydroxysuccinimide (sulfo-NHS) and 1-ethyl-3-(3-dimethylaminopropyl) carbodiimide (EDC). After thoroughly rinsing the device with deionized water, all subsequent measurements are carried out in phosphate buffered saline solution (1X PBS, pH=7.4). After attaching the probe DNA to the point defect in the nanotube, the temperature is controlled with the thermal water bath (0.1°C). When thermal equilibrium is reached (∼10 minutes), we monitor the device conductance for periods of 30 seconds. Without the presence of target DNA, the devices show no particular features in a conductance dominated by flicker (1/f) noise as shown in Fig. 6.11a.

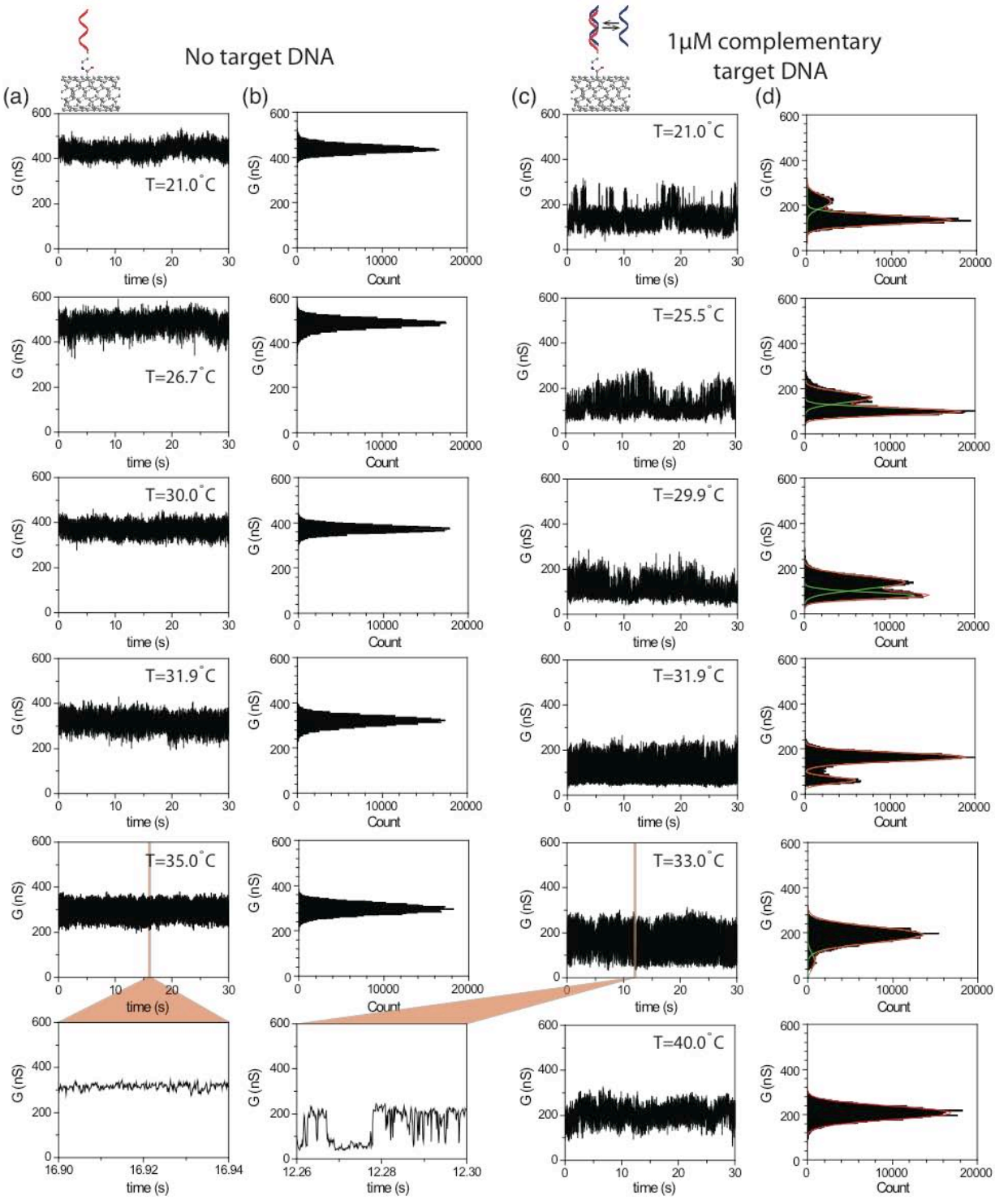

Figure 6.11: Real time measurements of DNA kinetics. (a) Conductance controlled recordings of Device 1 over one 30 s interval with DNA oligonucleotide probe NH_2-5′-GGAAAAAAGG-3′ (A_6) without exposure to complementary DNA in 1X PBS. (b) Conductance based histograms of time intervals shown in a. (c) Same device as in a but with 1 μM complementary target DNA added. (d) Conductance based histograms of time intervals shown in c.

When the device is immersed in buffer containing complementary target DNA, however, large-amplitude two-level fluctuations appear as shown in Fig. 6.11c with a conductance difference of approximately 60-100 nS with an SNR of better than three over the 1/f noise background for a time interval of 30 seconds. The real time conductance data of a representative device (Device 1) is shown with the probe DNA NH_2-5-GGAAAAAAGG-3 (probe A_6) and 1 μM complementary target DNA. The two conductance states have a strong temperature dependence: the device is mostly in the low-conductance state at low temperature and in the high-conductance state both at high temperature and prior to the addition of target DNA. Around the melting temperature, the two states are similarly occupied. Due to this evident temperature correlation, we propose a model in which the conductance is modulated by probe-target hybridization, consistent with other observations that target DNA binding to covalently attached DNA probe reduces tube conductance [95] due to increased scattering and charge transfer at the defect created by the target attachment. The low conductance state represents a device with duplex DNA and the high conductance state represents a device with unbound probe DNA. In principle, longer DNA strands should increase scattering further and result in larger amplitude fluctuations, but we expect that this effect would be partially offset by Debye screening from the dissolved solution counterions. This will be discussed in detail in the next Chapter. The above model is further supported by the observation that these two-level fluctuations are not observed in pristine control devices without electrochemical modification either before or after the addition of target DNA as shown in Fig. 6.12 and control devices that have been linked with probe DNA with non-complementary target as shown in Fig. 6.13. We note that there is a baseline drop in the conductance after DNA target is added, which we attribute to non-specific adsorption [93].

We can relate the conductance modulation to a change in the transmission probability at the defect using the Landauer-Bttiker formalism [205] as

$$R_{total} = R_c + \frac{h}{4e^2}(1 + \frac{1-T}{T}) \tag{6.1}$$

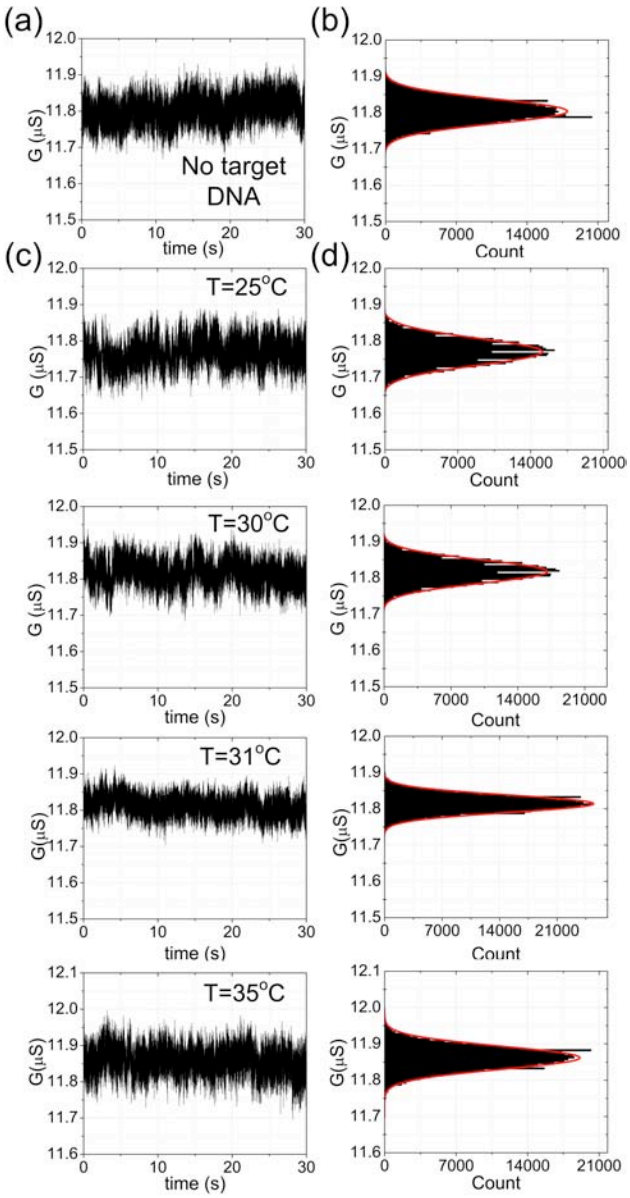

Figure 6.12: Conductance recording for non-functionalized device.

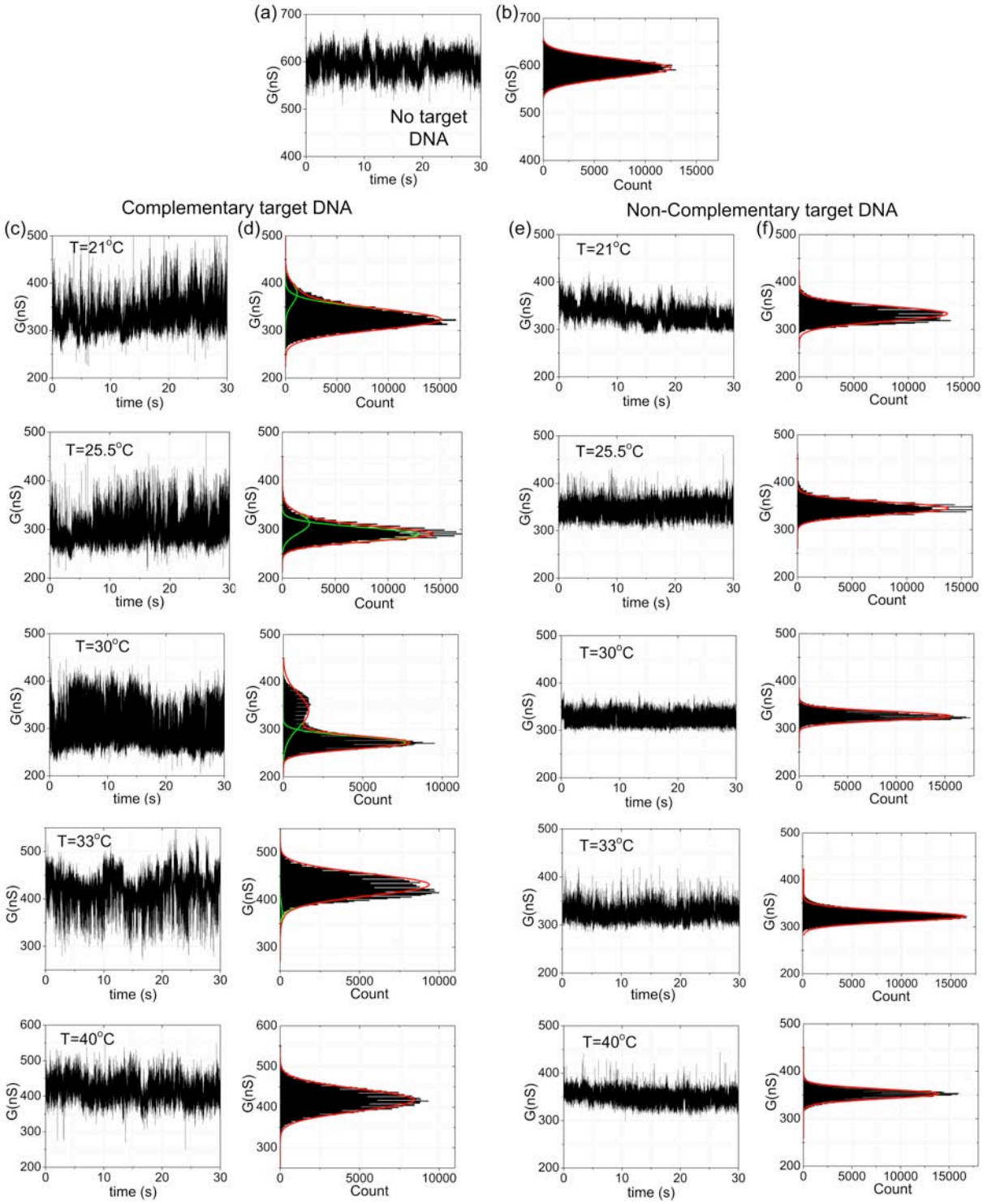

Figure 6.13: Conductance recording for device exposed to complementary and then non-complementary DNA

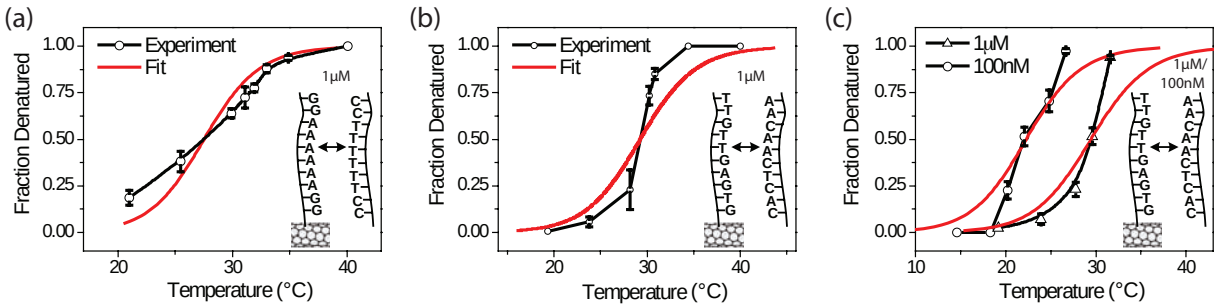

Figure 6.14: DNA melting curves. (a) Melting curve extracted from nanotube two-level fluctuations (Device 1) for probe DNA NH_2-5'-GGAAAAAAGG-3' (A_6) and complementary target with van't Hoff fit. (b) Melting curve extracted from nanotube two-level fluctuations (Device 2) for probe DNA with DNA probe NH_2-5'-GTGAGTTGTT-3' (A_1) and complementary target with van't Hoff fit using Device 3. Error bars are calculated from at least eight different 30 s intervals at each temperature.

where R_c is the resistance of the device before oxidation and T is the transmission probability through the defect. For this particular device, R_c=53kΩ and the transmission probability changes from 0.0055 before adding DNA target to roughly 0.0018 with target; that is, when the target DNA binds, the transmission probability is modulated by a factor of three. Neither AFM nor SGM techniques have sufficient spatial resolution to determine if the change in the device happens at a single carboxylate or if only a single DNA molecule covalently attaches to the nanotube. Multiple DNA probes could be attached to the nanotube leading to multi-level fluctuation; however, because of the strong two-level fluctuations, we conclude that only a single DNA interaction dominates the conductance modulation and the fluctuations are fit to a two-level model.

By taking the ratio of the areas under the low and high conductance state curves from the Gaussian fits in Fig. 6.11d, we obtain the melting curve shown in Fig. 6.14. We also obtain melting curves of the same DNA duplex in solution through ultraviolet-visible absorption spectroscopy (UV-Vis) as shown in Fig. 6.15a.

Assuming a two-state model where the DNA strands are either in single or in duplex form, the equilibrium constant, K, in solution is given by Eqn. 2.3, $K = \frac{2\alpha}{(1-\alpha)^2 C}$ where α is the fraction of total strand concentration C that is in duplex form [206]. For surface based hybridization, the equilibrium constant can be written as the Langmuir isotherm

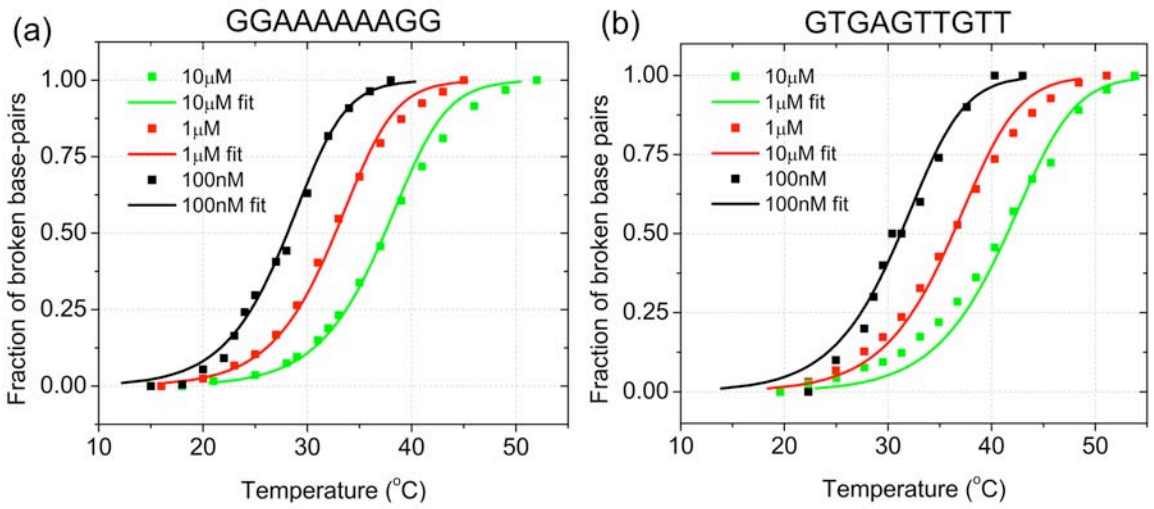

Figure 6.15: Melting curves from UV-Vis for probe DNA sequence NH_2-5'-GGAAAAAAGG-3' and complementary target and also (b) melting curves for probe DNA sequence NH_2-5'-GTGAGTTGTT-3' and complementary target.

$K = \frac{\alpha}{(1-\alpha)C}$ [207]. For both surface- and solution-based hybridization, we can then relate the temperature to the fraction of DNA in duplex form through the thermodynamic relation, $-RTln(K) = \Delta H^\circ - T\Delta S^\circ$. The melting temperature of the DNA duplex (where α =0.5) as measured by the nanotube (T_m= 27.5°C) is slightly lower and the transition is sharper compared to the free DNA (T_m = 32.3°C). A similar observation has been made for DNA linked to gold nanoparticles [208] and RNA adsorbed to carbon nanotubes [209] due to interactions between the molecules and the surface [210]. This is considered further below in the context of analyzing the results of the kinetic studies.

Figs. 6.14b and c show the melting curves extracted for a different probe oligonucleotide NH_2-5-GTGAGTTGTT-3 (probe A_1). The results are shown for a nanotube device (Device 2) with 1 mM complementary target concentration (Fig. 6.14b) and another device (Device 3) with both 1 mM and 100 nM complementary target concentrations (Fig. 6.14c). We observe that the lower target concentration reduces the melting temperature, similar to what has been observed in bulk solution. We summarize the thermodynamic properties for both DNA strands and compare them to results with standard UV-Vis analysis in Table 6.1.

DNA	Method	$\Delta H°$ (kJ mol^{-1})	$\Delta S°$ (kJ K^{-1}mol^{-1})	T_m(°C) at 1μM	E_a (kJ mol^{-1}) (hybridizing)	E_a (kJ mol^{-1}) (melting)
Probe (A_6): NH_2-5′-GGAAAAAAGG-3′ Target: 3′-CCTTTTTTCC-5′	UV-Vis	384	1134	32.3	-	-
Probe (A_6):NH_2-5′-GGAAAAAAGG-3′ Target: 3′-CCTTTTTTCC-5′	CNT	313	923	27.5	-142	44/398
Probe (A_1):NH_2-5′-GTGAGTTGTT-3′ Target: 3′-CACTCAACAA-5′	UV-Vis	357	1026	36.2	-	-
Probe (A_1):NH_2-5′-GTGAGTTGTT-3′ Target: 3′-CACTCAACAA-5′	CNT	239	674	29.4	-202	225

Table 6.1: Thermodynamic properties of DNA hybridization comparing solution based UV-Vis measurements and conductance-based single-molecule carbon nanotube experiments.

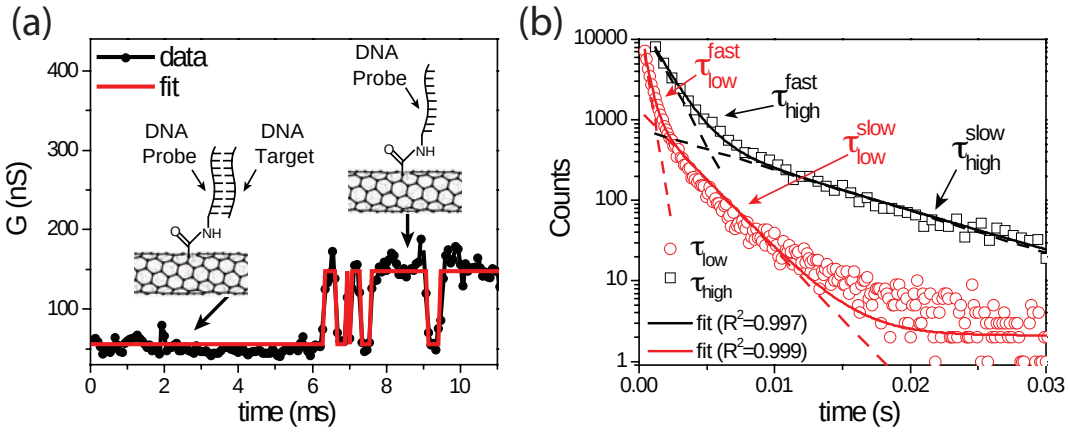

Figure 6.16: DNA kinetics extraction using HMM. (a) Conductance of Device 1 (from Fig. 6.11a) showing experimental data and idealized fits resulting from hidden-Markov-model analysis. Inset: associated bound and unbound state of the probe DNA. (b) Example of double exponential fitting at 1 μM target concentration and 32°C showing both fast and slow lifetimes (Device 3).

6.5 Single-molecule hybridization kinetics

With a relatively low SNR ratio, extracting the kinetic data cannot be easily done. Similar to other single-molecule studies, statistical methods are used to analyze the data and extract important dynamical properties.

6.5.1 Hidden Markov Model

A Markov Chain is a model in which the state of a system is given by a random variable. Given that the system is in a certain state, there is a probability to transition to a different

state. Therefore the state will change over time. A Markov Chain can be described by the initial state and the transition probabilities [211]. In a real system, the internal state of a system can only be inferred to by a set of external observables, which often have some degree of variability such as noise as shown in Chapter 2. This leads to the concept of Hidden Markov Model (HMM) in which the states are not observable but statistical methods can be used to extract the original information. Several different algorithms have been developed such as the Baum-Welch algorithm [212] or Viterbi algorithm [213] to find the most likely sequence of states. HMM has been used in many different applications such as speech recognition [214], sequencing [215], protein structure [216] and single-molecule modeling [217,218]. In particular, HMM has been successfully used to analyze noisy FRET data and extract the states and also the dwell times [219]. Fig. 6.16a demonstrates how an HMM model can be used to idealize the conductance data for the carbon nanotube.

6.5.2 Autocorrelation

Another method to extract the kinetics is by taking the autocorrelation of the conductance. This method has been used for FCS based experiments when the FRET intensity levels cannot be clearly identified and the SNR ratio is low. The autocorrelation of the conductance is given by

$$A(\tau) = \frac{< G(t)G(t+\tau) >}{< G^2(t) >} - 1 \tag{6.2}$$

The autocorrelation of the conductance has been plotted in Fig. 6.17b for a device with no target DNA and then immersed in 1 μM target DNA. Ideally, the autocorrelation should fit to an exponential, but because of noise (mostly flicker noise in the carbon nanotube), a stretched exponential function was shown to best fit the data. Similar to FCS experiments, the autocorrelation can then be fit to

$$A(\tau) = A(0)e^{-(\frac{t}{\tau})^{\beta}} \tag{6.3}$$

Where beta is the stretching parameter ($0< \beta <1$). This equation has been used for

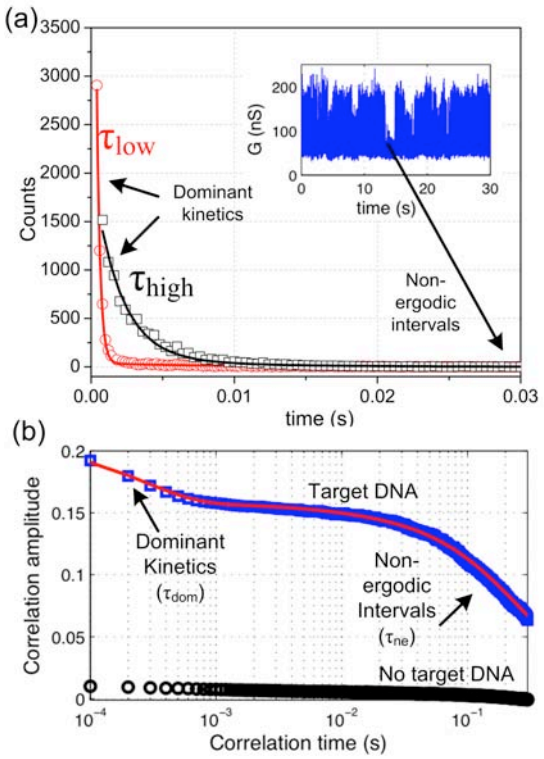

Figure 6.17: DNA kinetics extraction using the autocorrelation of the conductance. (a) There are non-ergodic time intervals where the fluctuations stop. These are represented by long tails in the lifetime histograms after HMM analysis. (b) The same intervals can be found in the autocorrelation based kinetics extraction along with the dominant kinetics.

fitting both the dominant and the non-ergodic time intervals as shown in Fig. 6.17b. One problem arises because the autocorrelation based dwell time extraction is a combination of the high and low rates, given by $1/\tau = 1/\tau_{high} + 1/\tau_{low}$. By also knowing the melting curve where the melted fraction can be written in terms of the high and low dwell times as $M = \frac{\tau_{high}}{\tau_{high}+\tau_{low}}$, both the high and low dwell times can be computed.

6.5.3 Carbon nanotube kinetics extraction

In order to study the kinetics of DNA hybridization and obtain further insight into the thermodynamics observed through time averaging of a single molecule system, we extract (as shown in Fig. 6.16a) the dwell times in the high (τ_{high}) and low states (τ_{low}) in the presence of flicker noise by idealizing the transitions using a hidden Markov model (incorporated in the vbFRET software package) [218], which has been used in smFRET experiments to study

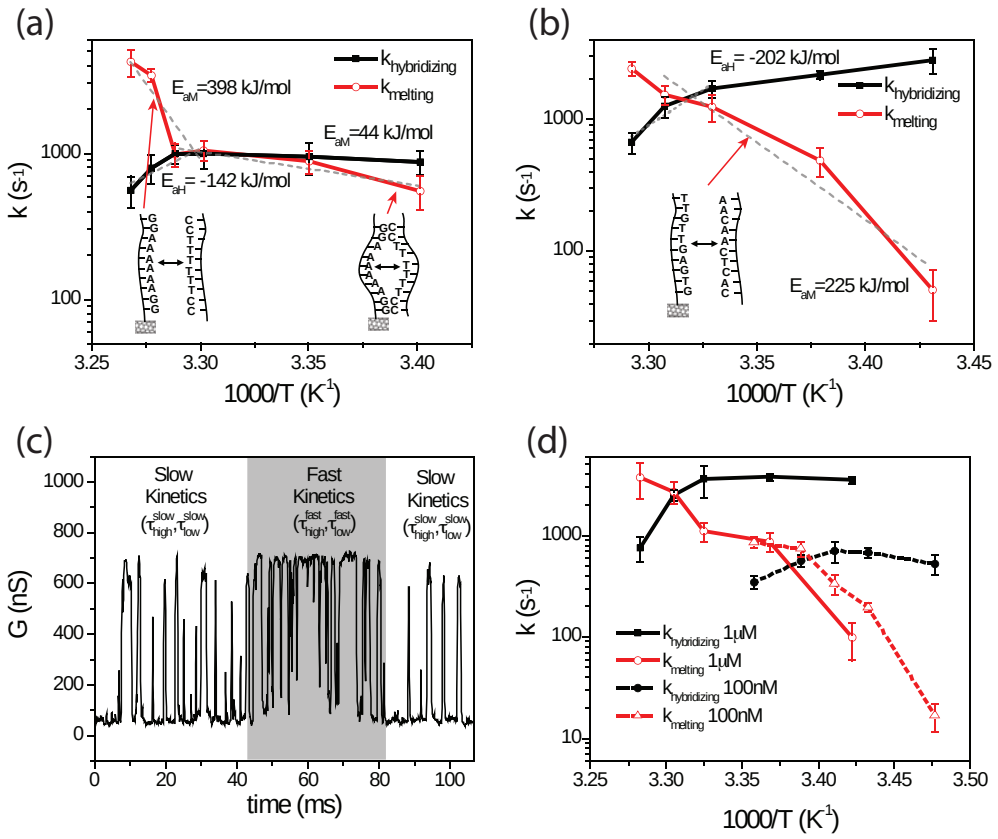

Figure 6.18: (a)Arrhenius plot showing hybridization and melting rates for Device 1. A sharp transition in activation energy is shown around the melting temperature and is attributed to bubble kinetics a lower temperatures. (b) Arrhenius plot of Device 2. There is no sharp transition in the activation energy. (c) Conductance data showing intervals with both fast and slow kinetics. (d) Arrhenius plot showing hybridization and melting rates for 100 nM and 1 μM complementary target concentrations (Device 3). Error bars for the Arrhenius plots are calculated from at least sixteen different 15 s intervals.

conformational changes in biomolecules [219]. To reduce random drift, the data is split into 15 second intervals and then fit to a two-level model. These idealized traces are then used to extract the dwell times in the high and low states by generating dwell time histograms at each temperature (shown in Fig. 6.16)b which can be best fit to a double exponential of the form

$$y = y_0 + A^{fast} e^{-\frac{t}{\tau^{fast}}} + A^{slow} e^{-\frac{t}{\tau^{slow}}} \tag{6.4}$$

The superscript fast indicates the shorter and slow the longer lifetime of the fit, such

that $t_{high}^{fast} < t_{high}^{slow}$ and $t_{low}^{fast} < t_{low}^{slow}$ (the R^2 values of the fits are always greater than 0.97). The subscripts high and low are used to indicate the lifetime of the high and low states respectively. The extracted lifetimes are used to generate the Arrhenius plot in Fig. 6.18.

The origin for the double exponential may be the result of two competing pathways for hybridization. Similar models have been used to describe DNA hybridization kinetics with immobilized probes on silicon or glass [220] and how proteins find specific target sites along DNA strands [221,222]. In this model, target DNA reach probe by either 3D diffusion or non-specific adsorption followed by surface diffusion. As shown in Fig. 6.18c, the nanotube conductance switches between two distinct kinetic modes which have different time constants. How these time constants are associated with solution-based or surface-based kinetics is determined by examining the concentration dependence of the associated dwell times. From chemical kinetics, we expect the solution hybridization rate ($k_{hybridization}$) to be proportional to DNA target concentration (bimolecular process) and the solution melting rate ($k_{melting}$) to be independent of concentration (unimolecular process). Fig. 6.18d shows the Arrhenius plot for Device 3 with 100 nM and 1 μM complementary target concentration using $\mathrm{k}_{hybridizing} = 1/\tau_{high}^{fast}$ and $\mathrm{k}_{melting} = 1/\tau_{low}^{fast}$ for the 1 μM concentration and $\mathrm{k}_{hybridizing} = 1/\tau_{high}^{slow}$ and $\mathrm{k}_{melting} = 1/\tau_{low}^{slow}$ for the 100 nM concentration so that the hybridizing and melting rates behave as expected based on solution ensemble experiments and as described above. We believe that the target concentration at which $\mathrm{k}_{hybridization}$ ($\mathrm{k}_{melting}$) goes from being determined by τ_{high}^{fast} (τ_{low}^{fast}) to being determined by τ_{high}^{slow} (τ_{low}^{slow}) depends on the ratio of one-dimensional and three-dimensional diffusion rates and the concentration dependence of the surface-based hybridization and melting rates.

The dwell time histograms for both DNA sequences over all measurements (temperature and target concentrations) can be best fit by a double exponential. This behavior originates from the system switching between two distinct kinetic modes (Fig. 6.19). We have identified and analyzed longer time intervals in which the system stays in only one of these modes. Fig. 6.19b and c shows the dwell time histogram at 1 μM DNA target concentration (Device 3), in which the system is in either the fast mode (total of three sec-

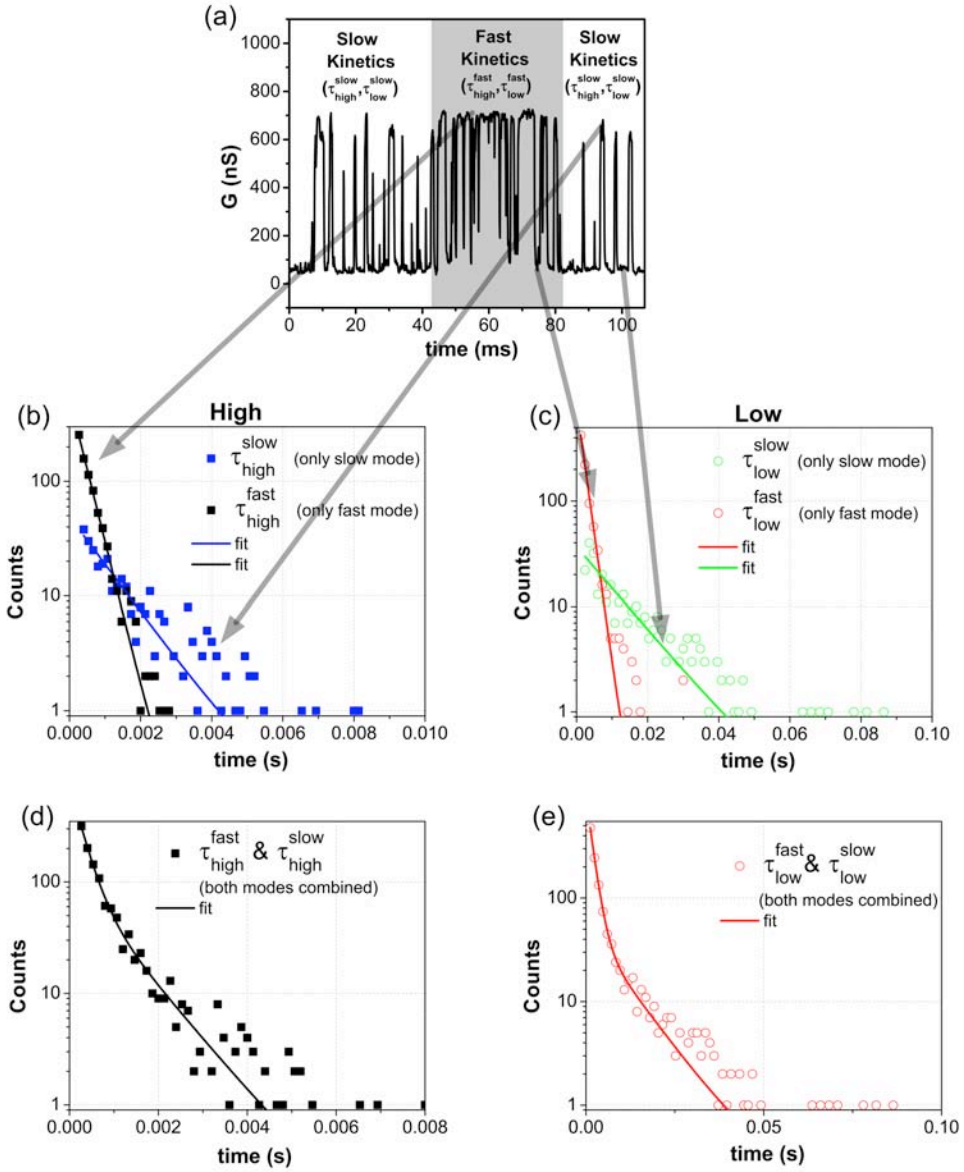

Figure 6.19: (a) Real time conductance data showing both surface and solution modes. (b,c) Dwell time histograms when modes are decoupled for high and low states. (d,e) Combined dwell time histograms when both modes are present leading to a double exponential.

onds) or slow mode (total of five seconds). When we analyze only a single mode, the dwell time histograms are largely mono-exponential and can be best fit with a single exponential function. This analysis also demonstrates that in the fast kinetic interval, both high and low lifetimes are shorter than in the slow kinetic interval. This behavior was seen over all temperatures and for both measured concentrations. When we analyze intervals with both modes present (6.19d and e), the dwell time histogram have a double exponential because of the combination of the fast and slow modes.

Arrhenius plots for $k_{hybridization}$ and $k_{melting}$ at 1 μM target concentration for Devices 1 (probe A_6) and 2 (probe A_1) are presented in Figs. 6.18a and b, respectively. The Arrhenius plot of Device 2 (Fig. 6.18b) looks very similar to ones reported [44, 45] for DNA duplex kinetics studied with DNA hairpins. The melting rates ($k_{melting}$) follow Arrhenius-like behavior and are very dependent on temperature while the hybridization rates ($k_{hybridizing}$) have anti-Arrhenius behavior and are only slightly temperature-dependent. This anti-Arrhenius behavior yields a negative activation energy, which implies that the reaction rate decreases with increasing temperature and the free energy barrier arises from a significant loss of entropy [223]. The slight curvature in the Arrhenius plot has also been observed with DNA hairpin hybridization [44] and protein folding [224] and is attributed to a change in the rate limiting step of the reaction as a function of temperature, because of a significant temperature dependence in either the activation entropy or enthalpy [225, 226].

The Arrhenius plot of Device 1 (Fig 6.18a) shows a remarkably different behavior for $k_{melting}$, with a sharp change in activation energy around the melting temperature. At temperatures less than the melting temperature, kmelting has a small activation energy (44 kJ/mol) that can be seen from the shallow slope in the Arrhenius plot. We attribute this to breathing of the DNA duplex (probe A_6 for Device 1) which consists of six adenine-thymine (AT) base pairs that are enclosed by guanine-cytosine (GC) bases. This differs from the A_1 duplex (for Devices 2 and 3), which has at most two neighboring AT bases. We speculate that the fluctuations below the melting point for Device 1 could be due to bubble dynamics

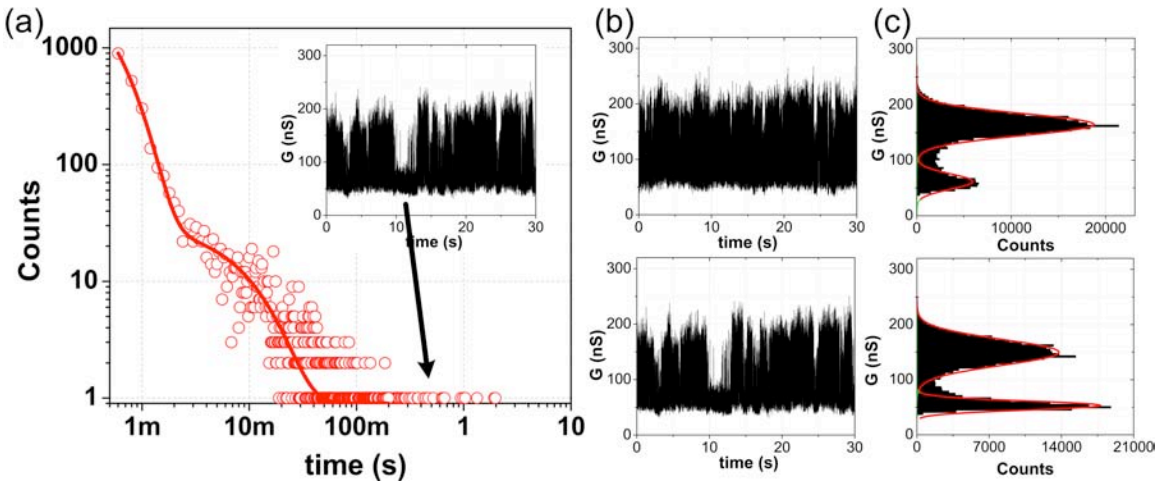

Figure 6.20: (a) Effect of non-ergodic time intervals on the lifetime histograms. (b) Effect of non-ergodic time intervals on the conductance based histograms (taken at the same temperature).

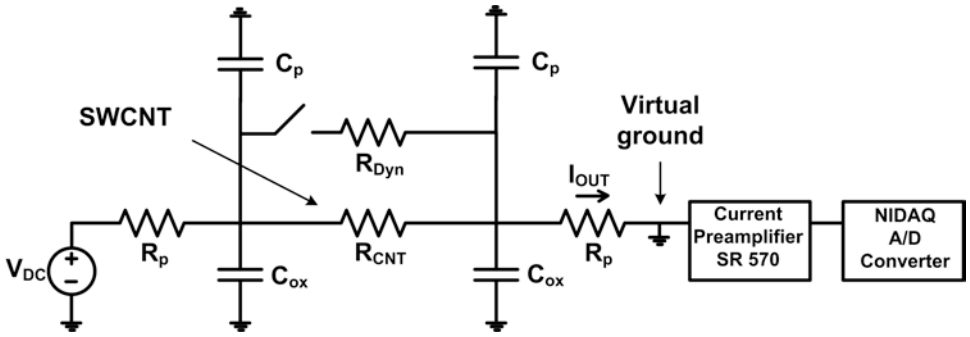

Figure 6.21: Equivalent circuit of carbon nanotube in aqueous solution. The DNA kinetics are modeled by a parallel resistor being switched in and out.

of the AT region which have been previously reported [227,228]. In addition to the solution and surface modes, we also observe occasional several-second-long non-ergodic time intervals when the fluctuations stop as shown in Fig. 6.20, which could be due to reversible states in which the DNA complex may adhere to the nanotube surface in a conformation that impedes the binding dynamics. From the dwell time histogram, we estimate the percentage of non-ergotic time intervals to be approximately 10% of the total monitored time.

6.6 Bandwidth of nanotube device

The bandwidth of the nanotube device itself is limited by extrinsic parasitics. The equivalent circuit is shown in Fig. 6.21. Here R_{CNT} is the resistance of the nanotube, R_p is the resistance in the leads (due to the resistivity of titanium), C_{ox} is the capacitance from the leads to the substrate and C_{sol} is the parasitic capacitance from the source and drain electrodes to the electrolyte. The intrinsic bandwidth of the device can be found by assuming that the biomolecule changes the resistance, which is approximated by another resistor in parallel (R_{Dyn}) with the nanotube resistance. If the DNA hybridizes, the switch opens and the resistance increases, if the DNA melts, the switch closes and the overall resistance decreases.

From DC measurements, the electrode resistance is assumed to be approximately $R_p = 5k\Omega$ and the oxide capacitance about 14 pF. The capacitance from the electrolyte to the titanium was measured with a standard AC impedance potentiostat measurement in 1X PBS on a 100x100 μm^2 electrode (the leads were passivated by a 5 μm SU-8 layer). The extracted impedance magnitude and phase is shown in Fig. 6.22a and b. This impedance was modeled by an equivalent circuit as shown in the inset of Fig. 6.22. The dominant capacitance is the smaller one (there are two capacitances in series from the electrolyte interface and the native titanium oxide) which came out to be approximately 31 $fF/\mu m^2$, which is the same order of magnitude as reported in literature [229]. For the electrodes in the experiment (width=20 μm and length about 3 mm, the total capacitance is about 1.86 nF. The other values extracted are shown in the table.

Assuming that parallel resistance is a fraction α of the nanotube resistance so that $R_{Dyn} = \alpha R_{CNT}$, this leads to two coupled KCL equations which can be solved for the current I_{OUT}. Assuming that $R_p << R_{CNT}$, the solution to the above equation gives a corner frequency of the device at $f_c = \frac{1}{2\pi R_p C}$ where $C = C_{ox}||C_{sol}$ is the parallel combination of the oxide capacitance and the electrolyte capacitance. For the device used in this experiment, this value comes out to be approximately 17 kHz. At a preamplifier gain of 200 nA/V, the bandwidth was limited to about 4.8 kHz at a measurement filter corner frequency of 10

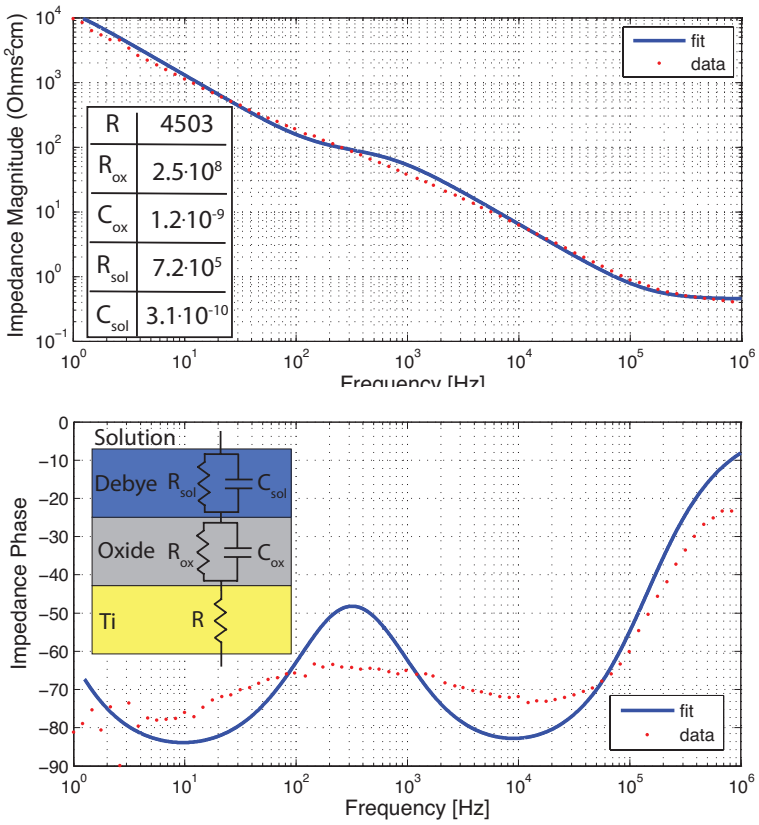

Figure 6.22: Titanium electrode parasitics showing both (a) magnitude and (b) phase of the titanium electrodes in 1X PBS buffer solution by A.C. impedance. The measurement was done using a potentiostat with Ag/AgCl reference electrode, a platinum counter electrode and a 100×100 μm^2 electrode as the working electrode. The table shows the extracted values from the fit to a equivalent circuit in the inset in b. This measurement was performed by Steven Warren.

kHz.

6.7 SNR ratio

The noise of the point functionalized carbon nanotube at low frequencies is dominated by flicker (or 1/f) noise, which can be seen from the measured power spectrum in Fig. 6.23 (calculated from the Fourier transform of the autocorrelation function). This background 1/f noise is higher in the presence of target DNA where two very small Lorrentzian curves can be seen. The signal is determined by the conductance difference between the two peaks in Fig. 6.24. The noise is determined by integrating the noise spectrum from f_{lower} =

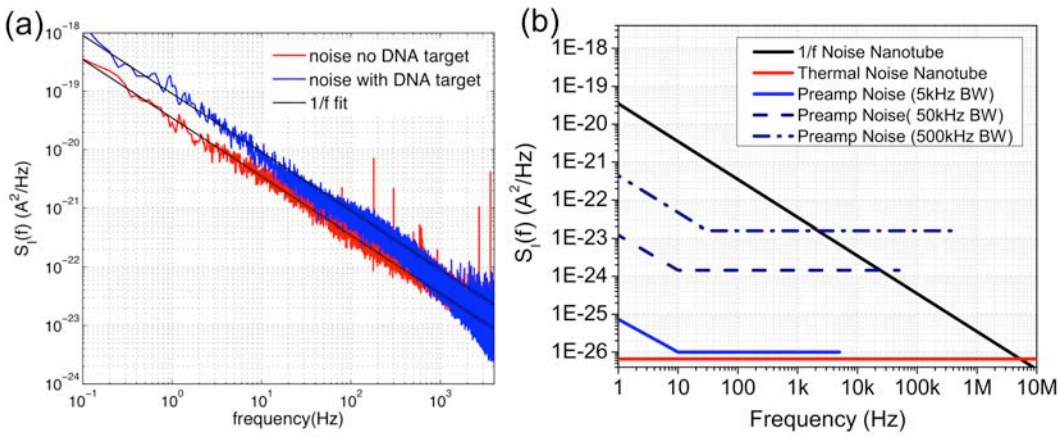

Figure 6.23: (a) Flicker noise for device shown in Fig. 6.11 with and without target at 31.9 °C. (b) System level noise characterization. At high bandwidth, the noise of the amplifier surpasses the noise of the nanotube.

$1/T_{window}$ (where T_{window}=30 s is the length of the analyzed time window) and f_{upper}, the bandwidth established by the measurement equipment (approximately 5 kHz). The resulting SNR is shown in Table 6.2 as "SNR (from 1/f)". Another approach to quantify the noise is by measuring the standard deviation of the Gaussian fits in Fig. 6.24, reported as "SNR (from σ)". We find this noise floor to be slighter higher than the one computed from the integrated 1/f spectrum because of additional power supply noise harmonics, which are not integrated in the 1/f noise calculation. The SNR ratio can be improved by decreasing T_{window} (Fig. 6.24), since this results in a higher low-frequency cutoff, reducing the effect of low-frequency noise (drift). T_{window}=15 s is used for the Arrhenius plot fittings in Figs. 6.18a,b and d.

There is also noise coming from the measurement equipment, in this case the current preamplifier (Stanford Research SR570). As the bandwidth of the preamplifier is increased, the noise internally generated by the preamplifier also increases, as shown in Fig. 6.23b (taken from the preamplifiers datasheet). This noise at a bandwidth of 4 kHz, however, is significantly lower than that coming from the nanotube itself. This results in an overall input-referred noise level of 1 nA_{rms} at 100 mV source to drain bias (Table 6.2).

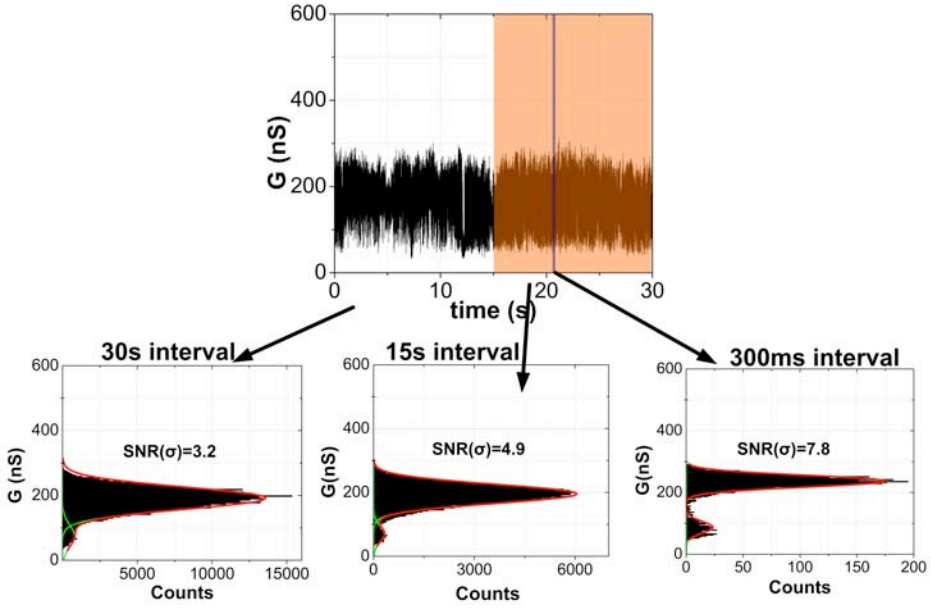

Figure 6.24: SNR for different time intervals.

Noise Nanotube (pA_{rms})	998.4
Noise Preamp (pA_{rms})	14.1
SNR (from 1/f)	5.7-11.7
SNR (from σ)	3-5.3

Table 6.2: Noise calculations at 4 kHz bandwidth for T_{window}=30 s.

Chapter 7

Debye length screening

Point-functionalized carbon nanotube field-effect transistors can serve as highly sensitive detectors for biomolecules. With a probe molecule covalently bound to a defect in the nanotube sidewall, two-level random telegraph noise (RTN) in the conductance of the device is observed as a result of a charged target biomolecule binding and unbinding at the defect site. Charge in proximity to the defect modulates the potential (and transmission) of the conductance-limiting barrier created by the defect. In this chapter, the effects of these single-molecule electronic sensors on ionic screening are studied [230]. Both charge in proximity to the defect site and buffer concentration are found to affect RTN amplitude in a manner that follows from simple Debye length considerations. RTN amplitude is also dependent on the potential of the electrolyte gate as applied to the reference electrode; at high enough gate potentials, the target DNA is completely repelled and RTN is suppressed.

7.1 Introduction

Point functionalization of the nanotube channel, which creates a conductance-dominating scatterer as well as a chemically reactive site for molecular attachment, greatly enhances the sensitivity of the device to charge in the region of the defect [101, 231]. In the previous Chapter, the appearance of two-level random telegraph noise (RTN) in the conductance of the device was shown as a result of a biomolecule binding and unbinding from the defect

site thereby modulating the transmission through the defect [174]. This RTN data can be analyzed to study the kinetics and thermodynamics of the interaction by monitoring the conductance as a function of temperature. In this case, all the information extracted from the sensor is contained in the dynamics of the conductance transitions. In this Chapter, the conductance magnitude of the two-level RTN as a function of the distance between the biomolecule and the nanotube and as a function of buffer concentration are instead examined.

Previous sensing experiments with nanowire field-effect transistors have demonstrated that charges on biomolecules can be screened by increasing the distance of the biomolecule from the nanowire surface [232] or by increasing the buffer concentration [233, 234]. As demonstrated here, the single-molecule response of these devices is also screened by the counterions in the buffer solution. As a result, Debye screening constitutes an important design consideration for label-free single-molecule detection in order to maximize RTN signal by optimizing buffer concentrations, linker and molecular arrangements, and applied electric fields [235].

7.2 Automated microfluidic setup

7.2.1 On-chip platinum electrode

The fabrication method for the point functionalized carbon nanotube devices was described in more detail in Chapter 4. In order for easy integration with the fluidic system described below, an on-chip platinum electrode was fabricated for controlling the solution potential. The thickness of the platinum electrode is 75 nm with a 2 nm titanium adhesion layer. As shown in Fig. 7.1a, the on-chip platinum electrode can be used to electrolytically gate the carbon nanotube device in 1X PBS buffer solution. The hysteresis in the gate sweep is only about 8 mV at a sweep rate of 5 mV/s. Because titanium is used for the source and drain electrodes of the device, the gate leakage current (shown in Fig. 7.1b) is below 300 pA, which is more than 20 times smaller than the smallest measured device current.

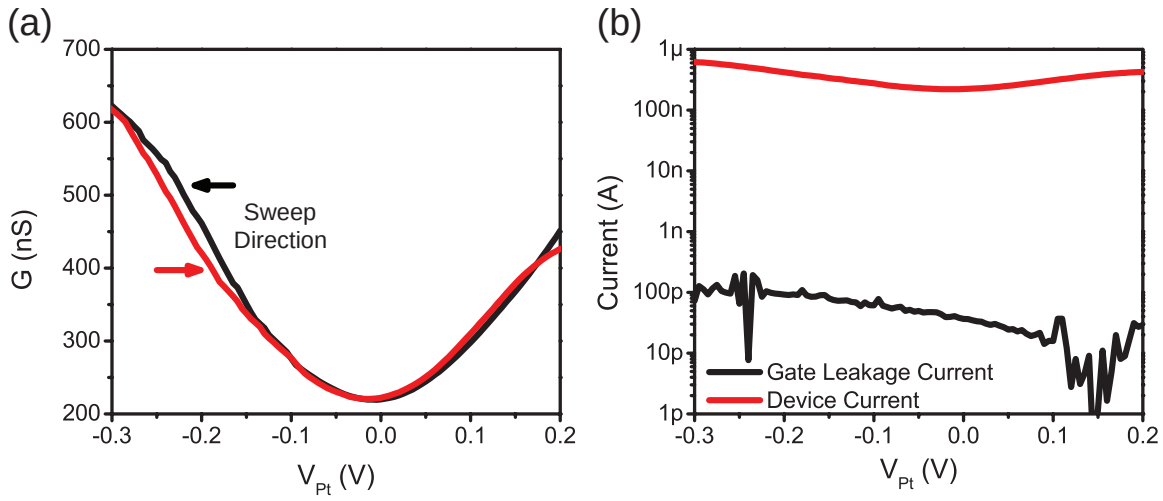

Figure 7.1: On-chip platinum electrode as gate. (a) Hysteresis of on-chip pseudo reference electrode. (b) Gate leakage current through 1X PBS buffer solution.

After a short transient of around 30 minutes, the open circuit potential between the Ag/AgCl (3M NaCl) reference electrode (Bioanalytical Systems; 0.209V vs. Normal Hydrogen Electrode (NHE)) and the on-chip platinum electrode is very stable as shown in Fig. 7.2a with a standard deviation of only 1 mV over a 90-minute observation period. The absolute value of the on-chip platinum open circuit potential is about 300 mV above the potential of the platinum wire and the platinum evaporated on a glass slide (during the same evaporation step) as shown in Fig. 7.2b. We believe that this is the result of the annealing step in a forming gas (Hydrogen/Argon) at 340 °C. Similar to hydrogen plasma experiments [236,237], the forming gas annealing step reduces the amount of platinum oxide at the surface of the platinum electrode and therefore reduces the open circuit potential.

7.2.2 Microfluidic channel

After wire-bonding, the chip is assembled in a microfluidic setup with a poly(dimethylsiloxane) (PDMS) mold as shown in Fig. 7.3a. This microfluidic channel inside the PDMS mold was defined using a standard fabrication method [238]. Briefly, a master is patterned on a silicon chip using SU-8 resist (Microchem Corp.) and soft lithography to define the channel. The master chip is then coated with a thin layer silane layer (trimethoxysilane) using silane vapor in a closed container in order to avoid permanent bonding of the cured PDMS to the

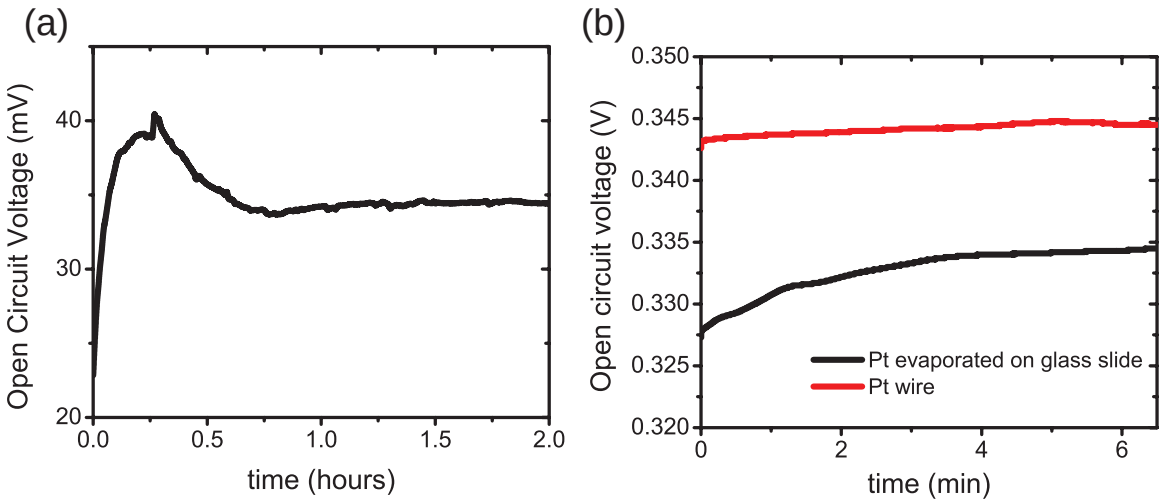

Figure 7.2: Stability of on-chip electrode. (a) Open circuit voltage for on-chip platinum electrode vs. Ag/AgCl reference electrode. (b) Open circuit voltage for evaporated platinum on glass and platinum wire vs. Ag/AgCl reference electrode.

chip. PDMS from a two-component base and curing agent (Dow Corning, Sylgard 184) is poured over the master to about 1 cm in height and cured at 80 °C for 2 hours. The PDMS stamp is peeled off and small holes are drilled into it for connecting the fluid lines to the channel. The tearing of the relatively soft polymer during drilling could be significantly reduced by submerging the PDMS into liquid nitrogen before drilling.

The PDMS mold with the channel is sealed against the substrate with the devices and held in place by epoxy as shown in Fig. 7.3b. Teflon tubing (0.91 mm inner diameter) is mechanically attached to the PDMS channel and permanently bonded by epoxy to create a stable system. The cured PDMS was chemically resistive to the dilute sulfuric acid (1M) and the potassium permanganate (6.5 mM) [239]. The temperature inside the tubing is controlled by a large, grounded water reservoir (1M NaCl). A copper coil provides good thermal coupling to this reservoir and the temperature is controlled by a circular heater/refrigerator (PolyScience 9112). The inside fluid at the channel never gets in contact with the outside heating/cooling bath as shown in Fig. 7.3c.

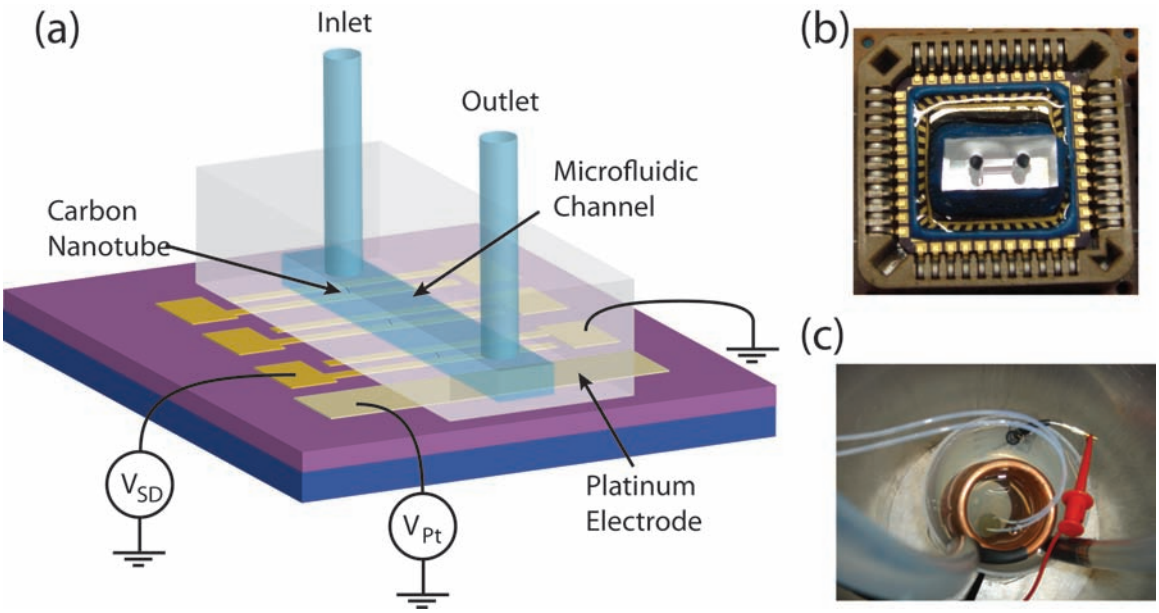

Figure 7.3: Microfluidic cell. (a) Chip with nanotube devices is wire-bonded and encapsulated in a PDMS microfluidic cell. (b) Picture of assembled chip carrier with PDMS mold sealed over the devices. (c) Teflon tubing is connected to the channel and a larger water reservoir is used to heat or cool the tubing and the device (from circular heater/refrigerator.

7.2.3 Fluidic System

The Debye length studies described in this report are facilitated by a microfluidic system shown in Fig.7.4. Different aqueous solutions (with different target DNA or ionic concentrations) can be automatically drawn into the channel with the nanotube devices. Digitally controlled pinch valves, manifolds (NResearch Incorporated), and a syringe pump are used to selectively pull and push solutions from reservoirs into a microfluidic channel and into a waste reservoir. In order to avoid solution mixing, solutions are split up into 120 μL intervals that are separated by $\sim$20 μL air gaps. To deliver a new solution into the channel, a Labview program (National Instruments) automatically cycles through a combination of pulling solution into the fluid lines, pulling an air gap, and finally pushing out solution into the waste reservoir. In this way, the fluid channel above the devices can be first flushed by buffer solution and then the selected solution can be introduced automatically. We have verified that the variation in the solution volume is less than $\sim 20\mu$L when pulling solution into the channel. This setup provides the controlled fluidic platform for the experiments

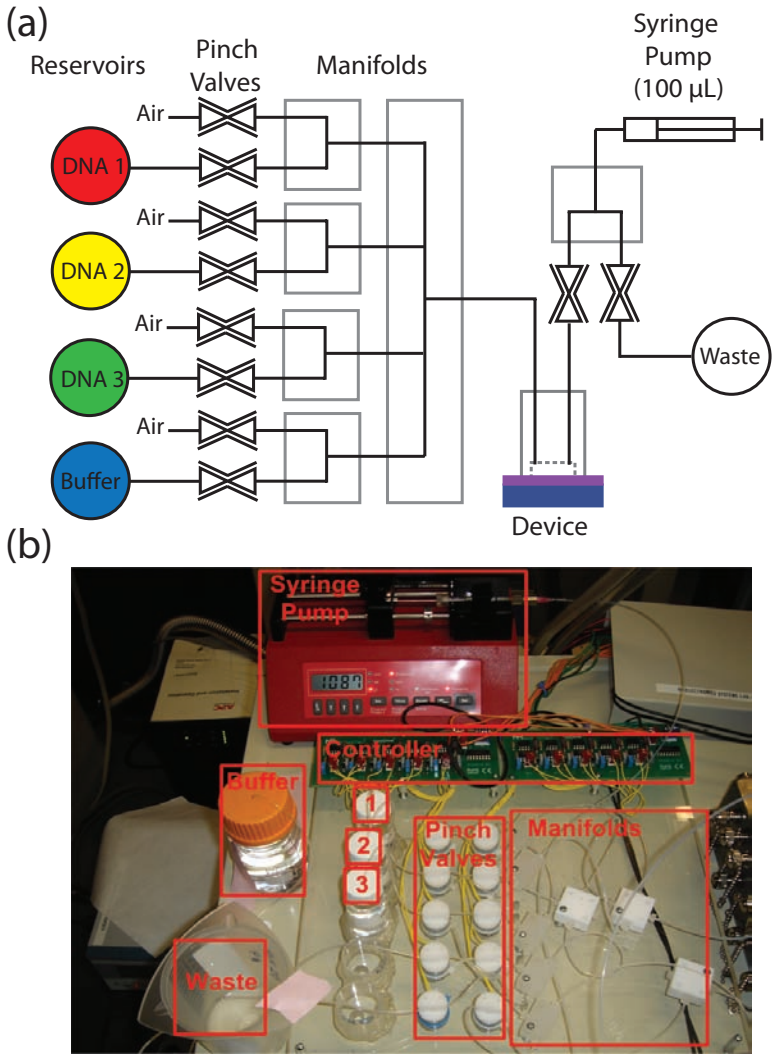

Figure 7.4: Fluid delivery system. (a) Digitally controlled pinch valves and manifolds can automatically deliver solutions into and out of the microfluidic channel with a syring pump. (b) Picture of system implementation.

outlined in this Chapter.

7.3 Charge proximity

The point defect in the carbon nanotube sidewall is created by the electrochemical oxidation method in 1 M H_2SO_4 followed by a 45 s immersion in 6.5 mM $KMnO_4$. After overnight coupling of the probe oligonucleotide NH_2-5′-GTGAGTTGTT-3′ to the carbon nanotube defect, we characterize conductance of the carbon nanotube in 1X PBS buffer. In previous

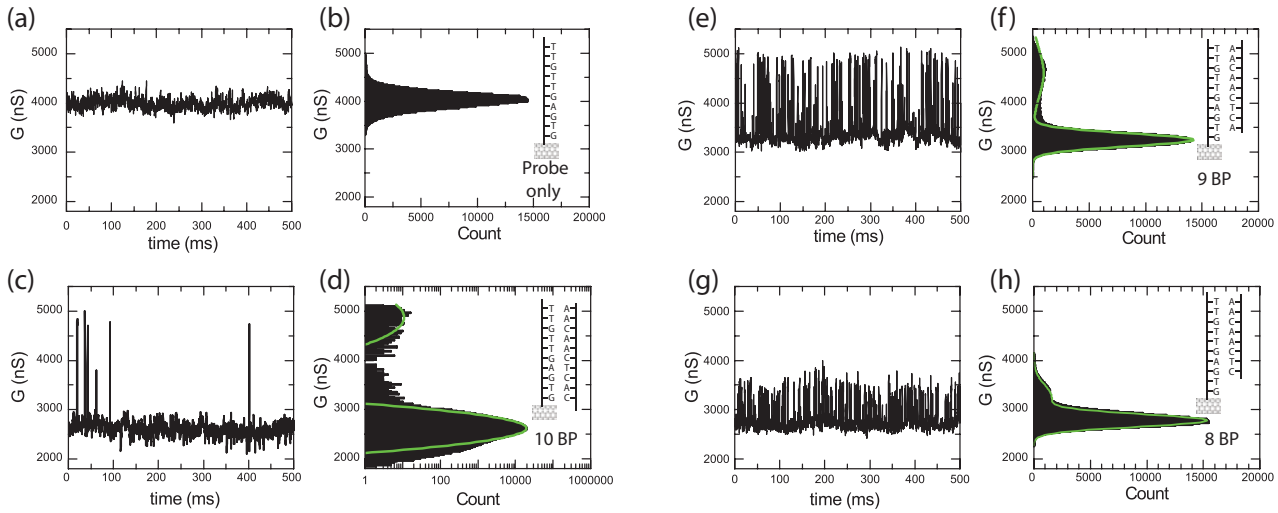

Figure 7.5: Real time measurements of binding kinetics with different target DNA. Conductance recordings are performed at V_{sd}=100 mV and V_{Pt}=-0.3V showing a small intervals from an 8 minute recording. (a) Conductance recording in 1X PBS buffer solution without target DNA. (c,e,g) Conductance recording with 10, 9 and 8 bases of complementary target DNA. (b,d,f,h) Conductance based histograms from 30 s time intervals (of which panels a, c, e and g are small subsets).

studies, we have examined the conductance at different temperatures with and without adding complementary DNA target [174]. Now the temperature is set to 17 °C with a circular heater/refrigerator and different solutions are introduced into the channel. After turning off the fluid flow and equilibrating the temperature, the conductance is measured for periods of eight minutes at a constant pseudo reference potential of -0.3 V, applied to the on chip platinum electrode. Without complementary target DNA, the device shows a conductance that is dominated by flicker noise as shown in Fig. 7.5a and only contains a single state (Fig. 7.5b). Different lengths of target complementary oligonucleotides are now added at 1 μM concentration and the device is again measured for each nucleotide without flow after the equilibrium temperature is reached.

Fig. 7.5c shows the real-time conductance with the corresponding histogram in Fig. 7.5d for an exactly complementary ten-base-pair target DNA (5′-AACAACTCAC-3′). The conductance fluctuation is similar to previous measurements [174], and the device is mostly in the low (bound) state with occasional large but very short spikes corresponding to brief

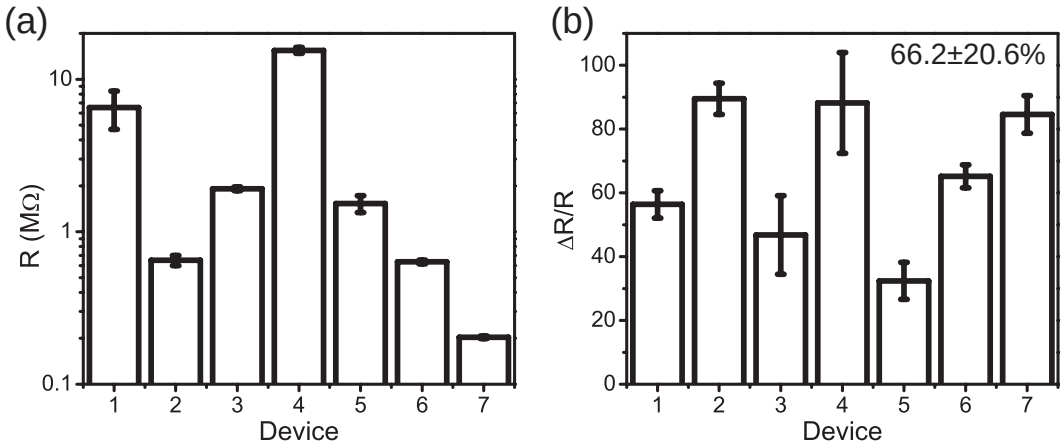

Figure 7.6: Fluctuation variability. (a) Standard deviation of point functionalized device resistance and (b) normalized device RTN amplitude.

intervals in which the probe DNA is unbound to complementary target. This behavior is expected because at 17 °C, the temperature is well below the melting point and the DNA is mostly in the duplex state. Overall, more than 7 devices have been fabricated, which have been functionalized with probe DNA. These devices have a wide variety of resistances spanning almost two orders of magnitude as shown in Fig. 7.6a. The random telegraph noise (RTN) amplitude is relatively invariant with a normalized resistance change of 66.2±20.6 % as shown in Fig. 7.6b, which is taken at 17 or 19 °C, well below the melting temperature. The variability is attributed to differences in the initial nanotube electronic properties, defect geometry, device doping and electrochemical potential.

Fig. 7.5e shows the two-level RTN observed for a complementary nine-base-pair oligonucleotide, one base pair shorter at the 3 end of the target (5′-AACAACTCA-3′), where the 3 end is closest to the carbon nanotube. The amplitude of the two-level RTN is lower in this case as is also evident in the histogram of Fig. 7.5f. An increase in the time spent in the high (unbound) state was also observed, which indicates that the melting curve has shifted toward lower temperature, as expected for a shorter DNA target. For the complementary eight-base-pair oligonucleotide (5′-AACAACTC-3′), shortened now by two based at the 3 end, the amplitude of the RTN further decreases as shown in Fig. 7.5g and in the histogram in Fig. 7.5h. Even though a small overall decrease in the conductance over

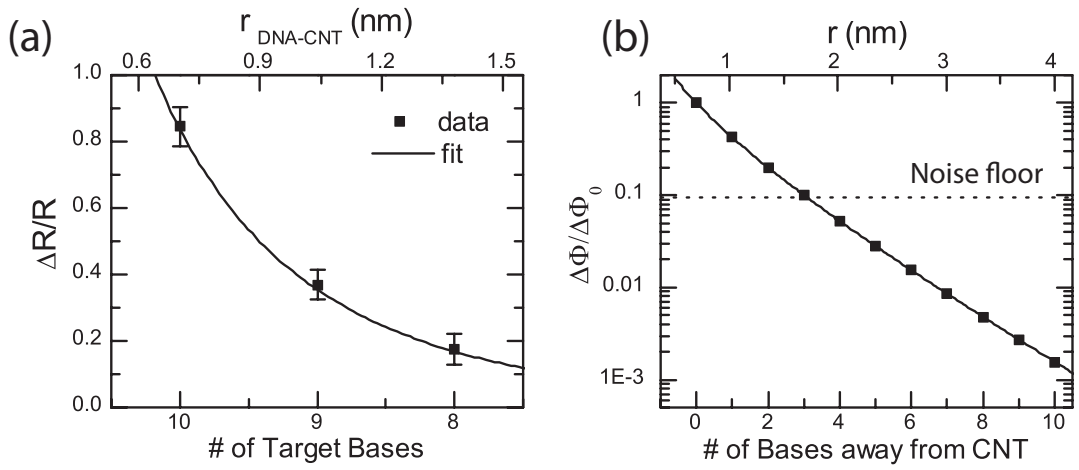

Figure 7.7: Normalized resistance change as a function of length of the target DNA. Nucleotides of the target DNA are removed from the 3′ end, closest to the carbon nanotube. Error bars are calculated from at least 5 different 30 s time interval histograms. (b) Plot of Eqn. X as a function of distance for a Debye length of $\lambda_D = 0.70$ nm (1X PBS). Base pairs further out are almost completely screened by the counterions. The noise floor is calculated for a signal-to-noise ratio of one using the full width at half maximum (FWHM) of the gaussian fits in the histograms in Fig. 7.5d,g and h for the noise amplitude.

several cycles has been observed, which is attributed to non-specific adsorption of target DNA to the sidewall, the fluctuations are repeatable over multiple cycles of flushing buffer and complementary target DNA. In Fig. 7.7a, the normalized change in resistance, ΔR/R is plotted as a function of different target lengths. The RTN amplitude decreases with reduction of the target sequence length at the 3′ end.

To explain the length effect on RTN amplitude, Debye screening theory is used. When a charged molecule is placed in a buffer solution, electrostatic interactions cause counterions to surround the molecule, partially offsetting the molecular charge. A very simple approximation of the resulting screened electric potential from a point charge Q is given by the Debye-Hückel model [240] as

$$\Phi = \frac{Q}{4\pi\epsilon_0}\frac{1}{d}e^{-\frac{d}{\lambda_D}} \tag{7.1}$$

where ϵ_0 is the dielectric constant, d is the distance from the charge, and λ_D is the Debye length. That is, the potential decreases exponentially with distance and the Debye length sets the length scale at which the potential approaches zero.

In Fig. 7.7b, we plot the change in potential ($\Delta\Phi$) normalized to change in potential for the 10-mer target ($\Delta\Phi_0$) as determined by Eqn. 7.1 as a function of the distance between the defect and the position of the first nucleotide on 3 end of the target. Assuming that the DNA is upright and each base is separated by 0.33 nm [241] (the three-carbon linker was estimated to be around 0.697 nm long), bases more than 2 nm away from the nanotube lead to changes in the potential smaller than the noise level (flicker noise) in 1X PBS buffer solution. The data in Fig. 7.7a can be represented as a function of distance between the defect and the first target nucleotide and fit with Eqn. 7.1. To simplify this analysis, all of the DNA targets are assumed to have fixed charge despite having varying lengths. This is justified because in 1X PBS buffer solution, only charges within 2 nm of the defect contribute to the potential. It was further assumed that the resistance change in the nanotube is proportional to the change in potential at the defect. This is valid since the simulated potential change is typically between 8 and 15 mV (see Section 7.6), considerably smaller than the thermal voltage. Excellent agreement is found with the measured data with an extracted value of the Debye length of 0.73 nm, slightly larger than the 0.70 nm predicted from Eqn. 7.1.

7.4 Buffer concentration

Fig. 7.8 shows how the RTN amplitude for the 8-mer hybridization target depends on the buffer concentration, which modulates the Debye length of the counterions in solution. Here we use five different buffer concentrations of PBS buffer: 10X, 5X, 1X, 0.4X and 0.1X. Reducing the buffer concentration increases the Debye length, which leads to an increase in the RTN amplitude. At the highest buffer concentration (10X PBS), the target DNA charge is completely screened such that the RTN is below the noise floor. The data in Fig. 7.8 was fitted to Eqn. 7.1 and an average distance between the target DNA charge and the defect of approximately 1.79 nm was extracted. Again, if the assumption is that each DNA is upright and that each base is separated by 0.33 nm with a linker length of 0.697 nm, this yields an expected distance of 1.36 nm. Taking into account the double helix structure of

the DNA molecule, the crystal structure predicts a distance of around 1.8-2.2 nm depending on the orientation of the DNA.

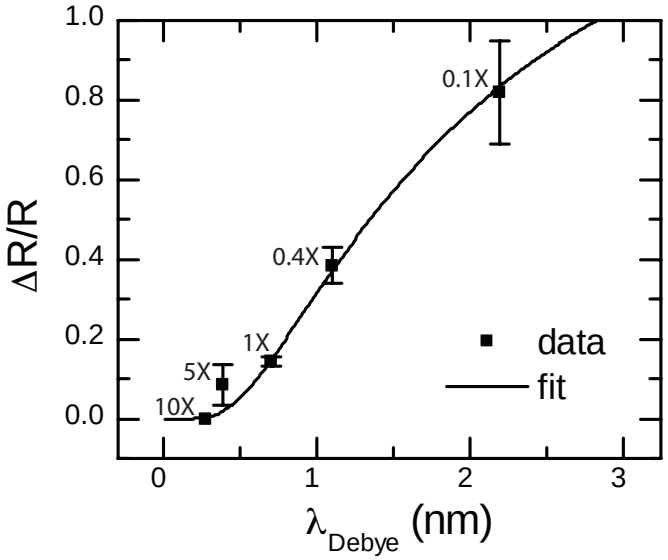

Figure 7.8: Effect of Debye length. Normalized resistance change as a function of buffer concentration. Increasing the buffer concentration will reduce the Debye length so that more of the DNAs negative charge will be screened by counterions. Error bars are calculated from at least 5 different 30 s time interval histograms.

In the previous analyses, the hybridized double-stranded DNA molecule is assumed to be standing upright from the surface. In principle it may actually be at an angle to the surface. In particular, there could be a strong electrostatic interaction between the DNA molecule and the surface of the carbon nanotube such that the potential difference between the liquid and the nanotube will affect the angle of the DNA, similar to previous experiments with DNA on metal electrodes [242,243]. In Fig. 7.9, the effect of the potential difference (V_{Pt}) between the solution and the carbon nanotube on the RTN amplitude was investigated by using the 10-mer DNA target (5′-AACAACTCAC-3′) in 1X PBS.

7.5 Solution potential

As shown in the gate sweep in inset of Fig. 7.9a, the pristine device has a charge neutrality point of around -0.2 V compared to the platinum reference electrode. Biasing the

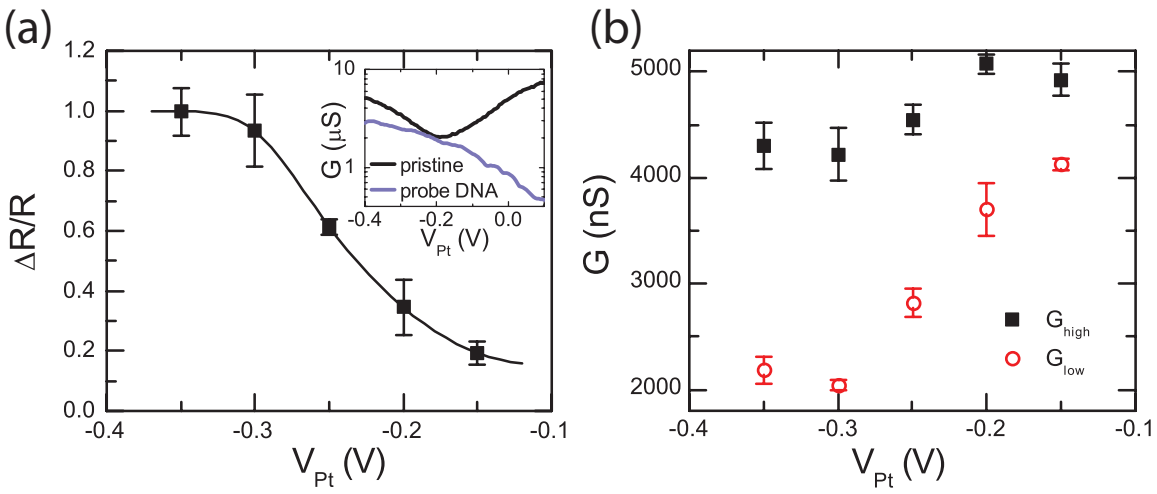

Figure 7.9: (a) RTN amplitude as a normalized resistance change given as a function of electrode potential. The data points are connected by interpolation. Inset shows conductance as a function of solution potential for the pristine device and the functionalize device with probe DNA attached in 1X PBS. The charge neutrality point for the pristine device is around -0.2 V. Error bars are calculated from at least five different 30 s time interval histograms. (b) High and low conductance at different applied on-chip platinum electrode potentials.

carbon nanotube device at a potential higher (lower) than the neutrality point will induce electrons (holes) in the nanotube and cause a repulsive (attractive) electrostatic force with the negatively charged DNA. The inset of Fig. 7.9a also shows the conductance variation with V_{Pt} for the defected device with probe DNA attached. The observed RTN amplitudes are larger than what would be predicted from $\frac{\partial G}{\partial V_{Pt}}\Delta\Phi$ for the probe-attached nanotube by approximately a factor of 50, indicating that the localization of the field effect of the target DNA charge probably results in considerably more modulation of the barrier due to the point-functionalized defect than global gating.

In Fig. 7.9b, both states of the RTN signal were monitored at different potentials as set by the on-chip platinum electrode. The low-conductance state (with the DNA in the duplex state) is much more dependent on the potential compared to the high-conductance state (with probe DNA only). This is consistent with previous studies, which demonstrate that the orientation of surface-immobilized double-stranded DNA is more strongly affected by electric fields because of its long persistence length (50 nm) compared to single stranded DNA (2 nm) [242]. Fig. 7.9a shows that the normalized RTN amplitude (as primarily de-

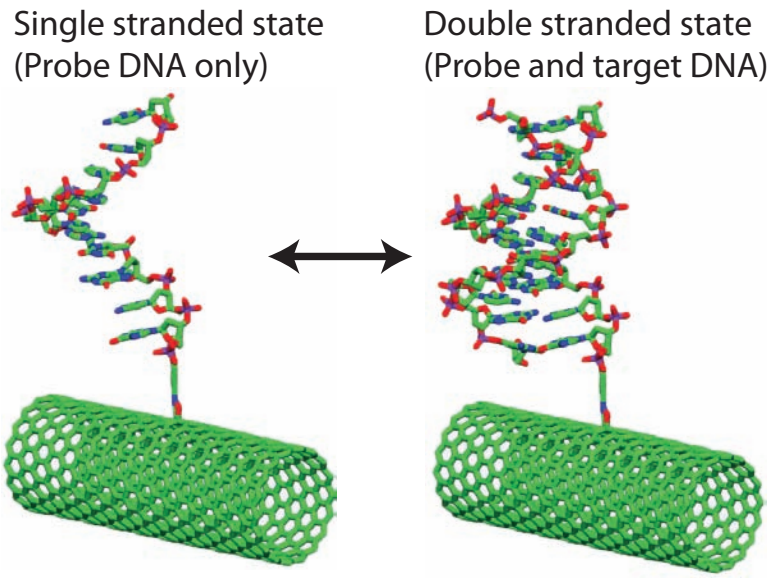

Figure 7.10: Crystal structure representation of DNA attached to the carbon nanotube for both single and double stranded configurations.

termined by the change in the low-conductance state) increases with more negative solution potentials, consistent with DNA that is leaning towards the carbon nanotube and thereby increasing the potential at the nanotube surface (electrostatic simulations are presented in the Supporting Information). The RTN transitions vanish at high potentials ($V_{Pt} \geq$ -0.1 V) indicating that DNA hybridization is inhibited by the negative surface potential.

7.6 Electrostatic simulation

The electrostatics of a DNA molecule tethered to a carbon nanotube is modeled using a nonlinear Poisson-Boltzmann equation for different DNA conformations relative to the nanotube. The crystal structure of a 10-mer DNA (1D68) was obtained through the Protein Data Bank [244] with charge distribution assigned through the PDB2PQR software [245]. For the carbon nanotube, we choose a zigzag (18,0) nanotube with diameter of 1.4 nm. The geometry of the three carbon spacer is estimated using ChemDraw3D (CambridgeSoft, Cambridge, MA). The nonlinear Poisson-Boltzmann equation is solved with the finite-element solver Delphi [246]. The buffer is approximated by a single salt with 0.137 M concentration and an ion radius of 0.2 nm (sodium chloride). Both the linker and carbon nanotube are

assumed to be uncharged for the purpose of the electrostatic simulation, in a manner similar to other simulations [235].

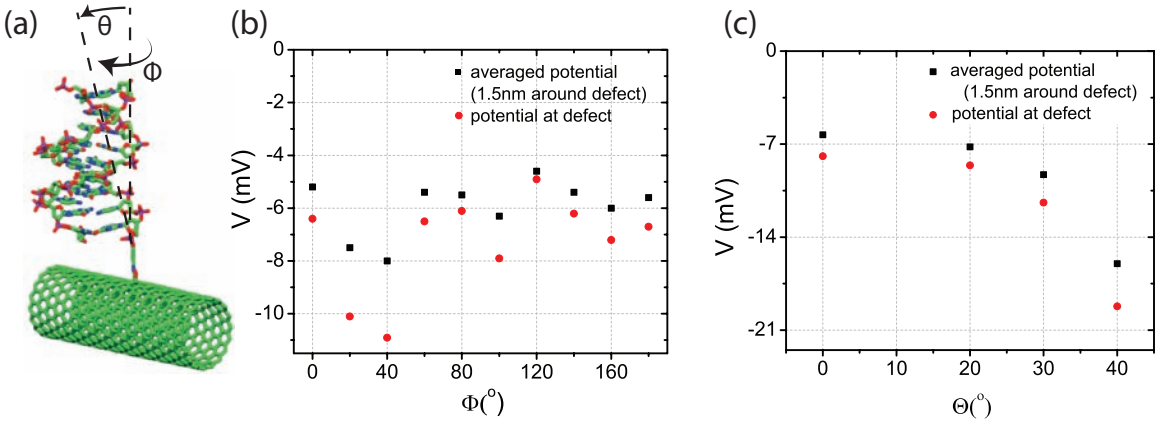

Figure 7.11: (a) The configuration of the DNA molecule can change with respect to the carbon nanotube by a rotational angle Φ and tilt angle θ. (b) Effect of rotational angle Φ on the potential difference on the carbon nanotube surface. (c) Effect of tilt angle θ on the potential difference on the carbon nanotube surface.

The negative charge of the DNA backbone leads to a change in potential at the carbon nanotube. The potential at the carbon nanotube surface has been computed with the single stranded probe attached and the double stranded DNA configurations as shown in Fig. 7.10 and then computed the potential difference between the two states. Because the DNA molecule is subject to Brownian motion, it will undergo fast rotational and translational motion, which will affect the potential at the defect. However, these motions are at times scales (< 0.2 μs) faster than the bandwidth of the current device (~ 100 μs) so the observed potential will be a distribution of all accessible configurations.

In Fig. 7.11b, we have computed the potential difference between the single stranded and double stranded states as a function of the rotation angle Φ. The potential difference is shown both precisely at the point carboxyl defect and as an average around the defect at a radius of 1.5 nm on the carbon nanotube surface (the localization roughly expected from a defect state of a semiconducting carbon nanotube) [181]. Both potentials are relatively rotational invariant since the nanotube has a relatively large diameter.

The potential difference at the surface of the carbon nanotube is plotted as a function of the tilt angle θ in Fig. 7.12 at a rotation angle of Φ =90 °. The defect atom is shown in

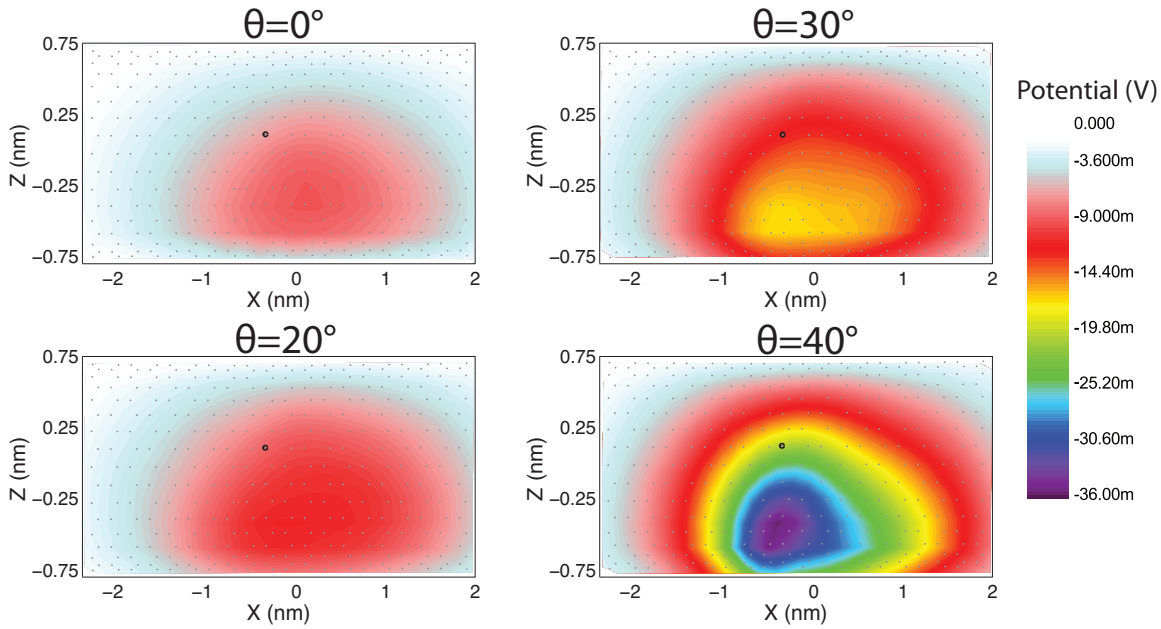

Figure 7.12: Potential difference at the carbon nanotube surface for different tilt angles. The gray points are the nanotube atoms and the black ring is the position of the carboxylic defect.

the center of the figures as a dark ring and the nanotube atoms are shown as grey squares (the X axis is the direction of the length of the nanotube). As the tilt angle increases, the DNA is closer to the surface, which increases the potential difference. The potential at the defect and averaged around the defect are plotted in Fig. 7.11c for the different tilt angles. We attribute the change in the random telegraph noise (RTN) amplitude in Fig. 7.9a to changes in the tilt angle due to electrostatic attraction or repulsion of the molecule with the surface.

7.7 Summary

Experimental results demonstrating the importance of Debye screening for single-molecule field-effect sensors based on carbon nanotubes have been presented. The amplitude of RTN fluctuations characterizing single-molecule interactions increases by moving charges closer to the defect or by decreasing the buffer concentration, as supported by simple screening arguments. The results presented here are not only significant to basic scientific research

but also important to understand potential applications of these devices as a single-molecule label free sensing platform.

Chapter 8

Conclusion

8.1 Summary of this work

This thesis describes the design of a single molecule sensor based on a carbon nanotube field-effect transistor. The motivation behind this work is that a purely electronic sensing platform can potentially detect biomolecular systems with very fast dynamics. The sensor has been validated by a proof of principle biological system based on DNA hybridization. Temperature dependent fluctuations lead to extraction of thermodynamics and kinetics that agree with previous hybridization experiments using optical techniques. Studies on the buffer concentration, charge proximity and solution potential dependence of the fluctuation amplitude were consistent with a simple Debye screening model. This work has lead to the following peer reviewed publications:

- S. Sorgenfrei, C.-Y. Chiu, R.L. Gonzalez, Y.-J. Yu, P. Kim, C. Nuckolls,and K.L. Shepard,"Label-free single-molecule detection of DNA hybridization kinetics with a carbon nanotube transitor," *Nature Nanotechnology*, vol.6, pp.126-132, February 2011.

- S. Sorgenfrei, C.-Y. Chiu, M. Johnston, C. Nuckolls,and K.L. Shepard,"Debye screening in single-molecule carbon nanotube field-effect sensors," *Nano Letters*, Advanced Online Publication.

- S. Sorgenfrei, I. Meric, S. Banerjee, A. Akey, S. Rosenblatt, I.P. Herman, K.L. Shep-

ard,"Controlled dielectrophoretic assembly of carbon nanotubes using real time electrical detection," *Applied Physics Letters*, vol.94, 053105, February 2009.

- S. Sorgenfrei, K.L. Shepard,"Single-molecule electronic detection using nanoscale field-effect devices," *Design and Automation Conference (DAC) (invited paper)*, June 2011.

- S. Sorgenfrei, C.-Y. Chiu, C. Nuckolls,and K.L. Shepard,"Ultra-sensitive carbon nanotubes for single-molecule detection of DNA hybridization kinetics using conductance-based correlation spectroscopy," *Proc. of 16th International Conference on Solid-State Sensors, Actuators and Microsystems (Transducers '11)*, June 2011.

- S. Sorgenfrei, C.-Y. Chiu, C. Nuckolls,and K.L. Shepard,"Charge sensing using point-functionalized carbon-nanotube transistors for single-molecule detection," *Proc. of IEEE/NIH Life Science Systems and Applications Workshop (LiSSA)*, April 2011

- J. Rosenstein, S. Sorgenfrei, K.L. Shepard,"Noise and Bandwidth Performance of Single-Molecule Biosensors," *IEEE Custom Integrated Circuits Conference (CICC) accepted*, September 2011.

8.2 Future work

There are multiple topics in this thesis tha I would have liked to improve and address but did not have enough "bandwidth" to do it. One idea is to integrate the carbon nanotube sensors on a CMOS substrate with active circuitry such as low noise amplifiers and data converters (ADCs and DACs). This is both interesting and challenging from a circuit design perspective since it involves designing measurement circuits for currents as low as picoamps up to several microamps and a wide bandwidth from DC to possibly over 1 MHz. Another challenge is to actually integrate the carbon nanotubes on a commercial chip from a foundry that usually uses it for microprocessors and communication chips so a lot of post processing of the chip surface and interconnect is necessary. From a biological and biosensor perspective, a big advantage is that the chip could enable multiplexed measurement of

many devices in parallel. The chip could also be used to map out where the nanotubes are assembled on the surface and measure device to device variability on an array of 1 million devices. Also, the bandwidth of the measurement could be drastically reduced since the electrode size are shrunk down to possibly only 10×10 μm^2 so that C_p is reduced by over two orders of magnitude (while also reducing R_p at the same time), therefore pushing out the corner frequency to above 1MHz.

Currently, one of the main limitations in the carbon nanotube sensor is the large flicker noise. Studies on suspended carbon nanotubes have shown that the flicker noise can be decreased by almost an order of magnitude by suspending the nanotube, thereby reducing the effects of oxide traps [247]. Recently, we showed that boron nitride is a superior dielectric for graphene devices because it is both flatter and has less charge traps [248]. By growing carbon nanotubes on boron nitride, I would like to study if the flicker noise can also be reduced which would directly improve the SNR ratio for the sensor.

The yield of the electrochemical oxidation is about 10% and I would like to work on alternative methods to create a point defect. One method is to lithographically define a very small channel ($\sim$5 nm) and lightly etch the nanotube in a oxygen plasma, creating a defect but not cutting the nanotube. This would be more of a top down approach and many devices could be etched simultaneously. Another method I would like to investigate is using an afm tip with a water meniscus and applying a very short pulse (a few nanoseconds) to the tip in contact mode over the nanotube while measuring the nanotube conductance. These short pulses should improve the spatial resolution over previous studies with pulses around 1 ms [189].

While it is tempting to try to investigate biomolecular kinetics of more interesting biomolecules such as proteins, it is also much more difficult to interpret the data due to the complex electrostatic distribution. Instead, I would like to study DNA based systems such

as a DNA hairpin of different sequences and hairpin lengths, which should follow directly the experiments outlined in this thesis. If hairpin dynamics can be seen, the next step would be to try to incorporate new bases into the hairpin, similar to previous optical sequence-by-synthesis (SBS) approaches. Due to Debye length screening, a new incorporated base is closer to the nanotube so that the fluctuation amplitude increases, which could be detected by the sensor.

8.3 Other contributions

In addition to the work described in this thesis, I have also worked on other projects with several collaborators:

- I worked on a CMOS chip for fluorescent detection. Having measured the previously designed chip, I was able to improve the photodiode detector and redesign the chip. By incorporating a differential photodiode, the effects of long time constants due to carrier diffusion in the substrate could be successfully reduced. This lead to the following publications:

  - T.D. Huang, S. Sorgenfrei, P. Gong, K.L. Shepard,"A CMOS array sensor for sub-800-ps time-resolved fluorescence detection," *Proceedings of the IEEE 2007 Custom Integrated Circuits Conference (CICC)*, September 2007.
  - T.D. Huang, S. Sorgenfrei, P. Gong, K.L. Shepard,"A 0.18μm CMOS Array Sensor for Integrated Time-Resolved Fluorescence Detection," *IEEE Journal of Solid-State Circuits*, vol.44, pp.1644-1654, May 2009.

- Being interested in transfering carbon nanotubes and graphene to arbitrary substrates (such as a CMOS chip), I started working on transfer techniques. At the time, dielectrics made from boron nitride looked promising to improve the mobility of graphene devices so a method to reliably transfer a small flake of graphene onto a small flake of boron nitride on a different substrate was conceived. This lead to the following publication:

– C.R. Dean, A.F. Young, I. Meric, C. Lee, L. Wang, S. Sorgenfrei, K. Watanabe, T. Taniguchi, P. Kim, K.L. Shepard, and J. Hone,"Boron nitride substrates for high quality graphene electronics," *Nature Nanotechnology*, vol.5, pp.722-726, August 2010.

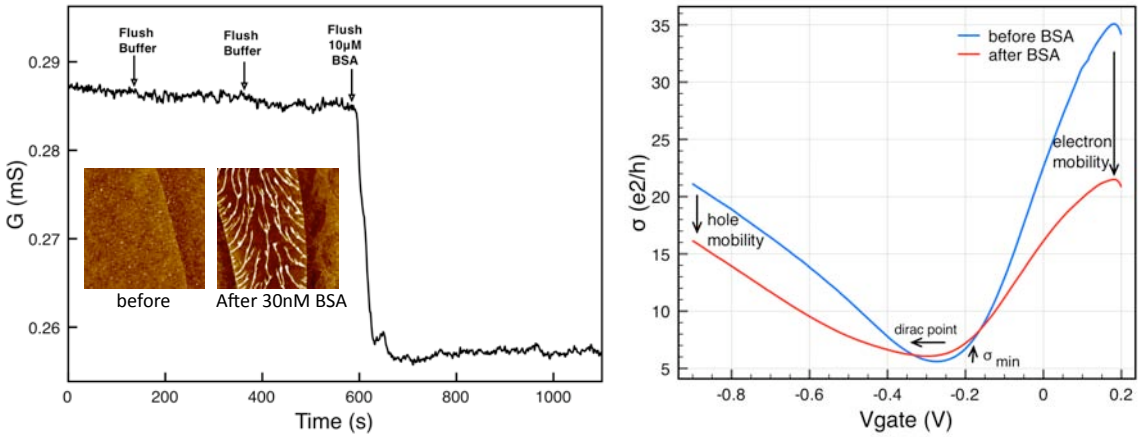

Figure 8.1: Graphene for ensemble protein detection. (a) Real time detection of 10 μM BSA in 1X PBS buffer. The ainset on the left shows an AFM image of the annealed device before the experiment and the inset on the right shows the graphene covered by protein. (b) As shown in the before and after electrolyte gate sweep of the graphene device, the mobility of the graphene decreases and the Dirac point shifts to the left as expected from similar experiments with carbon nanotubes.

- After working on carbon nanotubes for ensemble biosensors, I started to think about using graphene as a sensor. The advantages of graphene are that it has a much larger surface area compared to carbon nanotubes and using the recently established CVD growth technique, can be fabricated in a more top down approach, creating arrays of devices easily. Another advantage is that it is an ideal 2D electron system so that mobilities, carrier densities and capacitances can be easily measured. This should provide a better understanding of the physical mechanism in bulk sensing and differentiate the different sensing mechanism, which is not possible with nanotubes.

  Initial experiments using graphene showed interesting results but there was a lot of variability and the sensitivities were not very high as shown in the real time plot in Fig. 8.1a. By using a four probe measurement, we were able to take out effects

of the contact resistance and show changes in the mobility and resistance maximum (Dirac point) in Fig. 8.1b. Also, similar to ensemble sensing with carbon nanotubes, it is difficult to add specificity to the sensor because covalent attachement destroys the electronic transport properties and significantly reduces carrier mobility towards graphene oxide.

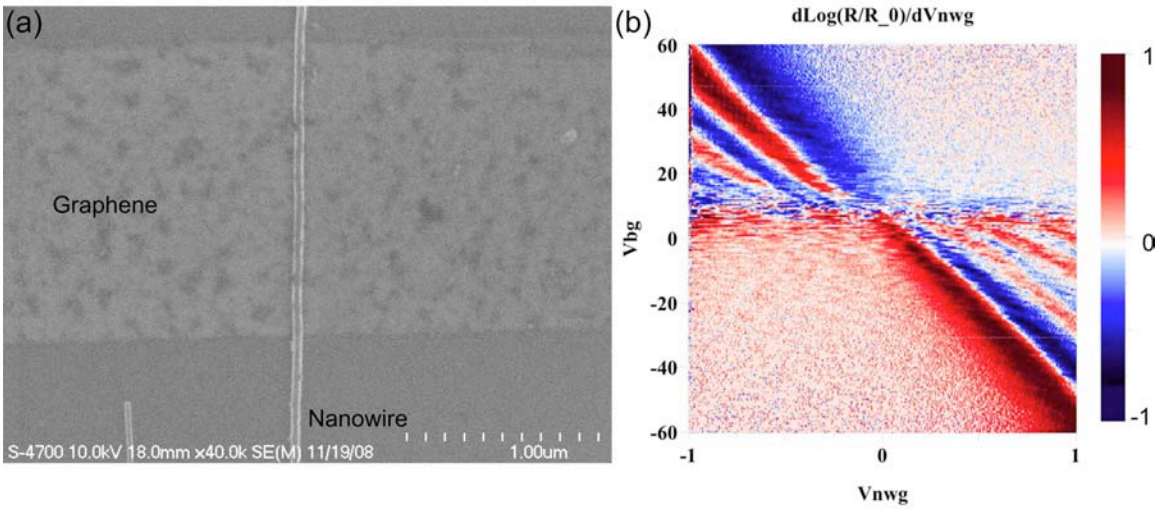

Figure 8.2: DEP aligned nanowire over graphene shown in the SEM image in (a). (b) shows quantum oscillations due to the sharp potential from the silicon nanowire. This measurement was performed by Andrea Young from Prof. Kims group.

- I have also used dielectrophoresis to align a silicon nanowire with an electrode to use it as a very small and well defined gate for studies on quantum tunneling in graphene [249] as shown in Fig. 8.2a. Compared to the previously used hafnium oxide top gate, nanowires do not degrade the quality of the graphene through processing and the thin native oxide and small dimensions result in a very sharp potential profile and large quantum interference effects (Fig. 8.2b. Another project involved the measurement of gate capacitance to graphene. Similar to carbon nanotubes, the density of states are proportional to the quantum capacitance so the capacitance is a direct way to extract carrier densities.

  – A.F. Young, C.R. Dean, I. Meric, S. Sorgenfrei, H. Ren, K. Watanabe, T. Taniguchi, J. Hone, K.L. Shepard, and P. Kim,"Eletronic compressibility of

gapped bilayer graphene," *arXiv:1004.556v1*, 2010.

- Another project involved the electrochemically oxidation of a graphene device while measuring its conductance. The conductance in graphene is even more reversible over many cycles of oxidation as shown in Fig. 8.3. This is in fact direct evidence that electrochemical oxidation can affect many atoms and a very careful conductance control during the oxidation is necessary to ensure that the device is not insulating for the case of carbon nanotubes.

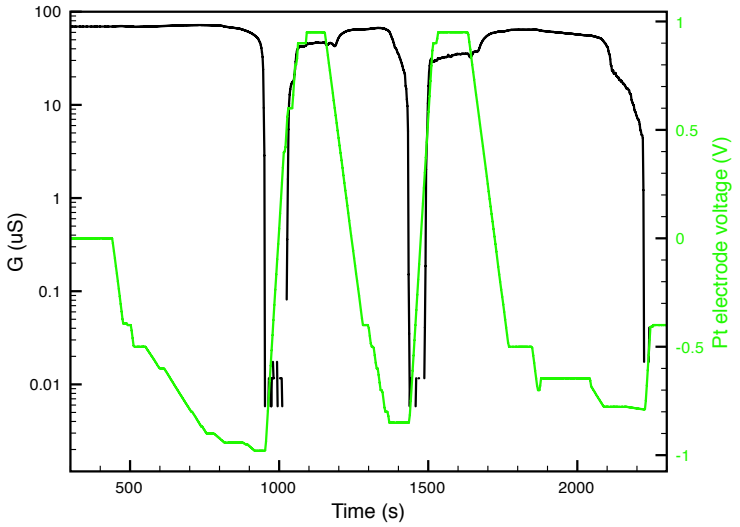

Figure 8.3: Electrochemical oxidation of graphene.

Bibliography

[1] J. S. Kilby, "Invention of integrated-circuit," *Ieee Transactions on Electron Devices*, vol. 23, no. 7, pp. 648–654, 1976.

[2] J. D. Watson and F. H. C. Crick, "Genetical implications of the structure of deoxyribonucleic acid," *Nature*, vol. 171, no. 4361, pp. 964–967, 1953.

[3] B. Alberts, *Molecular biology of the cell*, 4th ed. New York: Garland Science, 2002.

[4] R. Austin, "Nanopores - the art of sucking spaghetti," *Nature Materials*, vol. 2, no. 9, pp. 567–568, 2003.

[5] V. A. Bloomfield, D. M. Crothers, and I. Tinoco, *Nucleic acids : structures, properties, and functions*. Sausalito, Calif.: University Science Books, 2000.

[6] J. Shendure, R. D. Mitra, C. Varma, and G. M. Church, "Advanced sequencing technologies: methods and goals," *Nat Rev Genet*, vol. 5, no. 5, pp. 335–44, 2004.

[7] A. Ureta-Vidal, L. Ettwiller, and E. Birney, "Comparative genomics: genome-wide analysis in metazoan eukaryotes," *Nat Rev Genet*, vol. 4, no. 4, pp. 251–62, 2003.

[8] N. A. Holtzman and T. M. Marteau, "Will genetics revolutionize medicine?" *N Engl J Med*, vol. 343, no. 2, pp. 141–4, 2000.

[9] H. Rajagopalan, M. A. Nowak, B. Vogelstein, and C. Lengauer, "The significance of unstable chromosomes in colorectal cancer," *Nat Rev Cancer*, vol. 3, no. 9, pp. 695–701, 2003.

[10] E. Pennisi, "Disease risk links to gene regulation," *Science*, vol. 332, no. 6033, pp. 1031–1031, 2011.

[11] L. H. Grouse, P. J. Munson, and P. S. Nelson, "Sequence databases and microarrays as tools for identifying prostate cancer biomarkers," *Urology*, vol. 57, no. 4, 2001.

[12] C. Debouck and P. N. Goodfellow, "Dna microarrays in drug discovery and development," *Nat Genet*, vol. 21, no. 1, 1999.

[13] F. Sanger, S. Nicklen, and A. R. Coulson, "Dna sequencing with chain-terminating inhibitors," *Proc Natl Acad Sci U S A*, vol. 74, no. 12, pp. 5463–7, 1977.

[14] L. M. Smith, J. Z. Sanders, R. J. Kaiser, P. Hughes, C. Dodd, C. R. Connell, C. Heiner, S. B. Kent, and L. E. Hood, "Fluorescence detection in automated dna sequence analysis," *Nature*, vol. 321, no. 6071, pp. 674–9, 1986.

[15] R. Drmanac *et al.*, "Dna sequencing by hybridization with arrays of samples or probes," *Methods Mol Biol*, vol. 170, pp. 173–9, 2001.

[16] J. Ju *et al.*, "Four-color dna sequencing by synthesis using cleavable fluorescent nucleotide reversible terminators," *Proc Natl Acad Sci U S A*, vol. 103, no. 52, pp. 19 635–40, 2006.

[17] J. Guo *et al.*, "Four-color dna sequencing with 3'-o-modified nucleotide reversible terminators and chemically cleavable fluorescent dideoxynucleotides," *Proc Natl Acad Sci U S A*, vol. 105, no. 27, pp. 9145–50, 2008.

[18] B. Gharizadeh, T. Nordstrom, A. Ahmadian, M. Ronaghi, and P. Nyren, "Long-read pyrosequencing using pure 2'-deoxyadenosine-5'-o'-(1-thiotriphosphate) sp-isomer," *Anal Biochem*, vol. 301, no. 1, pp. 82–90, 2002.

[19] W. C. Timmer and J. M. Villalobos, "The polymerase chain-reaction," *Journal of Chemical Education*, vol. 70, no. 4, pp. 273–280, 1993.

[20] S. R. Mickelsen, "Electrochemical biosensors for dna sequence detection," *Electroanalysis*, vol. 8, no. 1, pp. 15–19, 1996.

[21] M. L. Metzker, "Applications of next-generation sequencing sequencing technologies - the next generation," *Nature Reviews Genetics*, vol. 11, no. 1, pp. 31–46, 2010.

[22] C. S. S. R. Kumar, J. Hormes, and C. Leuschner, *Nanofabrication towards biomedical applications : techniques, tools, applications, and impact*. Weinheim: Wiley-VCH, 2005.

[23] A. A. Deniz, S. Mukhopadhyay, and E. A. Lemke, "Single-molecule biophysics: at the interface of biology, physics and chemistry," *Journal of the Royal Society Interface*, vol. 5, no. 18, pp. 15–45, 2008.

[24] P. Hinterdorfer and A. van Oijen, "Handbook of single-molecule biophysics," 2009, full text available from SpringerLink ebooks.

[25] R. Sarpeshkar, T. Delbruck, and C. A. Mead, "White noise in mos transistors and resistors," *Ieee Circuits and Devices Magazine*, vol. 9, no. 6, pp. 23–29, 1993.

[26] J. R. Lakowicz, *Principles of fluorescence spectroscopy*, 3rd ed. New York: Springer, 2006.

[27] M. J. Rust, M. Bates, and X. Zhuang, "Sub-diffraction-limit imaging by stochastic optical reconstruction microscopy (storm)," *Nat Methods*, vol. 3, no. 10, pp. 793–5, 2006.

[28] S. R. Pavani, M. A. Thompson, J. S. Biteen, S. J. Lord, N. Liu, R. J. Twieg, R. Piestun, and W. E. Moerner, "Three-dimensional, single-molecule fluorescence imaging beyond the diffraction limit by using a double-helix point spread function," *Proc Natl Acad Sci U S A*, vol. 106, no. 9, pp. 2995–9, 2009.

[29] T. T. Perkins, D. E. Smith, and S. Chu, "Direct observation of tube-like motion of a single polymer chain," *Science*, vol. 264, no. 5160, pp. 819–22, 1994.

[30] Y. M. Wang, R. H. Austin, and E. C. Cox, "Single molecule measurements of repressor protein 1d diffusion on dna," *Physical Review Letters*, vol. 97, no. 4, 2006.

[31] A. Yildiz, J. N. Forkey, S. A. McKinney, T. Ha, Y. E. Goldman, and P. R. Selvin, "Myosin v walks hand-over-hand: single fluorophore imaging with 1.5-nm localization," *Science*, vol. 300, no. 5628, pp. 2061–5, 2003.

[32] K. Adachi, R. Yasuda, H. Noji, H. Itoh, Y. Harada, M. Yoshida, and J. Kinosita, K., "Stepping rotation of f1-atpase visualized through angle-resolved single-fluorophore imaging," *Proc Natl Acad Sci U S A*, vol. 97, no. 13, pp. 7243–7, 2000.

[33] T. Ha, T. Enderle, D. F. Ogletree, D. S. Chemla, P. R. Selvin, and S. Weiss, "Probing the interaction between two single molecules: fluorescence resonance energy transfer between a single donor and a single acceptor," *Proc Natl Acad Sci U S A*, vol. 93, no. 13, pp. 6264–8, 1996.

[34] C. Joo, H. Balci, Y. Ishitsuka, C. Buranachai, and T. Ha, "Advances in single-molecule fluorescence methods for molecular biology," *Annual Review of Biochemistry*, vol. 77, pp. 51–76, 2008.

[35] T. Ha, I. Rasnik, W. Cheng, H. P. Babcock, G. H. Gauss, T. M. Lohman, and S. Chu, "Initiation and re-initiation of dna unwinding by the escherichia coli rep helicase," *Nature*, vol. 419, no. 6907, pp. 638–41, 2002.

[36] S. Myong, I. Rasnik, C. Joo, T. M. Lohman, and T. Ha, "Repetitive shuttling of a motor protein on dna," *Nature*, vol. 437, no. 7063, pp. 1321–5, 2005.

[37] L. Bai, T. J. Santangelo, and M. D. Wang, "Single-molecule analysis of rna polymerase transcription," *Annu Rev Biophys Biomol Struct*, vol. 35, pp. 343–60, 2006.

[38] J. Fei, P. Kosuri, D. D. MacDougall, and J. Gonzalez, R. L., "Coupling of ribosomal l1 stalk and trna dynamics during translation elongation," *Mol Cell*, vol. 30, no. 3, pp. 348–59, 2008.

[39] A. A. Deniz, T. A. Laurence, G. S. Beligere, M. Dahan, A. B. Martin, D. S. Chemla, P. E. Dawson, P. G. Schultz, and S. Weiss, "Single-molecule protein folding: diffusion fluorescence resonance energy transfer studies of the denaturation of chymotrypsin inhibitor 2," *Proc Natl Acad Sci U S A*, vol. 97, no. 10, pp. 5179–84, 2000.

[40] S. Hohng, C. Joo, and T. Ha, "Single-molecule three-color fret," *Biophys J*, vol. 87, no. 2, pp. 1328–37, 2004.

[41] Z. Petrasek and P. Schwille, "Precise measurement of diffusion coefficients using scanning fluorescence correlation spectroscopy," *Biophys J*, vol. 94, no. 4, pp. 1437–48, 2008.

[42] S. A. Kim, K. G. Heinze, and P. Schwille, "Fluorescence correlation spectroscopy in living cells," *Nat Methods*, vol. 4, no. 11, pp. 963–73, 2007.

[43] G. Bonnet, O. Krichevsky, and A. Libchaber, "Kinetics of conformational fluctuations in dna hairpin-loops," *Proceedings of the National Academy of Sciences of the United States of America*, vol. 95, no. 15, pp. 8602–8606, 1998.

[44] M. I. Wallace, L. Ying, S. Balasubramanian, and D. Klenerman, "Non-arrhenius kinetics for the loop closure of a dna hairpin," *Proc Natl Acad Sci U S A*, vol. 98, no. 10, pp. 5584–9, 2001.

[45] H. T. Li, X. J. Ren, L. M. Ying, S. Balasubramanian, and D. Klenerman, "Measuring single-molecule nucleic acid dynamics in solution by two-color filtered ratiometric fluorescence correlation spectroscopy," *Proceedings of the National Academy of Sciences of the United States of America*, vol. 101, no. 40, pp. 14 425–14 430, 2004.

[46] K. C. Neuman and A. Nagy, "Single-molecule force spectroscopy: optical tweezers, magnetic tweezers and atomic force microscopy," *Nat Methods*, vol. 5, no. 6, pp. 491–505, 2008.

[47] H. Li, S. H. Park, J. H. Reif, T. H. LaBean, and H. Yan, "Dna-templated self-assembly of protein and nanoparticle linear arrays," *J Am Chem Soc*, vol. 126, no. 2, pp. 418–9, 2004.

[48] S. Scheuring and J. N. Sturgis, "Dynamics and diffusion in photosynthetic membranes from rhodospirillum photometricum," *Biophys J*, vol. 91, no. 10, pp. 3707–17, 2006.

[49] P. W. K. Rothemund, "Folding dna to create nanoscale shapes and patterns," *Nature*, vol. 440, no. 7082, pp. 297–302, 2006.

[50] M. Grandbois, M. Beyer, M. Rief, H. Clausen-Schaumann, and H. E. Gaub, "How strong is a covalent bond?" *Science*, vol. 283, no. 5408, pp. 1727–1730, 1999.

[51] A. F. Oberhauser, P. E. Marszalek, H. P. Erickson, and J. M. Fernandez, "The molecular elasticity of the extracellular matrix protein tenascin," *Nature*, vol. 393, no. 6681, pp. 181–185, 1998.

[52] G. U. Lee, L. A. Chrisey, and R. J. Colton, "Direct measurement of the forces between complementary strands of dna," *Science*, vol. 266, no. 5186, pp. 771–773, 1994.

[53] K. C. Neuman, E. H. Chadd, G. F. Liou, K. Bergman, and S. M. Block, "Characterization of photodamage to escherichia coli in optical traps," *Biophys J*, vol. 77, no. 5, pp. 2856–63, 1999.

[54] D. P. Cherney, T. E. Bridges, and J. M. Harris, "Optical trapping of unilamellar phospholipid vesicles: investigation of the effect of optical forces on the lipid membrane shape by confocal-raman microscopy," *Anal Chem*, vol. 76, no. 17, pp. 4920–8, 2004.

[55] S. B. Smith, Y. Cui, and C. Bustamante, "Overstretching b-dna: the elastic response of individual double-stranded and single-stranded dna molecules," *Science*, vol. 271, no. 5250, pp. 795–9, 1996.

[56] M. D. Wang, H. Yin, R. Landick, J. Gelles, and S. M. Block, "Stretching dna with optical tweezers," *Biophys J*, vol. 72, no. 3, pp. 1335–46, 1997.

[57] M. D. Wang, M. J. Schnitzer, H. Yin, R. Landick, J. Gelles, and S. M. Block, "Force and velocity measured for single molecules of rna polymerase," *Science*, vol. 282, no. 5390, pp. 902–7, 1998.

[58] W. J. Greenleaf, K. L. Frieda, D. A. Foster, M. T. Woodside, and S. M. Block, "Direct observation of hierarchical folding in single riboswitch aptamers," *Science*, vol. 319, no. 5863, pp. 630–3, 2008.

[59] J. Liphardt, B. Onoa, S. B. Smith, J. Tinoco, I., and C. Bustamante, "Reversible unfolding of single rna molecules by mechanical force," *Science*, vol. 292, no. 5517, pp. 733–7, 2001.

[60] T. Strick, J. Allemand, V. Croquette, and D. Bensimon, "Twisting and stretching single dna molecules," *Prog Biophys Mol Biol*, vol. 74, no. 1, 2000.

[61] J. K. Fisher *et al.*, "Thin-foil magnetic force system for high-numerical-aperture microscopy," *Rev Sci Instrum*, vol. 77, no. 2, p. nihms8302, 2006.

[62] A. R. Bausch, W. Moller, and E. Sackmann, "Measurement of local viscoelasticity and forces in living cells by magnetic tweezers," *Biophys J*, vol. 76, no. 1, 1999.

[63] G. Binnig, H. Rohrer, C. Gerber, and E. Weibel, "7x7 reconstruction on si(111) resolved in real space," *Physical Review Letters*, vol. 50, no. 2, pp. 120–123, 1983.

[64] T. W. Odom, J. L. Huang, P. Kim, and C. M. Lieber, "Atomic structure and electronic properties of single-walled carbon nanotubes," *Nature*, vol. 391, no. 6662, pp. 62–64, 1998.

[65] J. W. G. Wildoer, L. C. Venema, A. G. Rinzler, R. E. Smalley, and C. Dekker, "Electronic structure of atomically resolved carbon nanotubes," *Nature*, vol. 391, no. 6662, pp. 59–62, 1998.

[66] E. Shapir, H. Cohen, A. Calzolari, C. Cavazzoni, D. A. Ryndyk, G. Cuniberti, A. Kotlyar, R. Di Felice, and D. Porath, "Electronic structure of single dna molecules resolved by transverse scanning tunnelling spectroscopy," *Nature Materials*, vol. 7, no. 1, pp. 68–74, 2008.

[67] D. M. Eigler and E. K. Schweizer, "Positioning single atoms with a scanning tunneling microscope," *Nature*, vol. 344, no. 6266, pp. 524–526, 1990.

[68] M. F. Crommie, C. P. Lutz, and D. M. Eigler, "Confinement of electrons to quantum corrals on a metal surface," *Science*, vol. 262, no. 5131, pp. 218–20, 1993.

[69] M. Taniguchi, M. Tsutsui, K. Shoji, and T. Kawai, "Formation and self-breaking mechanism of stable atom-sized junctions," *Nano Letters*, vol. 8, no. 1, pp. 345–349, 2008.

[70] H. Park, A. K. L. Lim, A. P. Alivisatos, J. Park, and P. L. McEuen, "Fabrication of metallic electrodes with nanometer separation by electromigration," *Applied Physics Letters*, vol. 75, no. 2, pp. 301–303, 1999.

[71] X. Guo *et al.*, "Covalently bridging gaps in single-walled carbon nanotubes with conducting molecules," *Science*, vol. 311, no. 5759, pp. 356–9, 2006.

[72] L. Venkataraman, J. E. Klare, C. Nuckolls, M. S. Hybertsen, and M. L. Steigerwald, "Dependence of single-molecule junction conductance on molecular conformation," *Nature*, vol. 442, no. 7105, pp. 904–907, 2006.

[73] M. Taniguchi, M. Tsutsui, K. Yokota, and T. Kawai, "Identifying single nucleotides by tunnelling current," *Nature Nanotechnology*, vol. 5, no. 4, pp. 286–290, 2010.

[74] S. Huang, J. He, S. A. Chang, P. M. Zhang, F. Liang, S. Q. Li, M. Tuchband, A. Fuhrmann, R. Ros, and S. Lindsay, "Identifying single bases in a dna oligomer with electron tunnelling," *Nature Nanotechnology*, vol. 5, no. 12, pp. 868–873, 2010.

[75] S. Lindsay, S. A. Chang, S. Huang, J. He, F. Liang, P. M. Zhang, S. Q. Li, X. Chen, and O. Sankey, "Electronic signatures of all four dna nucleosides in a tunneling gap," *Nano Letters*, vol. 10, no. 3, pp. 1070–1075, 2010.

[76] D. Branton *et al.*, "The potential and challenges of nanopore sequencing," *Nature Biotechnology*, vol. 26, no. 10, pp. 1146–1153, 2008.

[77] J. J. Kasianowicz, E. Brandin, D. Branton, and D. W. Deamer, "Characterization of individual polynucleotide molecules using a membrane channel," *Proc Natl Acad Sci U S A*, vol. 93, no. 24, pp. 13 770–3, 1996.

[78] I. Szabo, G. Bathori, F. Tombola, M. Brini, A. Coppola, and M. Zoratti, "Dna translocation across planar bilayers containing bacillus subtilis ion channels," *J Biol Chem*, vol. 272, no. 40, pp. 25 275–82, 1997.

[79] J. Li, D. Stein, C. McMullan, D. Branton, M. J. Aziz, and J. A. Golovchenko, "Ion-beam sculpting at nanometre length scales," *Nature*, vol. 412, no. 6843, pp. 166–9, 2001.

[80] A. J. Storm, J. H. Chen, X. S. Ling, H. W. Zandbergen, and C. Dekker, "Fabrication of solid-state nanopores with single-nanometre precision," *Nature Materials*, vol. 2, no. 8, pp. 537–40, 2003.

[81] R. M. Smeets, U. F. Keyser, D. Krapf, M. Y. Wu, N. H. Dekker, and C. Dekker, "Salt dependence of ion transport and dna translocation through solid-state nanopores," *Nano Lett*, vol. 6, no. 1, pp. 89–95, 2006.

[82] M. Wanunu, T. Dadosh, V. Ray, J. M. Jin, L. McReynolds, and M. Drndic, "Rapid electronic detection of probe-specific micrornas using thin nanopore sensors," *Nature Nanotechnology*, vol. 5, no. 11, pp. 807–814, 2010.

[83] A. Meller, L. Nivon, E. Brandin, J. Golovchenko, and D. Branton, "Rapid nanopore discrimination between single polynucleotide molecules," *Proc Natl Acad Sci U S A*, vol. 97, no. 3, pp. 1079–84, 2000.

[84] D. Fologea, J. Uplinger, B. Thomas, D. S. McNabb, and J. Li, "Slowing dna translocation in a solid-state nanopore," *Nano Lett*, vol. 5, no. 9, pp. 1734–7, 2005.

[85] J. B. Heng, C. Ho, T. Kim, R. Timp, A. Aksimentiev, Y. V. Grinkova, S. Sligar, K. Schulten, and G. Timp, "Sizing dna using a nanometer-diameter pore," *Biophys J*, vol. 87, no. 4, pp. 2905–11, 2004.

[86] P. Bergveld, "Development, operation, and application of the ion-sensitive field-effect transistor as a tool for electrophysiology," *IEEE Trans Biomed Eng*, vol. 19, no. 5, pp. 342–51, 1972.

[87] E. Stern, J. F. Klemic, D. A. Routenberg, P. N. Wyrembak, D. B. Turner-Evans, A. D. Hamilton, D. A. LaVan, T. M. Fahmy, and M. A. Reed, "Label-free immunodetection with cmos-compatible semiconducting nanowires," *Nature*, vol. 445, no. 7127, pp. 519–22, 2007.

[88] G. Zheng, F. Patolsky, Y. Cui, W. U. Wang, and C. M. Lieber, "Multiplexed electrical detection of cancer markers with nanowire sensor arrays," *Nat Biotechnol*, vol. 23, no. 10, pp. 1294–301, 2005.

[89] J. Hahm and C. M. Lieber, "Direct ultrasensitive electrical detection of dna and dna sequence variations using nanowire nanosensors," *Nano Letters*, vol. 4, no. 1, pp. 51–54, 2004.

[90] F. Patolsky, G. F. Zheng, O. Hayden, M. Lakadamyali, X. W. Zhuang, and C. M. Lieber, "Electrical detection of single viruses," *Proceedings of the National Academy of Sciences of the United States of America*, vol. 101, no. 39, pp. 14 017–14 022, 2004.

[91] S. Purushothaman, C. Toumazou, and C. P. Ou, "Protons and single nucleotide polymorphism detection: A simple use for the ion sensitive field effect transistor," *Sensors and Actuators B-Chemical*, vol. 114, no. 2, pp. 964–968, 2006.

[92] K. Bradley, M. Briman, A. Star, and G. Gruner, "Charge transfer from adsorbed proteins," *Nano Letters*, vol. 4, no. 2, pp. 253–256, 2004.

[93] E. D. Minot, A. M. Janssens, I. Heller, H. A. Heering, C. Dekker, and S. G. Lemay, "Carbon nanotube biosensors: The critical role of the reference electrode," *Applied Physics Letters*, vol. 91, no. 9, pp. –, 2007.

[94] B. L. Allen, P. D. Kichambare, and A. Star, "Carbon nanotube field-effect-transistor-based biosensors," *Advanced Materials*, vol. 19, no. 11, pp. 1439–1451, 2007.

[95] A. Star, E. Tu, J. Niemann, J. C. P. Gabriel, C. S. Joiner, and C. Valcke, "Label-free detection of dna hybridization using carbon nanotube network field-effect transistors," *Proceedings of the National Academy of Sciences of the United States of America*, vol. 103, no. 4, pp. 921–926, 2006.

[96] R. J. Chen, Y. G. Zhang, D. W. Wang, and H. J. Dai, "Noncovalent sidewall functionalization of single-walled carbon nanotubes for protein immobilization," *Journal of the American Chemical Society*, vol. 123, no. 16, pp. 3838–3839, 2001.

[97] R. J. Chen, S. Bangsaruntip, K. A. Drouvalakis, N. W. S. Kam, M. Shim, Y. M. Li, W. Kim, P. J. Utz, and H. J. Dai, "Noncovalent functionalization of carbon nanotubes for highly specific electronic biosensors," *Proceedings of the National Academy of Sciences of the United States of America*, vol. 100, no. 9, pp. 4984–4989, 2003.

[98] N. W. S. Kam and H. J. Dai, "Carbon nanotubes as intracellular protein transporters: Generality and biological functionality," *Journal of the American Chemical Society*, vol. 127, no. 16, pp. 6021–6026, 2005.

[99] X. Guo, A. A. Gorodetsky, J. Hone, J. K. Barton, and C. Nuckolls, "Conductivity of a single dna duplex bridging a carbon nanotube gap," *Nat Nanotechnol*, vol. 3, no. 3, pp. 163–7, 2008.

[100] B. R. Goldsmith, J. G. Coroneus, V. R. Khalap, A. A. Kane, G. A. Weiss, and P. G. Collins, "Conductance-controlled point functionalization of single-walled carbon nanotubes," *Science*, vol. 315, no. 5808, pp. 77–81, 2007.

[101] B. R. Goldsmith, J. G. Coroneus, A. A. Kane, G. A. Weiss, and P. G. Collins, "Monitoring single-molecule reactivity on a carbon nanotube," *Nano Lett*, vol. 8, no. 1, pp. 189–94, 2008.

[102] S. Ram, E. S. Ward, and R. J. Ober, "Beyond rayleigh's criterion: A resolution measure with application to single-molecule microscopy," *Proceedings of the National Academy of Sciences of the United States of America*, vol. 103, no. 12, pp. 4457–4462, 2006.

[103] D. M. Willard and A. Van Orden, "Quantum dots - resonant energy-transfer sensor," *Nature Materials*, vol. 2, no. 9, pp. 575–576, 2003.

[104] K. A. Connors, *Chemical kinetics : the study of reaction rates in solution.* New York, N.Y.: VCH, 1990.

[105] J. Wang and P. Wolynes, "Intermittency of single molecule reaction dynamics in fluctuating environments," *Phys Rev Lett*, vol. 74, no. 21, pp. 4317–4320, 1995.

[106] H. P. Lu, L. Xun, and X. S. Xie, "Single-molecule enzymatic dynamics," *Science*, vol. 282, no. 5395, pp. 1877–82, 1998.

[107] S. Machlup, "Noise in semiconductors - spectrum of a 2-parameter random signal," *Journal of Applied Physics*, vol. 25, no. 3, pp. 341–343, 1954.

[108] M. J. Kirton and M. J. Uren, "Noise in solid-state microstructures - a new perspective on individual defects, interface states and low-frequency (1/f) noise," *Advances in Physics*, vol. 38, no. 4, pp. 367–468, 1989.

[109] R. Moller, A. Esslinger, and B. Koslowski, "Thermal noise in vacuum scanning tunneling microscopy at zero bias voltage," *Journal of Vacuum Science and Technology a-Vacuum Surfaces and Films*, vol. 8, no. 1, pp. 590–593, 1990.

[110] R. Saito, G. Dresselhaus, and M. S. Dresselhaus, *Physical properties of carbon nanotubes.* London: Imperial College Press, 1998.

[111] H. W. Kroto, J. R. Heath, S. C. Obrien, R. F. Curl, and R. E. Smalley, "C-60 - buckminsterfullerene," *Nature*, vol. 318, no. 6042, pp. 162–163, 1985.

[112] S. Iijima, "Helical microtubules of graphitic carbon," *Nature*, vol. 354, no. 6348, pp. 56–58, 1991.

[113] Y. Zhang, Y. W. Tan, H. L. Stormer, and P. Kim, "Experimental observation of the quantum hall effect and berry's phase in graphene," *Nature*, vol. 438, no. 7065, pp. 201–4, 2005.

[114] K. S. Novoselov, A. K. Geim, S. V. Morozov, D. Jiang, M. I. Katsnelson, I. V. Grigorieva, S. V. Dubonos, and A. A. Firsov, "Two-dimensional gas of massless dirac fermions in graphene," *Nature*, vol. 438, no. 7065, pp. 197–200, 2005.

[115] F. Bloch, "ber die quantenmechanik der elektronen in kristallgittern," *Zeitschrift fr Physik A Hadrons and Nuclei*, vol. 52, no. 7, pp. 555–600, 1929.

[116] P. Kim, T. W. Odom, J. L. Huang, and C. M. Lieber, "Electronic density of states of atomically resolved single-walled carbon nanotubes: Van hove singularities and end states," *Physical Review Letters*, vol. 82, no. 6, pp. 1225–1228, 1999.

[117] M. Y. Sfeir, F. Wang, L. M. Huang, C. C. Chuang, J. Hone, S. P. O'Brien, T. F. Heinz, and L. E. Brus, "Probing electronic transitions in individual carbon nanotubes by rayleigh scattering," *Science*, vol. 306, no. 5701, pp. 1540–1543, 2004.

[118] S. Zaric, G. N. Ostojic, J. Kono, J. Shaver, V. C. Moore, R. H. Hauge, R. E. Smalley, and W. Xing, "Estimation of magnetic susceptibility anisotropy of carbon nanotubes using magnetophotoluminescence," *Nano Letters*, vol. 4, no. 11, pp. 2219–2221, 2004.

[119] C. Kittel, *Introduction to solid state physics*, 8th ed. Hoboken, NJ: Wiley, 2005.

[120] Y. Imry, *Introduction to mesoscopic physics*, 2nd ed. Oxford ; New York: Oxford University Press, 2002.

[121] A. Javey, J. Guo, Q. Wang, M. Lundstrom, and H. Dai, "Ballistic carbon nanotube field-effect transistors," *Nature*, vol. 424, no. 6949, pp. 654–7, 2003.

[122] S. Datta, *Electronic transport in mesoscopic systems*. Cambridge ; New York: Cambridge University Press, 1995.

[123] M. S. Purewal, B. H. Hong, A. Ravi, B. Chandra, J. Hone, and P. Kim, "Scaling of resistance and electron mean free path of single-walled carbon nanotubes," *Phys Rev Lett*, vol. 98, no. 18, p. 186808, 2007.

[124] P. L. McEuen, M. Bockrath, D. H. Cobden, Y. G. Yoon, and S. G. Louie, "Disorder, pseudospins, and backscattering in carbon nanotubes," *Physical Review Letters*, vol. 83, no. 24, pp. 5098–5101, 1999.

[125] A. N. Andriotis, M. Menon, and G. E. Froudakis, "Various bonding configurations of transition-metal atoms on carbon nanotubes: Their effect on contact resistance," *Applied Physics Letters*, vol. 76, no. 26, pp. 3890–3892, 2000.

[126] R. Landauer, "Spatial variation of currents and fields due to localized scatterers in metallic conduction," *Ibm Journal of Research and Development*, vol. 1, no. 3, pp. 223–231, 1957.

[127] S. Iijima and T. Ichihashi, "Single-shell carbon nanotubes of 1-nm diameter," *Nature*, vol. 363, no. 6430, pp. 603–605, 1993.

[128] D. S. Bethune, C. H. Kiang, M. S. Devries, G. Gorman, R. Savoy, J. Vazquez, and R. Beyers, "Cobalt-catalyzed growth of carbon nanotubes with single-atomic-layerwalls," *Nature*, vol. 363, no. 6430, pp. 605–607, 1993.

[129] N. Hamada, S. Sawada, and A. Oshiyama, "New one-dimensional conductors - graphitic microtubules," *Physical Review Letters*, vol. 68, no. 10, pp. 1579–1581, 1992.

[130] D. H. Robertson, D. W. Brenner, and J. W. Mintmire, "Energetics of nanoscale graphitic tubules," *Physical Review B*, vol. 45, no. 21, pp. 12 592–12 595, 1992.

[131] H. J. Dai, "Carbon nanotubes: Synthesis, integration, and properties," *Accounts of Chemical Research*, vol. 35, no. 12, pp. 1035–1044, 2002.

[132] ——, "Nanotube growth and characterization," *Carbon Nanotubes*, vol. 80, pp. 29–53, 2001.

[133] S. J. Kang, C. Kocabas, T. Ozel, M. Shim, N. Pimparkar, M. A. Alam, S. V. Rotkin, and J. A. Rogers, "High-performance electronics using dense, perfectly aligned arrays of single-walled carbon nanotubes," *Nature Nanotechnology*, vol. 2, no. 4, pp. 230–236, 2007.

[134] S. R. P. Silva, G. Y. Chen, B. Jensen, and V. Stolojan, "Growth of carbon nanotubes at temperatures compatible with integrated circuit technologies," *Carbon*, vol. 49, no. 1, pp. 280–285, 2011.

[135] H. J. Dai, E. W. Wong, and C. M. Lieber, "Probing electrical transport in nanomaterials: Conductivity of individual carbon nanotubes," *Science*, vol. 272, no. 5261, pp. 523–526, 1996.

[136] M. Bockrath, D. H. Cobden, P. L. McEuen, N. G. Chopra, A. Zettl, A. Thess, and R. E. Smalley, "Single-electron transport in ropes of carbon nanotubes," *Science*, vol. 275, no. 5308, pp. 1922–1925, 1997.

[137] C. Dekker, A. Bachtold, P. Hadley, and T. Nakanishi, "Logic circuits with carbon nanotube transistors," *Science*, vol. 294, no. 5545, pp. 1317–1320, 2001.

[138] L. Y. Jiao, X. J. Xian, Z. Y. Wu, J. Zhang, and Z. F. Liu, "Selective positioning and integration of individual single-walled carbon nanotubes," *Nano Letters*, vol. 9, no. 1, pp. 205–209, 2009.

[139] Y. X. Zhou, L. B. Hu, and G. Gruner, "A method of printing carbon nanotube thin films," *Applied Physics Letters*, vol. 88, no. 12, 2006.

[140] J. A. Rogers, S. H. Hur, and O. O. Park, "Extreme bendability of single-walled carbon nanotube networks transferred from high-temperature growth substrates to plastic and their use in thin-film transistors," *Applied Physics Letters*, vol. 86, no. 24, 2005.

[141] C. W. Zhou, F. N. Ishikawa, H. K. Chang, K. Ryu, P. C. Chen, A. Badmaev, L. G. De Arco, and G. Z. Shen, "Transparent electronics based on transfer printed aligned carbon nanotubes on rigid and flexible substrates," *Acs Nano*, vol. 3, no. 1, pp. 73–79, 2009.

[142] R. Krupke, F. Hennrich, H. B. Weber, M. M. Kappes, and H. von Lohneysen, "Simultaneous deposition of metallic bundles of single-walled carbon nanotubes using ac-dielectrophoresis," *Nano Letters*, vol. 3, no. 8, pp. 1019–1023, 2003.

[143] R. Krupke, F. Hennrich, H. von Lohneysen, and M. M. Kappes, "Separation of metallic from semiconducting single-walled carbon nanotubes," *Science*, vol. 301, no. 5631, pp. 344–347, 2003.

[144] R. E. Smalley *et al.*, "Band gap fluorescence from individual single-walled carbon nanotubes," *Science*, vol. 297, no. 5581, pp. 593–596, 2002.

[145] S. J. Wind, M. Radosavljevic, J. Appenzeller, and P. Avouris, "Transistor structures for the study of scaling in carbon nanotubes," *Journal of Vacuum Science and Technology B*, vol. 21, no. 6, pp. 2856–2859, 2003.

[146] N. Fukui, A. Taninaka, T. Suga, H. Yoshida, S. Heike, M. Fujimori, Y. Terada, T. Hashizume, and H. Shinohara, "Placing and imaging individual carbon nanotubes on cu(111) clean surface using in situ pulsed-jet deposition-stm technique," *Journal of Nanoscience and Nanotechnology*, vol. 7, no. 12, pp. 4267–4271, 2007.

[147] L. An and C. R. Friedrich, "Real-time gap impedance monitoring of dielectrophoretic assembly of multiwalled carbon nanotubes," *Applied Physics Letters*, vol. 92, no. 17, 2008.

[148] S. Sorgenfrei, I. Meric, S. Banerjee, A. Akey, S. Rosenblatt, I. P. Herman, and K. L. Shepard, "Controlled dielectrophoretic assembly of carbon nanotubes using real-time electrical detection," *Applied Physics Letters*, vol. 94, no. 5, 2009.

[149] R. Martel, T. Schmidt, H. R. Shea, T. Hertel, and P. Avouris, "Single- and multi-wall carbon nanotube field-effect transistors," *Applied Physics Letters*, vol. 73, no. 17, pp. 2447–2449, 1998.

[150] J. U. Lee, "Photovoltaic effect in ideal carbon nanotube diodes," *Applied Physics Letters*, vol. 87, no. 7, 2005.

[151] D. A. Barry, J. Y. Parlange, L. Li, H. Prommer, C. J. Cunningham, and E. Stagnitti, "Analytical approximations for real values of the lambert w-function," *Mathematics and Computers in Simulation*, vol. 53, no. 1, 2000.

[152] R. C. Haddon, M. E. Itkis, D. E. Perea, S. Niyogi, S. M. Rickard, M. A. Hamon, and B. Zhao, "Purity evaluation of as-prepared single-walled carbon nanotube soot by use of solution-phase near-ir spectroscopy," *Nano Letters*, vol. 3, no. 3, pp. 309–314, 2003.

[153] A. J. Bard and L. R. Faulkner, *Electrochemical methods : fundamentals and applications*, 2nd ed. New York: John Wiley, 2001.

[154] J. S. Newman and K. E. Thomas-Alyea, *Electrochemical systems*, 3rd ed. Hoboken, N.J.: Wiley-Interscience, 2004.

[155] O. Stern, "The theory of the electrolytic double shift," *Zeitschrift Fur Elektrochemie Und Angewandte Physikalische Chemie*, vol. 30, pp. 508–516, 1924.

[156] P. L. McEuen, "Single-wall carbon nanotubes," *Physics World*, vol. 13, no. 6, pp. 31–36, 2000.

[157] J. D. Jackson, *Classical electrodynamics*, 2nd ed. New York: Wiley, 1975.

[158] M. Ishida, H. Hongo, F. Nihey, and Y. Ochiai, "Diameter-controlled carbon nanotubes grown from lithographically defined nanoparticles," *Japanese Journal of Applied Physics Part 2-Letters and Express Letters*, vol. 43, no. 10, 2004.

[159] L. M. Huang, X. D. Cui, B. White, and S. P. O'Brien, "Long and oriented single-walled carbon nanotubes grown by ethanol chemical vapor deposition," *Journal of Physical Chemistry B*, vol. 108, no. 42, pp. 16 451–16 456, 2004.

[160] M. Ishigami, J. H. Chen, W. G. Cullen, M. S. Fuhrer, and E. D. Williams, "Atomic structure of graphene on sio2," *Nano Letters*, vol. 7, no. 6, pp. 1643–1648, 2007.

[161] A. Blaum, O. Pilloud, G. Scalea, J. Victory, and F. Sischka, "A new robust on-wafer 1/f noise measurement and characterization system," in *Microelectronic Test Structures, 2001. ICMTS 2001. Proceedings of the 2001 International Conference on*, 2001, pp. 125–130.

[162] F. N. Hooge, "1/f noise sources," *Electron Devices, IEEE Transactions on*, vol. 41, no. 11, pp. 1926–1935, 1994.

[163] J. Mannik, I. Heller, A. M. Janssens, S. G. Lemay, and C. Dekker, "Charge noise in liquid-gated single-wall carbon nanotube transistors," *Nano Lett*, vol. 8, no. 2, pp. 685–8, 2008.

[164] J. Tersoff, "Low-frequency noise in nanoscale ballistic transistors," *Nano Letters*, vol. 7, no. 1, pp. 194–198, 2007.

[165] J. Appenzeller, J. Knoch, V. Derycke, R. Martel, S. Wind, and P. Avouris, "Field-modulated carrier transport in carbon nanotube transistors," *Phys Rev Lett*, vol. 89, no. 12, p. 126801, 2002.

[166] J. Appenzeller, Y. M. Lin, J. Knoch, Z. H. Chen, and P. Avouris, "Comparing carbon nanotube transistors - the ideal choice: A novel tunneling device design," *Ieee Transactions on Electron Devices*, vol. 52, no. 12, pp. 2568–2576, 2005.

[167] M. O'Connell, "Carbon nanotubes properties and applications," 2006, online EBOOKS.

[168] S. Heinze, M. Radosavljevic, J. Tersoff, and P. Avouris, "Unexpected scaling of the performance of carbon nanotube schottky-barrier transistors," *Physical Review B*, vol. 68, no. 23, 2003.

[169] S. Rosenblatt, Y. Yaish, J. Park, J. Gore, V. Sazonova, and P. L. McEuen, "High performance electrolyte gated carbon nanotube transistors," *Nano Letters*, vol. 2, no. 8, pp. 869–872, 2002.

[170] M. S. Fuhrer, T. Durkop, S. A. Getty, and E. Cobas, "Extraordinary mobility in semiconducting carbon nanotubes," *Nano Letters*, vol. 4, no. 1, pp. 35–39, 2004.

[171] K. Besteman, J. O. Lee, F. G. M. Wiertz, H. A. Heering, and C. Dekker, "Enzyme-coated carbon nanotubes as single-molecule biosensors," *Nano Letters*, vol. 3, no. 6, pp. 727–730, 2003.

[172] R. J. Chen, H. C. Choi, S. Bangsaruntip, E. Yenilmez, X. W. Tang, Q. Wang, Y. L. Chang, and H. J. Dai, "An investigation of the mechanisms of electronic sensing of protein adsorption on carbon nanotube devices," *Journal of the American Chemical Society*, vol. 126, no. 5, pp. 1563–1568, 2004.

[173] A. Star, J. C. P. Gabriel, K. Bradley, and G. Gruner, "Electronic detection of specific protein binding using nanotube fet devices," *Nano Letters*, vol. 3, no. 4, pp. 459–463, 2003.

[174] S. Sorgenfrei, C. Y. Chiu, R. L. Gonzalez, Y. J. Yu, P. Kim, C. Nuckolls, and K. L. Shepard, "Label-free single-molecule detection of dna-hybridization kinetics with a carbon nanotube field-effect transistor," *Nature Nanotechnology*, vol. 6, no. 2, pp. 125–131, 2011.

[175] A. M. Armani, R. P. Kulkarni, S. E. Fraser, R. C. Flagan, and K. J. Vahala, "Label-free, single-molecule detection with optical microcavities," *Science*, vol. 317, no. 5839, pp. 783–7, 2007.

[176] T. P. Burg, M. Godin, S. M. Knudsen, W. Shen, G. Carlson, J. S. Foster, K. Babcock, and S. R. Manalis, "Weighing of biomolecules, single cells and single nanoparticles in fluid," *Nature*, vol. 446, no. 7139, pp. 1066–9, 2007.

[177] R. C. Hughes, A. J. Ricco, M. A. Butler, and S. J. Martin, "Chemical microsensors," *Science*, vol. 254, no. 5028, pp. 74–80, 1991.

[178] C. Cecconi, E. A. Shank, C. Bustamante, and S. Marqusee, "Direct observation of the three-state folding of a single protein molecule," *Science*, vol. 309, no. 5743, pp. 2057–60, 2005.

[179] V. V. Deshpande, B. Chandra, R. Caldwell, D. S. Novikov, J. Hone, and M. Bockrath, "Mott insulating state in ultraclean carbon nanotubes," *Science*, vol. 323, no. 5910, pp. 106–10, 2009.

[180] P. Jarillo-Herrero, J. Kong, H. S. J. van der Zant, C. Dekker, L. P. Kouwenhoven, and S. De Franceschi, "Orbital kondo effect in carbon nanotubes," *Nature*, vol. 434, no. 7032, pp. 484–488, 2005.

[181] H. Park, J. J. Zhao, and J. P. Lu, "Distinct properties of single-wall carbon nanotubes with monovalent sidewall additions," *Nanotechnology*, vol. 16, no. 6, pp. 635–638, 2005.

[182] J. C. Charlier, T. W. Ebbesen, and P. Lambin, "Structural and electronic properties of pentagon-heptagon pair defects in carbon nanotubes," *Physical Review B*, vol. 53, no. 16, pp. 11 108–11 113, 1996.

[183] J. C. Charlier, "Defects in carbon nanotubes," *Accounts of Chemical Research*, vol. 35, no. 12, pp. 1063–1069, 2002.

[184] M. Bockrath, W. J. Liang, D. Bozovic, J. H. Hafner, C. M. Lieber, M. Tinkham, and H. K. Park, "Resonant electron scattering by defects in single-walled carbon nanotubes," *Science*, vol. 291, no. 5502, pp. 283–285, 2001.

[185] Y. W. Fan, B. R. Goldsmith, and P. G. Collins, "Identifying and counting point defects in carbon nanotubes," *Nature Materials*, vol. 4, no. 12, pp. 906–911, 2005.

[186] S. I. Khondaker and P. Stokes, "Evaluating defects in solution-processed carbon nanotube devices via low-temperature transport spectroscopy," *Acs Nano*, vol. 4, no. 5, pp. 2659–2666, 2010.

[187] C. Dekker, Z. Yao, H. W. C. Postma, and L. Balents, "Carbon nanotube intramolecular junctions," *Nature*, vol. 402, no. 6759, pp. 273–276, 1999.

[188] J. Hone *et al.*, "Molecular-scale quantum dots from carbon nanotube heterojunctions," *Nano Letters*, vol. 9, no. 4, pp. 1544–1548, 2009.

[189] J. Y. Park, Y. Yaish, M. Brink, S. Rosenblatt, and P. L. McEuen, "Electrical cutting and nicking of carbon nanotubes using an atomic force microscope," *Applied Physics Letters*, vol. 80, no. 23, pp. 4446–4448, 2002.

[190] L. C. Venema, J. W. G. Wildoer, H. L. J. T. Tuinstra, C. Dekker, A. G. Rinzler, and R. E. Smalley, "Length control of individual carbon nanotubes by nanostructuring with a scanning tunneling microscope," *Applied Physics Letters*, vol. 71, no. 18, pp. 2629–2631, 1997.

[191] C. Dekker, H. W. C. Postma, T. Teepen, Z. Yao, and M. Grifoni, "Carbon nanotube single-electron transistors at room temperature," *Science*, vol. 293, no. 5527, pp. 76–79, 2001.

[192] H. W. C. Postma, M. de Jonge, Z. Yao, and C. Dekker, "Electrical transport through carbon nanotube junctions created by mechanical manipulation," *Physical Review B*, vol. 62, no. 16, pp. 10 653–10 656, 2000.

[193] Z. Osvath, G. Vertesy, L. Tapaszto, F. Weber, Z. E. Horvath, J. Gyulai, and L. P. Biro, "Atomically resolved stm images of carbon nanotube defects produced by ar+ irradiation," *Physical Review B*, vol. 72, no. 4, 2005.

[194] F. Banhart, J. X. Li, and A. V. Krasheninnikov, "Carbon nanotubes under electron irradiation: Stability of the tubes and their action as pipes for atom transport," *Physical Review B*, vol. 71, no. 24, 2005.

[195] P. G. Collins, J. G. Coroneus, B. R. Goldsmith, J. A. Lamboy, A. A. Kane, and G. A. Weiss, "Mechanism-guided improvements to the single molecule oxidation of carbon nanotube sidewalls," *Chemphyschem*, vol. 9, no. 7, pp. 1053–1056, 2008.

[196] K. Kinoshita, *Carbon : electrochemical and physicochemical properties*. New York: Wiley, 1988.

[197] M. K. Ashraf, N. A. Bruque, R. R. Pandey, P. G. Collins, and R. K. Lake, "Effect of localized oxygen functionalization on the conductance of metallic carbon nanotubes," *Physical Review B*, vol. 79, no. 11, 2009.

[198] D. V. Kosynkin, A. L. Higginbotham, A. Sinitskii, J. R. Lomeda, A. Dimiev, B. K. Price, and J. M. Tour, "Longitudinal unzipping of carbon nanotubes to form graphene nanoribbons," *Nature*, vol. 458, no. 7240, pp. 872–6, 2009.

[199] C. W. Zhou, J. Kong, and H. J. Dai, "Intrinsic electrical properties of individual single-walled carbon nanotubes with small band gaps," *Physical Review Letters*, vol. 84, no. 24, pp. 5604–5607, 2000.

[200] W. Kim, A. Javey, R. Tu, J. Cao, Q. Wang, and H. J. Dai, "Electrical contacts to carbon nanotubes down to 1 nm in diameter," *Applied Physics Letters*, vol. 87, no. 17, 2005.

[201] H. J. Choi, J. Ihm, S. G. Louie, and M. L. Cohen, "Defects, quasibound states, and quantum conductance in metallic carbon nanotubes," *Physical Review Letters*, vol. 84, no. 13, pp. 2917–2920, 2000.

[202] M. Bockrath, D. H. Cobden, J. Lu, A. G. Rinzler, R. E. Smalley, L. Balents, and P. L. McEuen, "Luttinger-liquid behaviour in carbon nanotubes," *Nature*, vol. 397, no. 6720, pp. 598–601, 1999.

[203] Z. Yao, H. W. C. Postma, L. Balents, and C. Dekker, "Carbon nanotube intramolecular junctions," *Nature*, vol. 402, no. 6759, pp. 273–276, 1999.

[204] C. Kane, L. Balents, and M. P. A. Fisher, "Coulomb interactions and mesoscopic effects in carbon nanotubes," *Physical Review Letters*, vol. 79, no. 25, pp. 5086–5089, 1997.

[205] A. Bachtold, M. S. Fuhrer, S. Plyasunov, M. Forero, E. H. Anderson, A. Zettl, and P. L. McEuen, "Scanned probe microscopy of electronic transport in carbon nanotubes," *Phys Rev Lett*, vol. 84, no. 26, 2000.

[206] P. N. Borer, B. Dengler, J. Tinoco, I., and O. C. Uhlenbeck, "Stability of ribonucleic acid double-stranded helices," *J Mol Biol*, vol. 86, no. 4, pp. 843–53, 1974.

[207] P. Gong and R. Levicky, "Dna surface hybridization regimes," *Proc Natl Acad Sci U S A*, vol. 105, no. 14, pp. 5301–6, 2008.

[208] Y. Sun, N. C. Harris, and C. H. Kiang, "Melting transition of directly linked gold nanoparticle dna assembly," *Physica a-Statistical Mechanics and Its Applications*, vol. 350, no. 1, pp. 89–94, 2005.

[209] V. A. Karachevtsev, G. O. Gladchenko, M. V. Karachevtsev, V. A. Valeev, V. S. Leontiev, and O. S. Lytvyn, "Adsorption of poly(ra) on the carbon nanotube surface and its hybridization with poly(ru)," *Chemphyschem*, vol. 9, no. 14, pp. 2010–8, 2008.

[210] G. P. Brewood, Y. Rangineni, D. J. Fish, A. S. Bhandiwad, D. R. Evans, R. Solanki, and A. S. Benight, "Electrical detection of the temperature induced melting transition of a dna hairpin covalently attached to gold interdigitated microelectrodes," *Nucleic Acids Res*, vol. 36, no. 15, p. e98, 2008.

[211] S. L. Miller and D. G. Childers, *Probability and random processes : with applications to signal processing and communications*. Amsterdam ; Boston: Elsevier Academic Press, 2004.

[212] L. E. Baum, T. Petrie, G. Soules, and N. Weiss, "A maximization technique occurring in the statistical analysis of probabilistic functions of markov chains," *The Annals of Mathematical Statistics*, vol. 41, no. 1, pp. 164–171, 1970.

[213] A. Viterbi, "Error bounds for convolutional codes and an asymptotically optimum decoding algorithm," *Information Theory, IEEE Transactions on*, vol. 13, no. 2, pp. 260–269, 1967.

[214] L. R. Rabiner, "A tutorial on hidden markov-models and selected applications in speech recognition," *Proceedings of the Ieee*, vol. 77, no. 2, pp. 257–286, 1989.

[215] S. R. Eddy, "What is a hidden markov model?" *Nature Biotechnology*, vol. 22, no. 10, pp. 1315–1316, 2004.

[216] A. Krogh, B. Larsson, G. von Heijne, and E. L. L. Sonnhammer, "Predicting transmembrane protein topology with a hidden markov model: Application to complete genomes," *Journal of Molecular Biology*, vol. 305, no. 3, pp. 567–580, 2001.

[217] T. Ha, S. A. McKinney, and C. Joo, "Analysis of single-molecule fret trajectories using hidden markov modeling," *Biophysical Journal*, vol. 91, no. 5, pp. 1941–1951, 2006.

[218] J. E. Bronson, J. Fei, J. M. Hofman, J. Gonzalez, R. L., and C. H. Wiggins, "Learning rates and states from biophysical time series: a bayesian approach to model selection and single-molecule fret data," *Biophys J*, vol. 97, no. 12, pp. 3196–205, 2009.

[219] J. Fei, J. E. Bronson, J. M. Hofman, R. L. Srinivas, C. H. Wiggins, and J. Gonzalez, R. L., "Allosteric collaboration between elongation factor g and the ribosomal l1 stalk directs trna movements during translation," *Proc Natl Acad Sci U S A*, vol. 106, no. 37, pp. 15 702–7, 2009.

[220] V. Chan, D. J. Graves, and S. E. McKenzie, "The biophysics of dna hybridization with immobilized oligonucleotide probes," *Biophys J*, vol. 69, no. 6, pp. 2243–55, 1995.

[221] P. H. von Hippel and O. G. Berg, "Facilitated target location in biological systems," *J Biol Chem*, vol. 264, no. 2, pp. 675–8, 1989.

[222] S. E. Halford and J. F. Marko, "How do site-specific dna-binding proteins find their targets?" *Nucleic Acids Res*, vol. 32, no. 10, pp. 3040–52, 2004.

[223] A. Ansari, S. V. Kuznetsov, and Y. Shen, "Configurational diffusion down a folding funnel describes the dynamics of dna hairpins," *Proc Natl Acad Sci U S A*, vol. 98, no. 14, pp. 7771–6, 2001.

[224] M. Oliveberg, Y. J. Tan, and A. R. Fersht, "Negative activation enthalpies in the kinetics of protein folding," *Proc Natl Acad Sci U S A*, vol. 92, no. 19, pp. 8926–9, 1995.

[225] C. M. Dobson, A. Sali, and M. Karplus, "Protein folding: A perspective from theory and experiment," *Angewandte Chemie-International Edition*, vol. 37, no. 7, pp. 868–893, 1998.

[226] T. V. Chalikian, J. Volker, G. E. Plum, and K. J. Breslauer, "A more unified picture for the thermodynamics of nucleic acid duplex melting: a characterization by calorimetric and volumetric techniques," *Proc Natl Acad Sci U S A*, vol. 96, no. 14, pp. 7853–8, 1999.

[227] G. Altan-Bonnet, A. Libchaber, and O. Krichevsky, "Bubble dynamics in double-stranded dna," *Phys Rev Lett*, vol. 90, no. 13, p. 138101, 2003.

[228] R. Metzler, T. Ambjornsson, A. Hanke, and H. C. Fogedby, "Single dna denaturation and bubble dynamics," *Journal of Physics-Condensed Matter*, vol. 21, no. 3, pp. –, 2009.

[229] A. Norlin, J. Pan, and C. Leygraf, "Investigation of electrochemical behavior of stimulation/sensing materials for pacemaker electrode applications i. pt, ti, and tin coated electrodes," *Journal of the Electrochemical Society*, vol. 152, no. 2, pp. J7–J15, 2005.

[230] S. Sorgenfrei, C. Y. Chiu, M. Johnston, C. Nuckolls, and K. L. Shepard, "Debye screening in single-molecule carbon nanotube field-effect sensors," *Nano Lett*, 2011.

[231] V. R. Khalap, T. Sheps, A. A. Kane, and P. G. Collins, "Hydrogen sensing and sensitivity of palladium-decorated single-walled carbon nanotubes with defects," *Nano Letters*, vol. 10, no. 3, pp. 896–901, 2010.

[232] G. J. Zhang, G. Zhang, J. H. Chua, R. E. Chee, E. H. Wong, A. Agarwal, K. D. Buddharaju, N. Singh, Z. Q. Gao, and N. Balasubramanian, "Dna sensing by silicon nanowire: Charge layer distance dependence," *Nano Letters*, vol. 8, no. 4, pp. 1066–1070, 2008.

[233] X. P. A. Gao, G. F. Zheng, and C. M. Lieber, "Subthreshold regime has the optimal sensitivity for nanowire fet biosensors," *Nano Letters*, vol. 10, no. 2, pp. 547–552, 2010.

[234] E. Stern, R. Wagner, F. J. Sigworth, R. Breaker, T. M. Fahmy, and M. A. Reed, "Importance of the debye screening length on nanowire field effect transistor sensors," *Nano Letters*, vol. 7, no. 11, pp. 3405–3409, 2007.

[235] L. Prisbrey, G. Schneider, and E. Minot, "Modeling the electrostatic signature of single enzyme activity," *Journal of Physical Chemistry B*, vol. 114, no. 9, pp. 3330–3333, 2010.

[236] T. Yajima, "Electrochemical characteristics of platinum surface treated by rf plasma," *Surface and Coatings Technology*, vol. 112, no. 1, 1999.

[237] Z. Y. Li, P. Beck, D. A. A. Ohlberg, D. R. Stewart, and R. S. Williams, "Surface properties of platinum thin films as a function of plasma treatment conditions," *Surface Science*, vol. 529, no. 3, pp. 410–418, 2003.

[238] J. C. McDonald and G. M. Whitesides, "Poly(dimethylsiloxane) as a material for fabricating microfluidic devices," *Accounts of Chemical Research*, vol. 35, no. 7, pp. 491–499, 2002.

[239] J. N. Lee, C. Park, and G. M. Whitesides, "Solvent compatibility of poly(dimethylsiloxane)-based microfluidic devices," *Analytical Chemistry*, vol. 75, no. 23, pp. 6544–6554, 2003.

[240] P. Debye and E. Huckel, "The theory of electrolytes i. the lowering of the freezing point and related occurrences," *Physikalische Zeitschrift*, vol. 24, pp. 185–206, 1923.

[241] M. Mandelkern, J. G. Elias, D. Eden, and D. M. Crothers, "The dimensions of dna in solution," *Journal of Molecular Biology*, vol. 152, no. 1, pp. 153–161, 1981.

[242] U. Rant, K. Arinaga, S. Scherer, E. Pringsheim, S. Fujita, N. Yokoyama, M. Tornow, and G. Abstreiter, "Switchable dna interfaces for the highly sensitive detection of label-free dna targets," *Proceedings of the National Academy of Sciences of the United States of America*, vol. 104, no. 44, pp. 17 364–17 369, 2007.

[243] S. O. Kelley, J. K. Barton, N. M. Jackson, L. D. McPherson, A. B. Potter, E. M. Spain, M. J. Allen, and M. G. Hill, "Orienting dna helices on gold using applied electric fields," *Langmuir*, vol. 14, no. 24, pp. 6781–6784, 1998.

[244] J. W. Cheng, S. H. Chou, M. Salazar, and B. R. Reid, "Solution structure of d(gcgtatacgc) 2," *Journal of Molecular Biology*, vol. 228, no. 1, pp. 118–137, 1992.

[245] T. J. Dolinsky, J. E. Nielsen, J. A. McCammon, and N. A. Baker, "Pdb2pqr: an automated pipeline for the setup of poisson-boltzmann electrostatics calculations," *Nucleic Acids Research*, vol. 32, pp. W665–W667, 2004.

[246] W. Rocchia, E. Alexov, and B. Honig, "Extending the applicability of the nonlinear poisson-boltzmann equation: Multiple dielectric constants and multivalent ions," *Journal of Physical Chemistry B*, vol. 105, no. 28, pp. 6507–6514, 2001.

[247] Y. M. Lin, J. C. Tsang, M. Freitag, and P. Avouris, "Impact of oxide substrate on electrical and optical properties of carbon nanotube devices," *Nanotechnology*, vol. 18, no. 29, 2007.

[248] C. R. Dean *et al.*, "Boron nitride substrates for high-quality graphene electronics," *Nature Nanotechnology*, vol. 5, no. 10, pp. 722–726, 2010.

[249] P. Kim and A. F. Young, "Quantum interference and klein tunnelling in graphene heterojunctions," *Nature Physics*, vol. 5, no. 3, pp. 222–226, 2009.